2016-06-01

The Effect of Projectile Nose Shape on the Formation of the Water Entry Cavity

Jeremy Conrad Ellis
Brigham Young University

The Effect of Projectile Nose Shape on the Formation of the Water Entry Cavity

Jeremy Conrad Ellis

A thesis submitted to the faculty of
Brigham Young University
in partial fulfillment of the requirements for the degree of

Master of Science

Tadd T. Truscott, Chair
Julie Crockett
R. Daniel Maynes

Department of Mechanical Engineering

Brigham Young University

June 2016

ABSTRACT

The Effect of Projectile Nose Shape on Formation of the Water Entry Cavity

Jeremy Ellis
Department of Mechanical Engineering, BYU
Master of Science

This research focuses on the effect of several convex and concave nose shapes on cavity formation for both hydrophilic and hydrophobic projectiles. It specifically investigates the effect of convex shape on the threshold velocity for cavity formation as well as the effect of concave shapes on cavity formation in terms of impact velocity, geometry of the concave shape and wettability of the projectile. For the convex cases, the streamlined axisymmetric shape significantly increases the threshold velocity when cavities form and is most pronounced for the ogive and cone. The study demonstrates that measuring the wetting angle and impact velocity is not enough to predict cavity behavior, rather the roughness and nose shape must also be taken into consideration for convex projectiles. For the concave cases, the cavities formed are highly influenced by impact speed and nose shape. Wetting angle did not have any visible effect on the cavity formed at higher impact speeds (7 m/s). The dynamics of the cavity formation are dominated by the pocket of trapped air formed when the concave projectiles impact the water. At low impact speeds (~0-1 m/s) the trapped air can separate the flow from the leading edge of the projectile nose when venting out and cause a large cavity to form, depending on the specific concave shape and speed. At moderate impact speeds (1-4 m/s) the trapped air will vent completely underwater forming a small ring-shaped cavity. At high impact speeds (4-10 m/s) the trapped pocket of air compresses tremendously and causes an unsteady pressure pulse, which can result in the formation of a bubble and jet in front of the cavity. The jet is formed by water passing behind the pocket of trapped air along the walls of the concave nose and converging into a jet at the top of the concave shape and entraining the trapped air as it descends.

Keywords: water entry, projectiles, underwater cavities, nose shapes, concave noses, wetting, roughness, jets

ACKNOWLEDGEMENTS

I would like to thank Brigham Young University, and the Department of Mechanical Engineering for providing the facility, equipment, and materials necessary to conduct this research. I also would like to thank my committee for providing guidance and support in preparing this thesis. I want to thank Dr. Truscott for all of his hard work, mentoring, patience, and insight throughout this research. I also want to thank him for sticking with me even after changing universities. I want to thank the members of the Splash Lab for the training and mentoring and especially Benjamin Lovett, and Madison Boyer for collecting a good portion of the data, and Kyle Bodily for letting me inherit his test set up and all of his data collecting wisdom. I want to thank Dr. Linford and his students for the training and use of their contact angle goniometer. I want to thank my wife Kathryn and my two wonderful children, Evelyn and Ezra for their love and support. Most importantly I want to thank my Savior, Jesus Christ, who has always been there for me, for His grace, love, and making me all that I am.

TABLE OF CONTENTS

LIST OF TABLES

LIST OF FIGURES

1 INTRODUCTION

Many studies have investigated projectile water entry and the effect of projectile nose shape on various facets of water entry. Projectile nose shape variations include: spherical, a-spherical and axisymmetric (nose shape followed by a cylindrical body). Some studies have shown how sphere and spheroid geometries affect the impact velocity at which a cavity will form, but no studies so far have determined the effect of a nose shape followed by a cylindrical shaft. This study sets out to determine the effect of axisymmetric nose shapes on cavity formation, specifically the effect of convex shapes on the threshold velocity for cavity formation, and the mechanism of cavity formation in the concave case generally. This chapter starts by discussing cavity dynamics and the factors that affect cavity formation. The background then illustrates the importance of the research by discussing the influence of cavities and the factors that contribute to cavity formation on the general subjects studied within water entry, namely forces during water entry, underwater trajectory and stability, and acoustics. This chapter will then discuss some of the past research that specifically addresses the influence of geometry and surface condition on the water-entry cavity and establish the need for the current study.

1.1 Fundamentals of water entry and cavity formation

Water entry is ubiquitous in life, whether splashing in a rain puddle, dropping food in a pot of water, or skipping a rock across a lake. In solid-object water-entry the object transitions from flow through a gas (air) to flow through a liquid (water). When the object enters the liquid,

the liquid must move out of the way for the object to enter. The interaction between the three phases (solid, liquid, and gas) present at the entry dominates the water entry phenomenon.

Under the right conditions a projectile will form a cavity in the water surface by forcing the water away from the projectile and entraining air behind it. Truscott et al. [1] listed the stages of the water entry event as radial jet formation, splash crown formation, splash dome over and cavity seal (forms of cavity sealing include surface-seal, deep-seal, shallow-seal, and quasi-static seal). Figure 1-1 illustrates the splash crown, splash dome over, and surface seal of an axisymmetric projectile (Ogive) used in the current study. They explained that a cavity forms

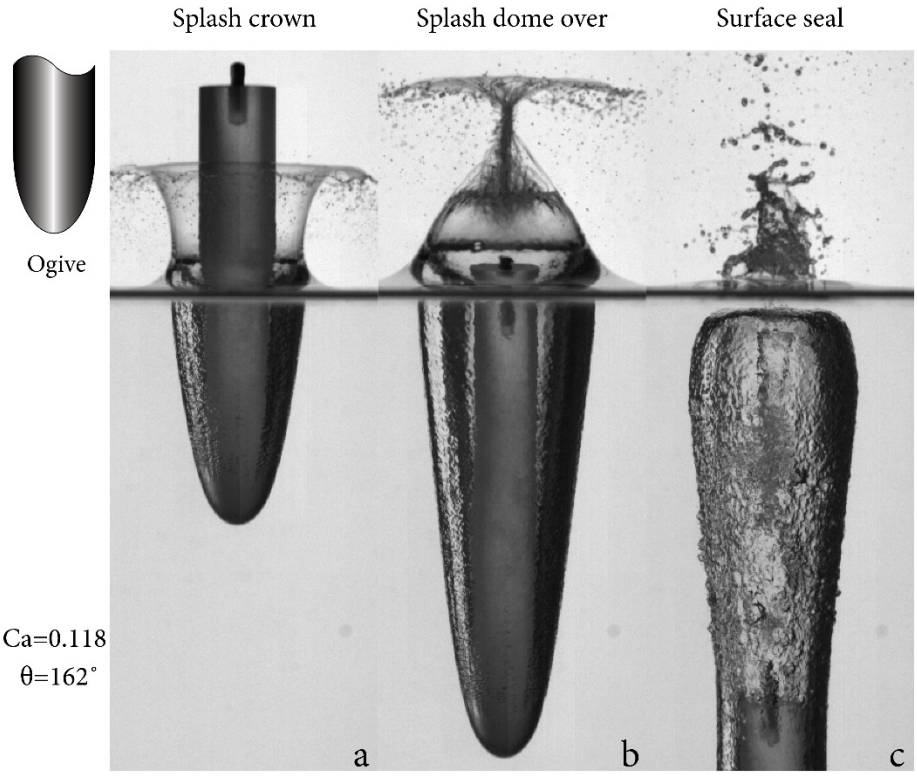

Figure 1-1. Stages of cavity formation for an ogive shaped projectile (cross section shown in upper left). The formation of the splash crown is depicted in a. The splash dome over is depicted in b and the surface seal in c.

when viscous forces outweigh surface tension forces at the air-water-projectile line and a contact line is pinned to the projectile surface. This contact line pinning allows air to be entrained and a cavity to be formed.

Several studies have given insight on the stages of water entry. Lee et al [2] found that the non-dimensional time of deep closure is essentially constant and independent of impact velocity for a sphere and that the location of deep closure only has a weak dependence on impact velocity. Aristoff et al. [3] showed however, that while the time of pinch off will remain the same, the depth of pinch off can be altered by lowering the mass ratio of the spheres. Yao et al. [4] developed a model based off of [5] [6] [7] that describes the evolution of the cavity shape that they claimed would work for any projectile nose shape.

Truscott et al. [1] further outlined that the key parameters of Capillary number ($Ca = \mu U_o/\gamma$), wetting angle (θ) and geometry determine whether or not an air-entraining cavity will form. Figure 1-2 shows how varying each of these parameters can affect when a cavity forms. Each image in the figure only varies by one variable (either capillary number, nose shape, or wetting angle) when compared to the one preceding it. Image 1a shows an entry without cavity formation. As the impact speed, or capillary number, increases the projectile forms a cavity, image 1b. When the nose shape is changed however, no cavity is formed, image 2a. A cavity again forms when the wetting angle increases, image 2b.

Geometry, wetting angle (surface condition), and the Capillary number certainly all play a role in cavity formation as Figure 1-2 has demonstrated. The Capillary number is a non-dimensional comparison of the inertial and surface tension forces, and its influence is fairly straightforward. At low Capillary numbers the surface tension forces are most prevalent but as

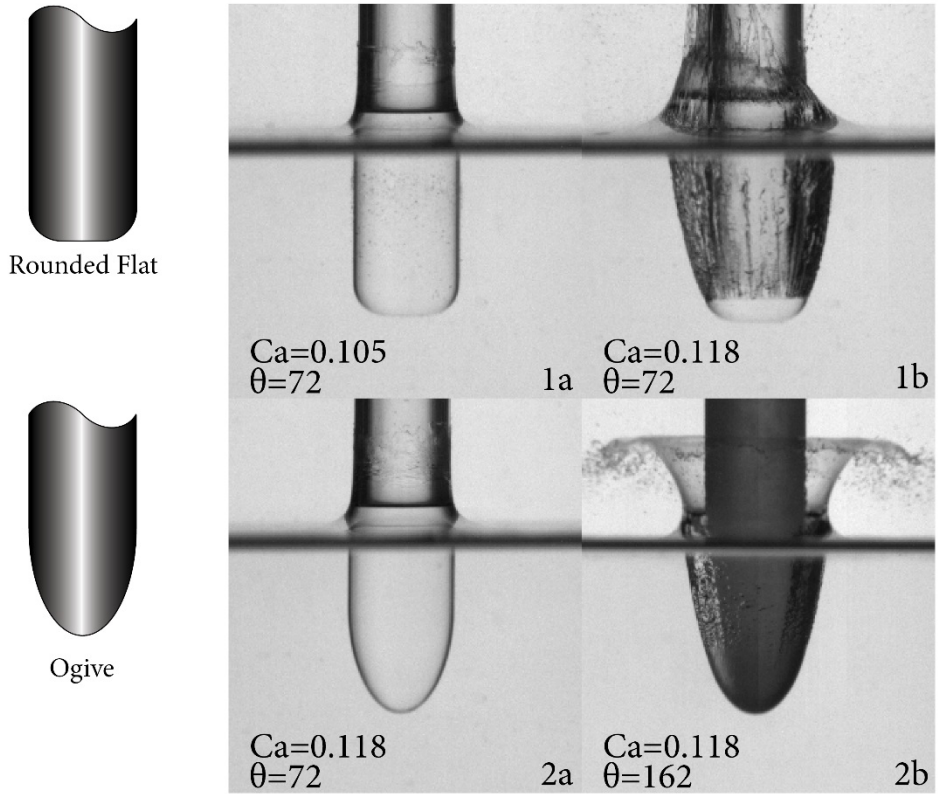

Figure 1-2. Entry of several shapes with several different entry conditions. In image 1a the rounded flat shape enters without forming a cavity. Image 1b shows the entry of the same shape when the capillary number increases and a distinct cavity forms illustrating the dependence of cavity formation on capillary number. Image 2a shows the entry of a different shape at the same capillary number and surface condition as image 1b yet no cavity forms, showing the dependence of cavity formation on the geometry in addition to capillary number. Image 2b shows the entry of the same shape at the same capillary number as image 2a but with a different wetting angle, where a cavity forms. This shows the dependence of cavity formation on wetting condition.

the Capillary number increases the inertial forces overcome the surface tension forces. The influence of geometry (projectile nose shape) and wetting angle (surface condition) are a little less straight forward. The nose shape affects the large scale displacement of the flow at impact [8] while the wetting angle is a measure of the influence of wetting on the projectile surface and is a function of both surface chemistry and surface morphology (roughness) [9]. Outside of their effects on cavity formation they affect several other subjects within the study of water entry

including but not limited to forces at impact, trajectory and stability, and acoustics. A brief review on their effects in these areas is given in the next section to illustrate the importance of understanding their combined influence in the study of water-entry as a whole. A discussion of the previous research concerning the influence of geometry and surface condition on cavity formation is then presented, outlining what has been done and where the current knowledge is lacking.

1.2 Influence of geometry and surface condition in other subjects of water entry

The following sections serve a dual purpose. They give a sampling of the different subjects studied within water entry outside of cavity formation and dynamics, and also show how geometry or surface condition or both can affect the water entry event within each subject.

1.2.1 Forces at impact

Geometry and surface condition not only affect the cavity dynamics, but also the forces and pressures experienced at impact. Projectiles with blunter nose shapes experience greater reductions in velocity during water entry, while more streamlined projectiles experience less of a reduction in velocity [10], [11]. Bodily et al [12] compared the impact forces between three different axisymmetric nose shapes (flat, ogive, and cone) with both hydrophobic and hydrophilic surface conditions. They found that the flat shape experienced impact forces 10 times those experienced by either the ogive or narrow cone (21˚ cone angle). They did not, however, find a significant difference in impact force between the two surface conditions.

The surface condition can however affect the forces experienced by a sphere through the initial stages of entry if it causes a cavity to form. Truscott et al. [13] studied the forces acting on a sphere in both cavity and non-cavity forming cases during the initial stages of water entry.

They used a hydrophobic coating to alter the wetting angle and induce cavity formation and found that the forces experienced by the cavity forming sphere were significantly less than the unsteady forces experienced by the non-cavity forming sphere. The unsteady forces on the sphere in the non-cavity forming case were attributed to the growth and shedding of vortex structures. This showed that a projectile will experience lower forces during entry if it forms a cavity as opposed to entering without forming a cavity.

These studies show that the geometry of a projectile will directly influence the impact forces it experiences, while the surface condition can influence forces throughout the entry by facilitating cavity formation.

1.2.2 Trajectory and stability

Projectile surface condition and geometry also affect projectile underwater trajectory and stability. Hydro-ballistic stability has also been studied in great detail, and the main focus is how well a projectile can maintain a straight course once it enters the water.

Surface roughness can contribute to underwater instability. Shi and Takami [14] studied the high speed entry of bullets (ogive with a cylindrical tail) and found that the surface roughness of the projectile caused the turbulent boundary layer to separate earlier than theoretically predicted, and that the separation of the boundary layer was responsible for the observed trajectory deflection.

Inconsistent surface condition (wetting angle) on the projectile can also lead to trajectory deflections. Truscott and Techet [15] studied spheres with a hydrophobic coating on only half of the nose and found that the difference in surface conditions caused the sphere's trajectory to deviate after impact. They explained that the hydrophobic half formed an air cavity, while the hydrophilic side did not. The cavity reduced the drag force on the hydrophobic half of the

projectile and consequenly caused the deviation. Bodily et al [12] studied partially coated axisymmetric projectiles and found results similar to Truscott and Techet [15].

Geometry also affects underwater stability. Projectiles with flat nose shapes are fairly stable at high velocities [1], [7], whereas projectiles with ogive, or hemispherical nose shapes are less stable [16]. Bodily et al. [12] studied underwater stability at lower entry speeds and also found that the flat shape was much more stable than the ogive or conical nose shapes. They explained that the comparatively long nose lengths of the ogive and cone nose shapes created a greater moment couple between gravity acting on the center of mass and the center of pressure acting on the nose region.

Geometry affects underwater stability largely from the balance of forces acting on the nose region and the center of mass. The surface condition can affect stability through separating the boundary layer in high-speed entry, or by forming asymmetrical cavities.

1.2.3 Acoustics

The last main focus of water entry outside of cavity formation and dynamics is acoustics. One of the main questions with acoustics is what aspect of the entry creates the most noise and what factors influence it? The sound generated from an impact of a sphere with the water surface is significantly louder when a cavity is formed [17]. Except in the case of blunt bodies, the pinch off of the cavity is the loudest part of the entry [12], and may be explained by the supersonic flow of air that is formed as the cavity pinches off [18]. Uber and Fegan [19] studied the acoustics of several differently shaped projectiles and found that the oscillations of the air cavity created the most predominant aspect of the acoustic signature.

Overall the geometry of the impacting shape affects the acoustics of water entry either at initial impact (as with blunt bodies) or later through the shape of the cavity it creates and its

subsequent collapse. The surface condition also affects acoustics through its influence on cavity formation.

While forces, trajectory, and acoustics are in and of themselves beyond the scope of the current study they are each affected by geometry, surface condition, or the subsequent cavity facilitated by geometry or surface condition. It is reasonable to assume then that greater insight into the effects of nose shape and surface condition would be beneficial to many facets of water entry research. The effects of geometry and surface condition on the specific topic of cavity formation will be discussed in the following section and well help elucidate the purpose of this thesis.

1.3 Background and motivation

Cavity formation is important to many subjects within water entry. As shown earlier the presence of a cavity can affect forces, trajectory, and acoustics. The conditions under which a projectile will form a cavity is therefore of particular importance.

Water entry has been studied for well over a century. Worthington studied droplet impact in milk by drawing sketches in 1877 [20], and then with single spark photography in 1896 [21] Twelve years later he studied the impact of spheres into water and their resulting cavity [21]. He classified the impacts of the spheres as rough and smooth (cavity and no cavity respectively) and found that the transition between the two occurred with increasing drop heights. He also found that a smooth impact could be maintained at increasing drop heights after careful polishing of the sphere, and reported that the water entry event had a strong dependence on the surface of the sphere. Forty three years later May [22] built off Worthington's work and studied the effect of surface coatings on a sphere and the velocity at which the coated sphere would form a rough entry (water-entry cavity). He tested various liquid coatings and found that contamination from

handling the sphere had the most pronounced effect on lowering the transition velocity between smooth and rough entries. He found that the distinction between the two was not always definite and that there were intermediate cases where the cavities were very small or only consisted of a small cloud of bubbles. He also found that under seemingly identical situations the cavity size would differ or not form a cavity at all. He also noted that no extreme precautions were taken to obtain perfectly clean surfaces, and that grease could have been present in the cleaning agents. Although he did not directly state the connection, it is possible that surface contaminants could explain the inconsistencies he noted in cavity formation, based on his own statements that surface condition affects cavity formation. To facilitate locating the transitional (threshold) velocity for cavity formation he plotted maximum cavity size versus velocity separately for the different sphere sizes. Duez et al. [17] also studied the threshold velocity for cavity formation of spheres. They found that the threshold velocity is dependent on the advancing contact angle of the impacting body and is not dependent on body diameter or gas pressure.

Zhao et al. [23] studied the entry of roughened spheres and found that they formed cavities at velocities well below those predicted by Duez et al [17] in the hydrophilic regime. They reported that the failure of a flow to wet a surface, and subsequently not form a cavity, is promoted by surface roughness. They showed that dynamic wetting on a rough hydrophilic surface can be similar to the wetting on a hydrophobic surface by characterizing the rough surface as a smooth surface with a series of capillaries. As the flow moves across the capillary interface the flow will behave like a hydrophobic coating if the time to fill the capillary exceeds the time for the flow to move across the interface. When that occurs the flow moves across a solid-liquid-gas composite surface and operates in a Cassie-Baxter state and exhibits a hydrophobic contact angle. Thus at a low wetting velocity the roughness of a hydrophilic surface

will enhance the wetting process, but as the velocity increases to a critical value the surface roughness will inhibit wetting and cause the surface to perform as though it was hydrophobic [9]. Zhao et al. [23] used a Cassie Baxter wetting angle approximation to correct the measured wetting angle of the roughened spheres. With this corrected wetting angle their results found agreement with the threshold velocity prediction made by Duez et al. [17]

Ding et al [24] investigated contact line pinning and its relation to cavity formation and cavity evolution for spheres and cylinders using experimental, numerical and theoretical analysis. They found that the contact line pinned above the equator of the sphere and on the side of the cylinder and not exactly at the hemisphere and corner as previously thought. They found in their simulations that flow separation happened in conjunction with pinning a contact line in all cases and that there is a pinned meniscus in between the flow separation point and the pinned contact line. They also investigated the geometric effect of spheroid objects, as well as disks and cylinders, (in the hydrophobic regime) on the critical Weber number for cavity formation. They stated that the geometry affects pinning of a contact line by how it affects the bending of the pinned meniscus as well as the value of low pressure in the fluid.

Kubota and Mochizuki [25] studied the splash formed by dropping a sphere into water and classified the different splash stages as a function of velocity. They found that the film flow along the sphere during impact separated earlier (lower on the sphere body) as the velocity was increased. They noted that the initial film separation is a result of the competition between the centrifugal and adhesive forces acting on the film flow. Kubota and Mochizuki [26] later studied the effect of the tail shape of an impacting body. They found that the connecting line between the tail and the nose affected the film flow. They pointed out that the relation between the film flow and the tail of the body is important for the formation of the air cavity. Kubota and Mochizuki

[8] further studied the effect of nose shape on splash formation. They found that different nose shapes produce a distinctive displacement of water in front of the head, which leads to different manners of film flow separation from the surface of the impacting body. They stated that the position where the film flow separates from the body coincides with the position where the air cavity adheres to the body and that the generation of the air cavity starts from the end of the nose part (for projectiles with a hemispherical tail). These papers by Kubota and Mochizuki give insight as to the difference in cavity formation between spheres and axisymmetric projectiles. Not only do they show that the projectile nose affects the flow of the water in front of and on the nose, they also show that the connecting line between the nose and tail affect the film flow separation. This helps explain why the onset of cavity formation in the entry of an axisymmetric projectile is different from that of a sphere. Even with the same nose shape the entry will be different between a sphere and an axisymmetric shape because the cylindrical shaft following the nose region of the axisymmetric shape creates a different connecting line between the nose and the tail.

Relatively few studies have focused on concave shapes, but those that have offer valuable insight. Mathai et al [27] compared the entry of a convex hemisphere and a concave hemisphere nose shape. They studied these shapes with two different diameters (2.54 cm and 5.08 cm) and two different impact speeds (7 and 10 m/s). They recorded pressure measurements inside the cavity with an embedded pressure transducer. They found that the pressure experienced by the concave shape is lower at impact than a convex shape. They also found that the concave nosed body experiences a sudden rise in pressure at impact followed by oscillations that damp out gradually. Truscott et al. [1] pointed out that a concave nose shape will form a small cavity that wraps up quickly and descends with the tip of the projectile. These two studies reveal that the

concave nose shape produces a uniquely shaped cavity that oscillates in pressure. Figure 1-3 compares the entry of a convex and two concave geometries. The figure shows how the cavities are different between the convex and concave geometries in both shape and size.

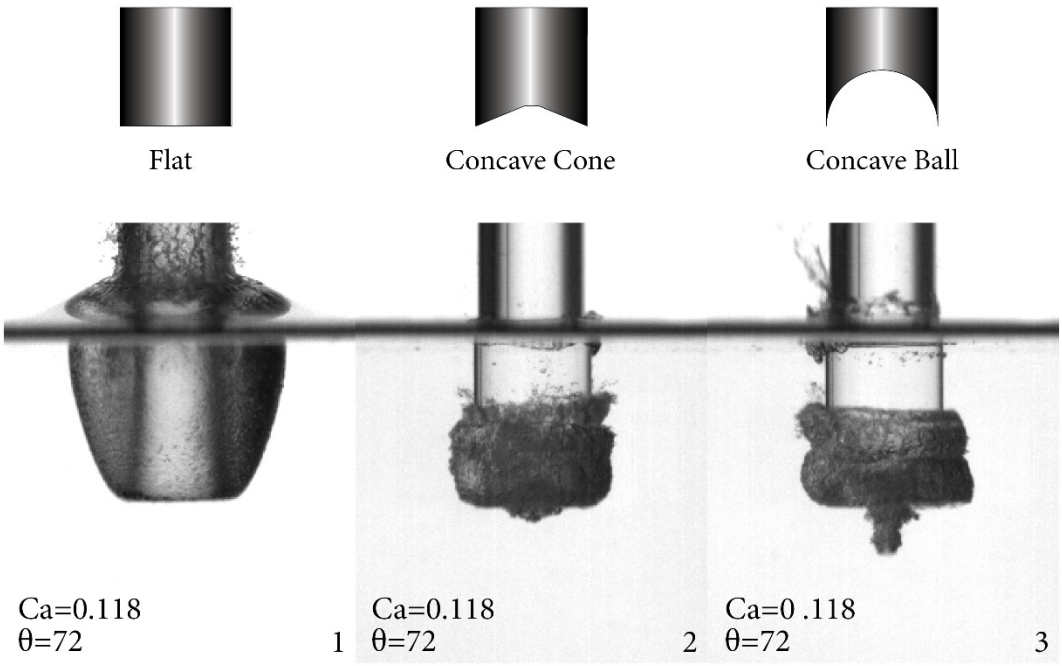

Figure 1-3. Comparison of the cavities made by a convex geometry (flat) and two concave geometries (cone and ball). Impact speed =7.06 m/s. Ca= 0.118, and wetting angle (θ) =72˚. Notice that the cavities made by the concave geometries have a different shape and are much smaller than the cavity formed by the convex geometry. Representative geometries are shown above the cavity images.

In the entry of drops and spheres, the surface of the water deforms slightly just before the object impacts the water surface due to the high-pressure air trapped in the narrow region between the two. The deformation of the water surface causes the sphere or droplet to entrain a small amount of air at impact [28], [29], [30]. Takagi and Dobashi [31] studied the influence of trapped air on ship sections using a deformed plate to intentionally trap air between the water and the structure. They pointed out that the trapped air creates a complicated problem because the

water and trapped air act as a spring and mass system. They found that the trapped air increases the impact force experienced by the impacting structure.

1.4 Objectives

Though much is known about cavity formation and the resultant effects of geometry on various aspects of water entry, there is still a lack of understanding associated with the effect an axisymmetric nose shape followed by a cylindrical shaft has on the threshold velocity for cavity formation. There is also relatively little information on the effect a concave nose shape has on cavity formation. The research presented here focuses on the effect of convex nose shape on the threshold velocity for cavity formation for both hydrophilic and hydrophobic projectiles, and for a variety of convex nose shapes. This research also investigates the formation of cavities in the wake of concave nose shaped bodies in terms of impact velocity, geometry of the concave shape and wettability of the projectile.

2 EXPERIMENTAL METHODS

The purpose of the research was to determine the effect of nose shape, both convex and concave, on the water entry cavity through a range of impact speeds and wetting angles. The experiment involved the impact of cylindrical bodies (projectiles) with the water surface, and the configurations that were tested consisted of combinations of five main nose shapes, four surface conditions, and two materials as shown in Table 2-1. The different nose shapes represent various slender-body nose geometries, three commonly seen in the literature (cone, ogive and rounded flat) and some less common (concave cone and concave hemisphere). Surface coatings were varied to show the effect of wettability. The two materials used offer slightly different densities in addition to two surface conditions. High-speed cameras were employed to capture the rapid entry of the projectiles and subsequently analyze their effect on cavity formation. Particle Image Velocimetry (PIV) was also used to qualitatively investigate the unique flow field variations between the concave nose shapes and the convex ones. Drop heights were varied to determine the impact speed at which cavities were formed, as well as investigate the cavity formed by the concave shapes through a range of impact speeds. These various factors affected the dimensionless parameters used herein: capillary number ($Ca = \mu U_0 / \gamma$), Reynolds number ($Re = \rho U_0 D / \mu$), Weber number ($We = \rho U_0^2 D / \gamma$), Froude number ($Fr = U_0 / \sqrt{gD}$) and Bond number ($Bo = \rho g D^2 / \gamma$) (ranges shown in Table 2-1).

Table 2-1. Various nose shapes, materials, surface conditions, drop heights and dimensionless numbers varied in this study.

Nose shapes	Materials (density g/cm^3)	Surface conditions	Impact velocity range (m/s)	Non-dimensional number ranges	
Cone,	Aluminum, ρ= 2.70 Acrylic ρ= 1.18	Hydrobead® θ = 164, Cytonix WX 2100® θ=162, Parrafin wax θ = 108, Polished/Uncoated θ = 72, 80, HydroPhil® θ = 15-33	0-15.07	Capillary #	~0-.023
Ogive,				Reynolds #	~0-342,000
Rounded Flat,				Webber #	~0-78,600
Concave cone,				Froude #	~0-30.199
Concave hemisphere				Bond #	86.14

2.1 Experimental setup

High-speed cameras were used to capture the water entry of a projectile and subsequent cavity formation. Particle Image Velocimetry (PIV) is a flow visualization technique that employs a high power laser, and a high-speed camera to illuminate particles in the water and then compare the position of the particles in time, resulting in a vector field estimate [32]. This technique was used to visualize the flow of water around the nose of the shapes upon impact with the water and correlate some of the unique cavity formations with velocity measurements.

Experimental drop testing was performed by holding a cylindrical projectile above the water surface with an electromagnet attached to an aluminum framework mounted above a glass tank of water (0.9 m X 0.9 m X 1.2 m) filled to 0.6 m with filtered tap water, Figure 2-1. A light-bank was placed behind the glass tank opposite of the camera, and on the side of the tank to provide back and side lighting on the projectiles for the high-speed imaging. Each light-bank

consisted of an array of 20 fluorescent lights attached to an aluminum plate with a diffuser screen to provide even lighting.

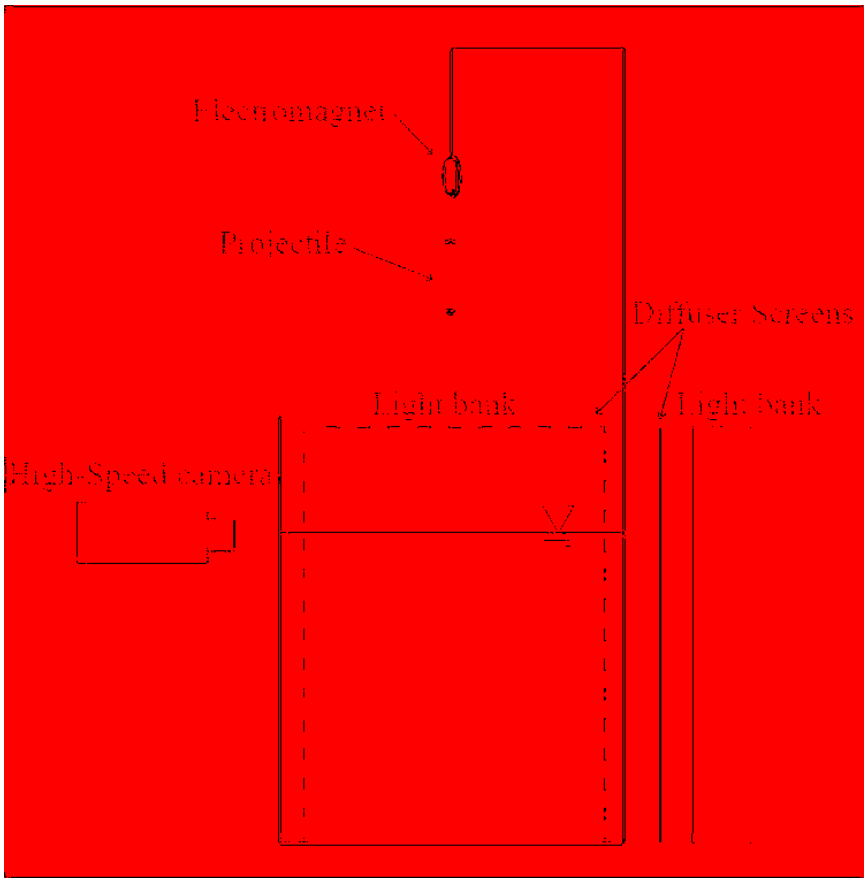

Figure 2-1. Diagram of the experimental setup. The projectiles were suspended from an electromagnet and released when the power to the electromagnet was reduced. Light banks with diffuser screens were placed behind and to the side of the tank to provide back and side lighting to provide contrast and illuminate the cavity.

A Photron SA3 high-speed camera was used to film the entry events at 2000 frames per second (fps) with a 1/7500th shutter speed, and was used for a majority of the drop tests. A Phantom v1612 using a frame rate of 7500 fps was also used to investigate the ring-cavity formed by the concave nose shapes. The images from the drop tests were visually inspected to

monitor cavity formation. The cameras were positioned level with the free surface of the water for a majority of the tests, but for a few special cases they were positioned above and below the water surface.

For PIV measurements the tank was seeded with Dantec® polyamide seeding particles having a mean particle size of 20 μm, and a density of 1.03 g/cm^3, making them neutrally buoyant. The laser was equipped with a prism lens to create a 2-D plane of light and operated at a frequency of 10,000 Hz and a current of 20 Amps (power level control). The laser timing is illustrated in Figure 2-2. A Phantom v2410 High-speed camera was used to record the event at 5,000 fps with a 2 image PIV burst mode, giving an effective frame rate of 10,000 fps. Two different image pairs could have been used from the data collected, one with a time spacing (dt) of 20 μs, and the other with 180 μs. The larger dt was used to allow sufficient particle movement (about 10 pixels between image pairs) for accurate PIV results.

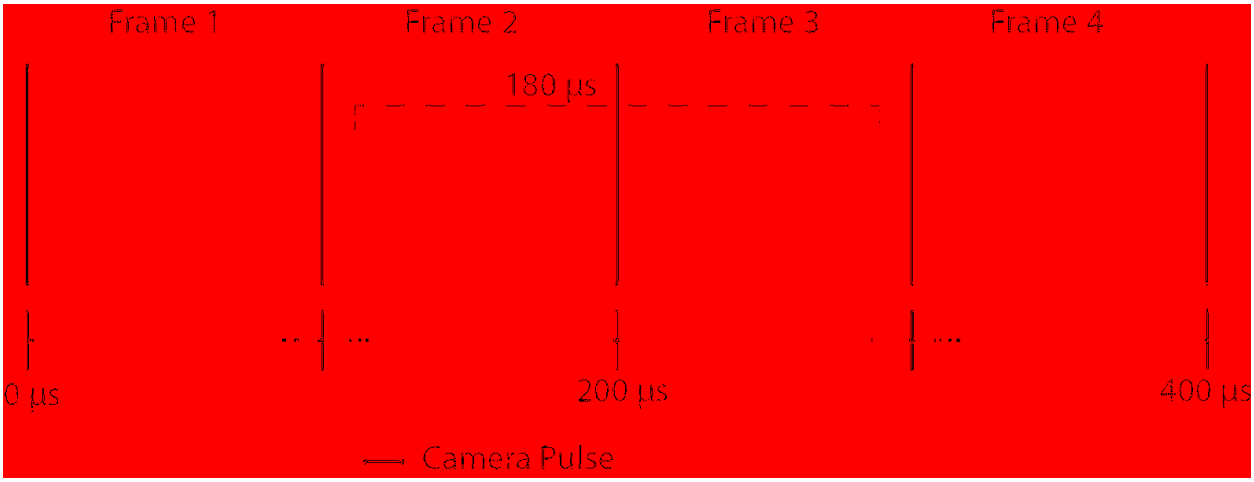

Figure 2-2. Illustration of the camera and laser pulse timing used to obtain the PIV data. The time between images (dt) was 20 μs and 180 μs (dashed line). The 180 μs image pairs were used for the PIV study.

Images from the PIV experiments were processed with MATLAB using the program PIVlab [33] to track the particle motion and determine the flow velocity, and vorticity. To process the PIV data 3 passes were used with window sizes of 128, 64, and 32 pixels each. Within a 32 pixel window there was as average particle density of 7 bright particles. The data was filtered by removing vectors that were significantly different from their neighbors and replaced with the neighboring average.

2.2 Testing procedures

2.2.1 Camera alignment

The camera was set up and aligned as follows:

- Step 1, place camera on tripod.
- Step 2, set camera so that front face is 52 inches from tank (measure this from both edges of the camera housing to ensure it is aligned perpendicular to the tank).
- Step 3, plug in power supply cable, Ethernet cable, and umbilical cord to the camera.
- Step 4, connect pickle switch to “trigger in” port on the umbilical cord and connect Ethernet cable to laptop.
- Step 5, turn on the camera, laptop, and PFV software. The software should automatically detect and display the camera (if not see the steps for “camera not detected”).
- Step 6, turn on light banks.
- Step 7, set up PFV software settings: set *Frame Rate* to “2000 fps”, *Resolution* to “512x768”, and *Shutter* to “1/7500”. Then set *Trigger Mode* to “center”. With the lens cap on the camera select *Shading* and click “Calibrate”, then remove the camera lens. Under the Data Save tab under save path select the axi_cavity_formation folder.

- Step 8, hang the calibration target from the electromagnet and place in the tank just below the surface of the water.
- Step 9, adjust aperture settings until the image displayed in PFV is light but not washed out, (the aperture can be set part way in between settings, generally between 5.6 and 11).
- Step 10, adjust horizontal position of camera so that the target is visually in the center.
- Step 11, adjust the pan so that the target is in the center of the screen and there is no distortion in the string as it descends into the water.
- Step 12, adjust elevation of camera until the water level is 1/3 down the screen.
- Step 13, adjust tilt so that the camera is level with the water (the water level will appear as one line).
- Step 14, adjust the camera focus until the target in the water as well as the string above the water are in focus, taking care that the target is in focus above all else.
- Step 15, if spots are on the glass take a razor and carefully scrape them off.

Troubleshooting: If the PFV software states that the camera is not detected first check the Ethernet cable. Then turn both the camera and the software off and on again, making sure the camera is turned on before the software program. If PFV does not automatically detect the camera and the screen comes up blank the IP address may not be configured correctly. To remedy this, go to the start menu, open the control panel, network and internet and under the network and sharing center click view network status and tasks. Under active networks click local area connection, click on properties, select internet protocol version 4 click on properties, type in IP address “192.168.000.010” and subnet mask “255.255.255.000” click ok and close out of the network connections.

2.2.2 Drop test procedure

The step by step experimental procedure is as follows:

- Step 1, turn on electromagnet.
- Step 2, attach projectile to electromagnet and wait until visibly motionless, also ensure there is no disturbance in the surface of the water in the tank.
- Step 3, In the PFV program go to the live tab, click record, and then trigger. The camera should now be recording.
- Step 4, slowly turn down electromagnet power until projectile drops.
- Step 5, trigger the pickle switch or click on the green “endless record” button when the projectile hits the water.
- Step 6, turn off the electromagnet.
- Step 7, replay the video and clip the video to the frame where the projectile enters view and to when it leaves.
- Step 8, name video with this filename structure “material_shape_coating (0 if none, 1 if Hydrobead®, 2 if wax, 3 if Hydrophil®, and 4 if Wx2100®)_angle at entry(0 unless doing angled studies)_drop height_drop number (for repeat tests). For example “al_ogive_0_0_10_3” means aluminum ogive, no coating, vertical entry (no angle), 10 inches distance between tip and water surface, 3rd run.
- Step 9, save the file as a series of tiff images.
- Step 10, place glove on one hand and retrieve the projectile using the magnet stick.
- Step 11, blow off projectile with compressed air. Follow projectile preparation for new projectile and repeat these steps.

2.3 Projectile details

2.3.1 Machining procedure

Each projectile in the study is 5.5 inches long and 1 inch in diameter. Each shape was modeled in SolidWorks and the three convex shapes were machined on a CNC lathe. The concave cone shape was made with a 1 inch diameter drill bit, having an 118˚ tip, to hollow out the nose area and the concave ball shape was respectively formed with a 1 inch diameter ball end mill. The projectiles were made out of aluminum and acrylic. The aluminum projectiles were wet lapped in steps after machining with 400 grit sandpaper and #2/0, and #4/0 (equivalent 1200 and 2000 grit) Emery polishing paper. The acrylic projectiles were likewise wet lapped after machining with #2/0, and #4/0 Emery polishing paper and given an additional surface finish using an acrylic polishing compound and a fine polishing wheel to ensure a smooth, transparent finish.

2.3.2 Convex shapes

Three main convex shapes were used in the study consisting of a cone, an elliptical ogive, and a rounded flat shape as shown in Figure 2-3. These shapes are similar to those used by Bodily et al. [15] with the exception that the cone shape has been given a narrower tip. They are representative of basic geometric shapes that have been streamlined, having no sharp corners, and immediately followed by a cylindrical shaft. This combination of nose shape with a following shaft has been used in many studies [1] [4] [7] [12] [16] [34].

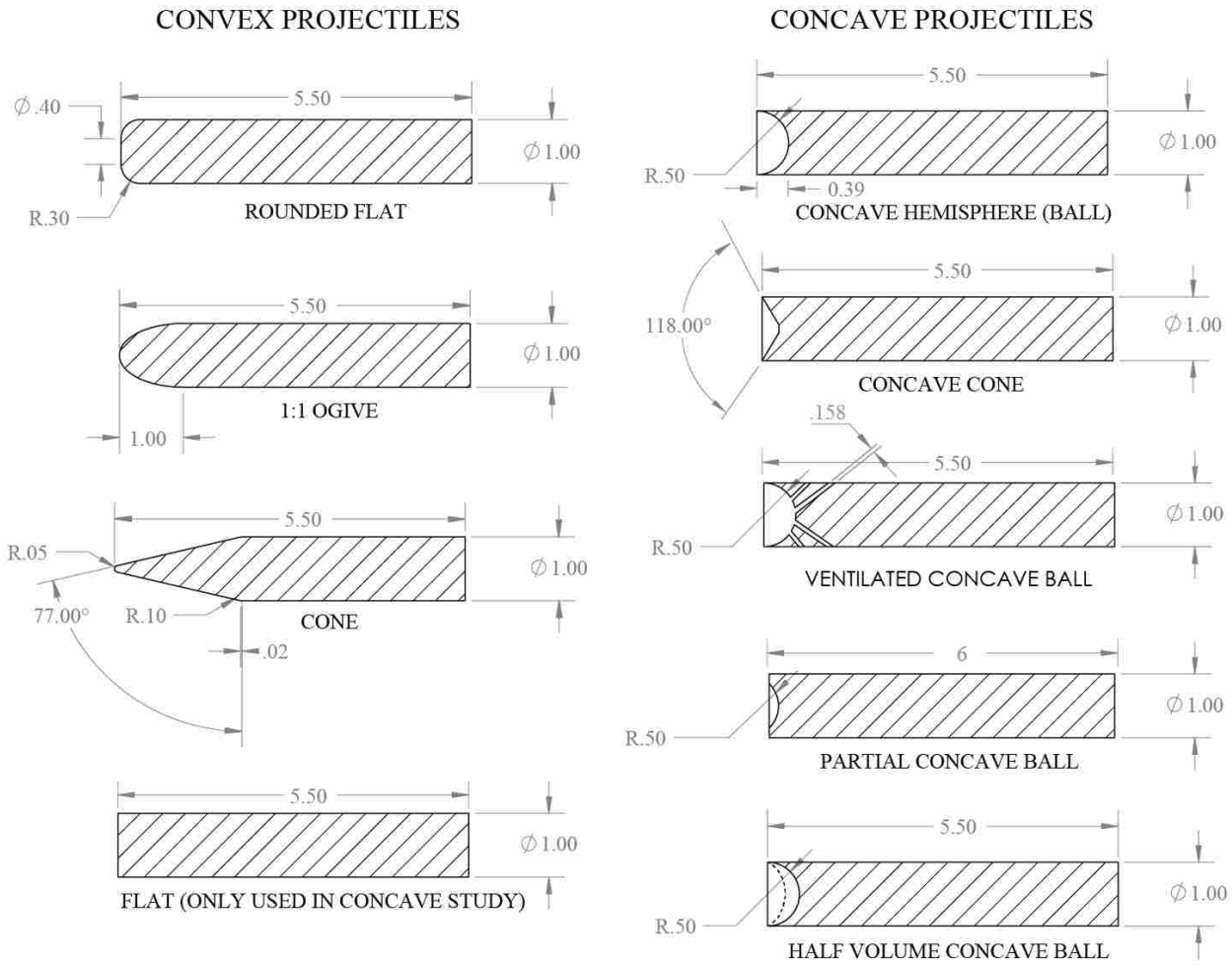

Figure 2-3. Cross-section of the shapes used in the study (dimensions are given in inches). The elliptical ogive is a parabolic shape with the nose length equaling the diameter and the curvature is determined by the equation: $y = 0.5\sqrt{1 - x^2}$. The cone has a slightly rounded transition from the nose to the shaft as well as a hemisphere for the tip. The convex shapes are the same studied by Bodily et al. [12] with the exception of the cone. The cone has the same nose length but a sharper point. The flat can be thought of as having zero concavity and was used for comparison with the concave shapes. The partial concave ball, the ventilated concave ball and the half volume concave ball were special variations of the concave ball used for case specific comparisons.

2.3.3 Concave shapes

Six shapes were used to study the cavity formation of concave shaped projectiles: concave ball, concave cone, flat, partial concave ball, ventilated concave ball and a half-volume

concave ball as shown in Figure 2-3. The concave ball and concave cone were the main focus of the study with the other shapes used for comparison. The concave ball and concave cone both have cutouts that reach the outer edge of the diameter. The flat shape has no concave shape and is compared for reference. The ventilated cone shape was made identical to the concave ball with the exception of 8 shafts, 1.6 mm in diameter each, drilled from the concave portion to the outer shaft. This allowed the air within the concave shape to vent out so that the role of the trapped air in the concave shapes could be determined. The partial concave ball has the same curvature as the concave ball but only takes up part of the bottom face, leaving a portion of the bottom face flat. The half volume concave ball was made by filling half of the volume of the concave ball with a tacky polymer, giving the relative shape of the dashed region in Figure 2-3.

2.3.4 Surface conditions and coating procedures

The two superhydrophobic surface conditions were respectively attained using Hydrobead™ and Cytonix WX2100™ spray coating and the hydrophobic coating was attained with a dip coating in paraffin wax. The two hydrophilic surface conditions came from the clean, polished material surface and Lotus Leaf's HydroPhil™ super-hydrophilic coating. Each combination of material, nose shape, and surface condition was tested within the range of impact velocities given in Table 2-1. Specific procedures for the various cleaning and coating methods follow.

Uncoated projectiles were cleaned previous to each drop to ensure wetting angle consistency. While wearing a new pair of latex gloves each was rinsed with isopropanol and wiped vigorously with Kimtech Kimwipes® to remove any particulates and oils and then rinsed

again with isopropanol and blown dry with compressed air. They were immediately rinsed with ethanol and dried again with compressed air.

Hydrobead™ and Cytonix Wx2100™ superhydrophobic coatings were applied according to the manufacturer's specifications with several coats to ensure hydrophobicity and durability.

Wax was applied by dip coating the projectiles in molten wax. After dipping, the projectiles were immediately inverted to give the nose area a uniform coating. Inconsistencies in the coating near the back end of the projectile were removed with a razor. No further action was taken to perfect the coating as only the nose area would affect the cavity formation. Care was taken to visually inspect each coating and reapply as needed until a visually uniform coating in the nose area was achieved. The wax projectiles were also handled with gloves to minimize contaminating the surface. Due to the soft nature of the wax, the coating was removed and reapplied after every drop to keep the conditions consistent.

The super-hydrophilic coating was obtained by using Lotus Leaf's HydroPhil™ coating. The projectiles were dip coated in the solution and allowed to air dry. This process was repeated three times to ensure a consistent coat because a single coat produced inconsistent results.

2.4 Wetting angle and surface roughness

The contact or wetting angle is a way to measure the wettability of a surface. There are various methods of measuring the wetting angle all giving a slightly different perspective on how the material wets with a particular liquid. Wetting angle measurements were made using a Rame-Hart Contact Angle Goniometer using the dynamic Seissle drop method [35]. Figure 2-4 illustrates the underlying measurement where a drop of liquid is placed on a surface and the

interior angle of the liquid drop is measured as the wetting angle. The uncertainty analysis for the wetting angles is given in Appendix A.

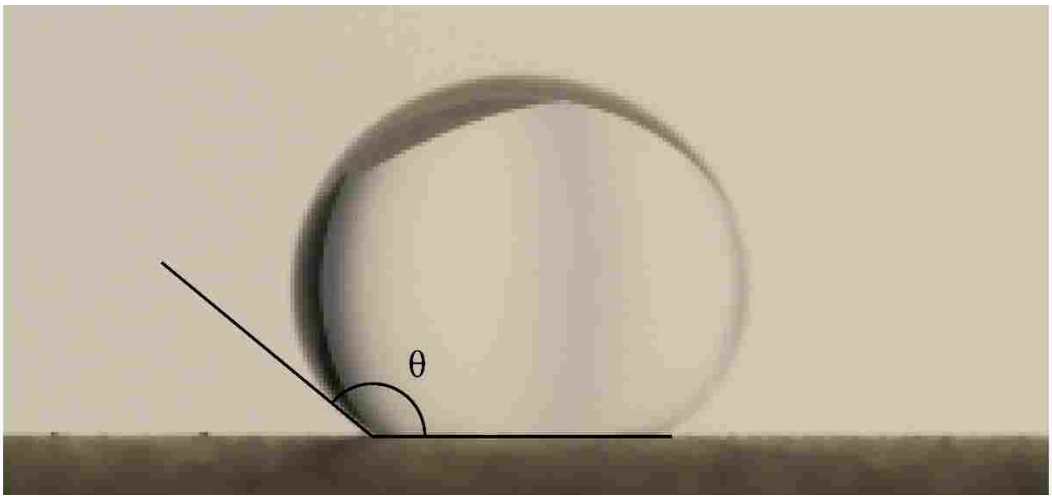

Figure 2-4. Wetting angle measurement. The interior angle is used for the wetting angle and is measured from the bottom of the drop to the edge, as shown in the figure.

Several test sample discs were machined from the same stock and machining procedure as the projectiles to facilitate measuring the contact angles of the different surface conditions used in the study. To determine similarity between the samples and the projectiles, surface roughness measurements were taken of both the sample and the projectiles. As seen in Table 2-2 the average roughness values are similar for the projectiles and samples, because of this we assume the wetting angle measured on either would be relatively similar and we use the wetting angle of the samples for the surface conditions. The surface roughness of the samples and projectiles, as well as the advancing dynamic wetting angle of the samples were averaged over 12 data points and are summarized in Table 2-2.

Table 2-2. Roughness values for projectiles and samples. Advancing wetting angles are shown for the samples. Both roughness and wetting angle are averaged over 12 data points. The bolded wetting angles indicate the values used in the study. They were selected based on the direction of the flow in relation to the machining lines on the projectiles to give the most similar wetting angle between the samples and the actual tests. Perpendicular and parallel indicate if the wetting angle was measured perpendicular to or parallel with the machining lines on the samples.

Coating	Material	Sample		Roughness (μm)			Advancing wetting angle (˚) +/- uncertainty
				Ra	Rq	Rz	
Uncoated	Aluminum	Projectiles	Cone	0.082	0.108	0.678	
			Ogive	0.082	0.104	0.628	
			Rounded flat	0.076	0.102	0.610	
		Average		0.080	0.105	0.639	
		Samples	Perpendicular	0.102	0.136	0.844	**80.1 +/- 7.8**
			Parallel	0.097	0.134	0.696	71.8 +/- 10.4
		Average		0.100	0.135	0.770	76.0 +/- 11.3
	Acrylic	Projectiles	Cone	0.046	0.062	0.344	
			Ogive	0.058	0.082	0.330	
			Rounded flat	0.056	0.078	0.482	
		Average		0.053	0.074	0.385	
		Samples	Perpendicular	0.043	0.054	0.283	72.7 +/- 5.5
			Parallel	0.046	0.063	0.323	**71.8 +/- 5.7**
		Average		0.044	0.059	0.303	72.2 +/- 5.5

Surface roughness was measured using a Hommelwerke LV-100/150 profilometer with a TKU 300/600 measuring arm for a variety of parameters including Ra, Rq, Rz, and Rmr. The prefix “R” denotes that the values are determined from the roughness profile, which is filtered from the primary profile to remove the waviness of the profile from the measurement. There are 5 sample lengths within an evaluation length and the centerline within a sample length is the reference line for each measurement. Each measurement is averaged over the 5 sampling lengths. Ra is the arithmetic mean of the deviations of the roughness profile. Rq is the root mean square of the deviation of roughness values from the centerline and corresponds to the standard

deviation of the profile values. Rz is the vertical distance between the highest and lowest point within a single measuring length. Rmr is the material ratio which is defined as the sum of peak widths at a given height within the roughness profile. These definitions were summarized from chapter 9 in the Hommelwerke Turbo Roughness operating manual [36]. The interested party may refer to that document for further definitions and figures explaining the measurements. For the purposes here the material ratio was calculated at the reference line within the roughness profile. The reference line was assumed to be the height of the ideal smooth surface and the Rmr measurement gave the proportion of material present at that height. The evaluation length was 4.8 mm (equal to 5 single measuring lengths), the measuring speed was 0.5 mm/s, and the vertical measuring range was 80 μm. The roughness values of the surface conditions as well as the associated advancing wetting angle were averaged over 12 data points and are summarized in Table 2-3. Note that the wax coating was too soft to obtain reliable roughness measurements.

Table 2-3. Summary of average roughness and wetting angle values measured for the projectiles and samples. Each value was averaged over 12 samples. Ra is the arithmetic mean of the roughness, Rq is the root mean square of the roughness, Rz is the average peak to valley height, and Rmr is the material ratio at the roughness reference line.

Coating	Material	Roughness (μm)			Material Ratio	Advancing wetting angle (˚)
		Ra	Rq	Rz	Rmr	
Uncoated	Aluminum	0.100	0.135	0.770		80.1 +/- 7.8
	Acrylic	0.044	0.059	0.303		71.8 +/- 5.7
Parrafin Wax	Aluminum	NA	NA	NA		110 +/- 4.1
	Acrylic	NA	NA	NA		108 +/- 6.2
Hydrobead®	Aluminum	0.642	0.988	5.323		165.9 +/- 4.6
	Acrylic	0.855	1.252	6.507		162.1 +/- 5.1
Cytonix Wx2100®	Aluminum	2.608	3.773	18.277		161.3 +/- 3.3
	Acrylic	2.125	2.975	14.163		163.1 +/- 4.5
Lotus Leaf Hydrophil®	Aluminum 1 coat	0.135	0.179	1.081		32.9 +/- 42.7
	Aluminum 3 coats	0.251	0.354	2.128	0.45 +/- 0.12	15.1 +/- 9.6
	Acrylic 1 coat	0.106	0.163	0.778		22.7 +/- 7.8
	Acrylic 3 coats	0.128	0.186	1.18	0.44 +/- 0.14	16.3 +/- 5.4

The measured wetting angle values for aluminum coincide well with values measured by Bernardin et al. [37]. They measured the wetting angle on polished aluminum at atmospheric pressure that had an average surface roughness of 115 nm. They determined the wetting angle to be about 90˚. They attribute this high angle to the likely presence of organic residue from the polishing process. To determine this they cleaned the samples using methanol and found that the wetting angle decreased to about 78˚ at room temperature. The samples measured in the current study had an average surface roughness of 102 nm perpendicular to the machining lines and were cleaned with ethanol. The average wetting angle measured was 80˚, very close to the average determined by Bernardin et al. [37]. The wetting angle perpendicular to the machining lines was selected because the flow at impact would always act in that direction, making it the best measure of the interaction between the flow and the surface.

The contact angle of acrylic resin was reported by Accudyne on their website as 70.9˚ [38]. Several different acrylic test specimens were also studied by Hilgenberg et al. [39]. Samples with a roughness of 60 nm exhibited a wetting angle of 69 +/- 9˚. Our roughness was an average of 44 nm with a wetting angle of 71.8 +/- 5.7˚, close to the values measured by Accudyne and Hilgenberg et al.

The contact angle of paraffin wax was also reported by Accudyne as 108.9˚ [38]. The average wetting angle for all the wax samples came out to 109.0 +/- 5.4˚ very close to Acudyne's values.

The manufacturers of Hydrobead® and Cytonix wx2100® claim wetting angles >160˚ on their websites and from other sources [41], [40]. The average of our samples are 164 +/- 5.8˚ and 162 +/- 4.6˚ for Hydrobead® and Cytonix wx2100® respectively.

2.5 Capillary number and velocity estimates

The Capillary number was used by Truscott et al. [1] to determine the threshold for cavity formation, and we likewise list it in the cavity formation results. The impact velocity of the projectile, however, is the only variable in the Capillary number for the current study and was used originally by Duez et al. [17]. For this reason the impact velocity is referred to instead of the Capillary number for a majority of the discussion. The uncertainty analysis for the capillary number is given in Appendix B.

The impact velocities were estimated based on their drop height (measured from the tip of the projectile to the free surface of the water) using $v = \sqrt{2gh}$, assuming negligible drag. Velocities were verified by analyzing the motion of a few projectiles and recording the pixel location of each projectile tip through time. Table 2-4 shows the calculated values and the reported values and gives the percent error between them.

Table 2-4. Calculation of impact velocity for a sample of cases based on image processing of the data. Linear fit values were used for the low impact velocities to reduce noise in the data. Above about 5 m/s the entry velocity was relatively constant within the measuring window (10 cm) and the calculated values were sufficient. Values in green are used for the error estimate.

Projectile details		**Impact Velocity (m/s)**			
Shape	**Material**	**Reported** $v = \sqrt{2gh}$	**Derivative of position (dz/dt)**	**Linear fit to position**	**% Error**
cone	acrylic	~0.000	0.212	0.212	100.00%
cone	aluminum	~0.000	0.202	0.156	100.00%
Rounded flat	acrylic	0.250	0.470	0.222	12.30%
torpedo	aluminum	0.250	0.176	0.231	7.86%
ogive	acrylic	0.706	0.564	0.662	6.62%
ogive	aluminum	0.706	0.706	0.669	5.48%
cone	acrylic	2.232	2.117	2.189	1.99%
torpedo	aluminum	4.992	4.939	-	1.07%
torpedo	aluminum	7.059	7.056	-	0.05%
cone	acrylic	7.059	7.056	-	0.05%
cone	acrylic	10.471	10.475	-	0.04%

The data was very sensitive to exact pixel location, and caused scatter in the velocity measurements at low impact velocity. A relatively large percent error was calculated for the low impact velocities, but a much smaller error was calculated for the high impact velocities (less than 2% error). The low velocity data was plotted in Excel® and a linear fit of the calculated velocity values was used to smooth the data. This allowed more accurate impact velocities to be calculated. The impact velocity data at about 5 m/s and higher remained relatively constant within the tracking window (about 10 cm).

2.5.1 Discrepancy at low impact velocity for superhydrophobic tests

Due to the nature of the experimental setup the initial impact velocity for the low entry speed superhydrophobic tests is not the velocity at which the flow separates from the projectile and forms a cavity. For these low impact velocity tests the projectiles were released just above the water surface. While the initial impact velocity was very low, the projectile continued to accelerate as it descended into the water. As a result of the different nose lengths of the projectiles each had a different amount of time to accelerate and consequently a different velocity at cavity formation (when the contact line pinned at or near the end of the nose region), even when at the same impact velocity. To account for this discrepancy, the impact velocities were adjusted by adding the nose length to the drop height of each projectile. To validate this adjustment the drop tests at the threshold velocity for each shape was image processed by hand to calculate the velocity of the projectile at the point the flow separated and formed a cavity, see Table 2-5 for calculated values. One reason the error is high for some cases is because the exact frame when flow separation occurred was difficult to distinguish because the water level meniscus was in the way of the camera focus.

Table 2-5. Difference between reported separation velocity and the calculated derivative of position separation velocity. The reported velocity was adjusted from the impact velocity by adding the nose length of the projectile *The acrylic cone dropped from -1.75D did not form a cavity but its velocity and error is reported to compare with the acrylic cone case that did form a cavity.

Projectile details		**Actual drop Height (D)**	**Impact Velocity (m/s)**	**Adjusted drop height (D)**	**Separation Velocity (m/s)**		
Shape	**Material**				**Reported value**	**position derivative linear fit**	**% Error**
Cone	acrylic	-1.75	-	0.25	0.353*	0.331*	6.23%
Cone	acrylic	0	0	2	0.998	0.922	7.66%
Cone	aluminum	0	0	2	0.998	1.003	0.46%
Rounded flat	acrylic	0.125	0.250	0.425	0.460	0.410	10.98%
Rounded flat	aluminum	0.125	0.250	0.425	0.460	0.394	14.37%
Ogive	acrylic	1	0.706	2	0.998	0.935	6.37%
Ogive	aluminum	1	0.706	2	0.998	0.993	0.58%
Ogive	acrylic	10	2.232	11	2.341	2.347	0.24%

3 RESULTS AND DISCUSSION

3.1 The impact of convex shapes on the threshold velocity for cavity formation

When a projectile enters the water it may form an underwater cavity, depending on several factors including entry speed, wettability, and shape. For a given shape and wettability there is a threshold velocity below which a projectile will not form a cavity and above which will form a cavity. Duez et al. [17] studied the effect of wetting on the threshold velocity for spheres and found that wetting has a significant effect on the threshold velocity. Ding et al [24] investigated the effect of shape on the critical Weber number for cavity formation for discs, cylinders, spheres and spheroid shapes and found that shape also has a significant effect. No studies yet, however, have focused on the effect of axisymmetric nose shapes coupled with a cylindrical shaft on the threshold velocity.

The effect of axisymmetric shape has been studied in great detail by several authors [1] [1] [15] [24] [8]. Nose shape affects both the speed and direction of the water as it is displaced by the entering projectile, consequently affecting how and when the cavity is formed. Figure 3-1 shows the effect of axisymmetric shape on the progression of the underwater cavity. Notice that the cavity size and shape are different for each projectile nose shape. The rounded flat shape forms a fairly wide and large cavity due to its blunt nose shape, shown in Figure 3-1 image series 1. The ogive shape produces a narrower but longer cavity shape than the rounded flat from the

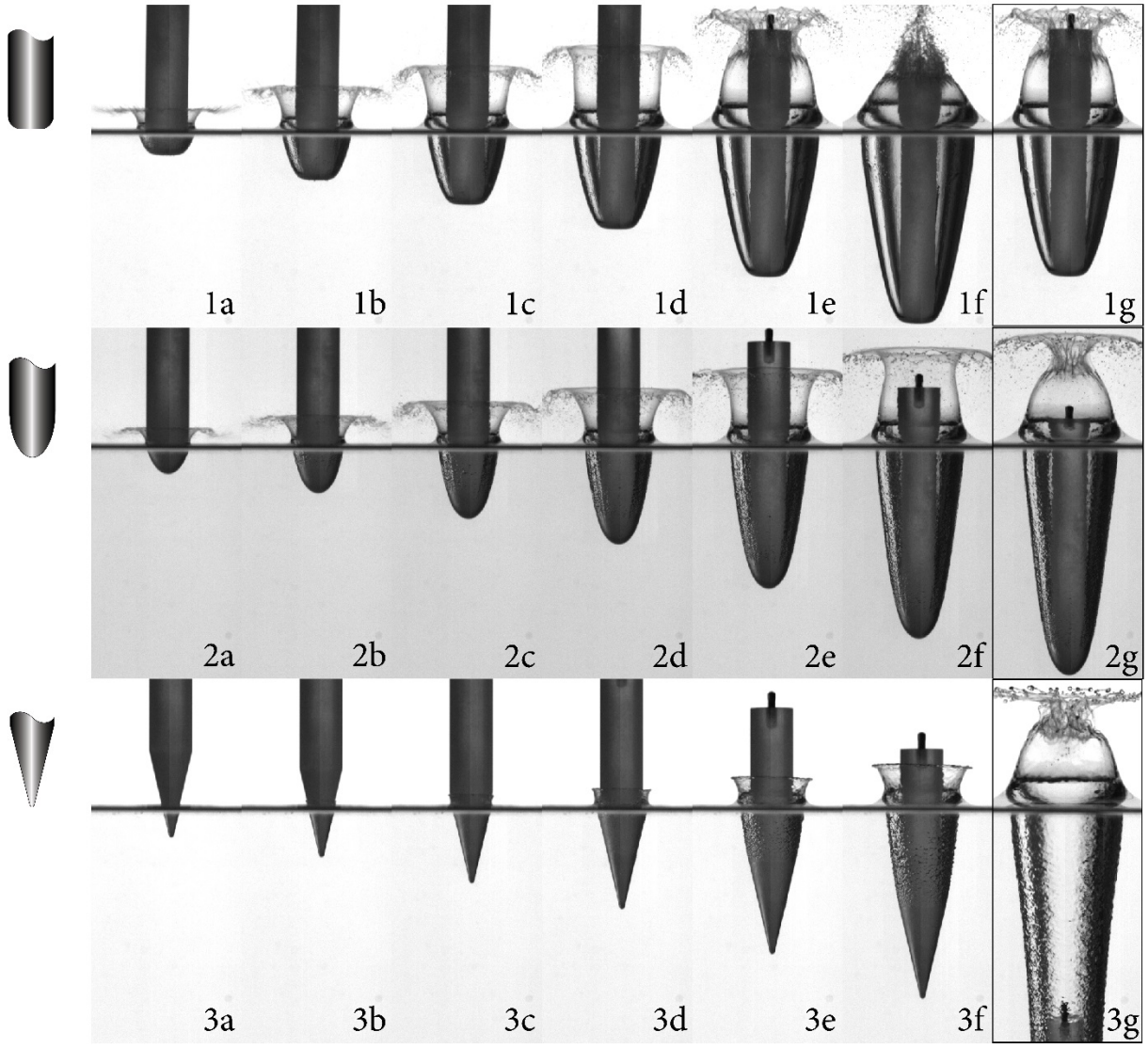

Figure 3-1. Comparison of cavity formation in the wake of three nose shapes: (rounded flat (1a-1g), ogive (2a – 2g) &, cone (3a – 3g). Images a-f were taken at depths of 1/2 1, 1 1/2, 2, 3, and 4 diameters (D) respectively. All projectiles are coated in a superhydrophobic coating (θ=162) and have an entry speed of v= 7.06 m/s (Ca=0.118). The final images on the right (Image series g) are of each of the projectiles at surface seal and the time for each from impact are t=0.0120 s, t=0.0135 s, t=0.0385 s for the rounded flat, ogive and cone respectively. Image series 1 shows the rounded flat entry. Notice the wide and large cavity formed soon after impact for the rounded flat nose shape (1a – 1g). Image series 2 shows the ogive entry. The more elongated nose region forms a narrower cavity. Image series 3 shows the cone entry. The highly elongated nose region delays cavity formation until the projectile is at a greater depth than the rounded flat and ogive shape.

more elongated nose shape, which also lacks corners or flat regions, shown in image series 2. The cone shape, shown in image series 3, has a highly elongated nose shape that allows it to slice though the water with less impact on the flow than the other two shapes. The comparatively long nose region also causes it to delay cavity formation until the projectile is at a greater depth beneath the surface. The cavity formed by the cone is narrow and long and has a considerably longer time to surface seal. Compare the time to surface seal and location of the projectiles in the far right images in Figure 3-1. Notice that the cone shape is no longer in the field of view at surface seal.

3.1.1 Entry behavior leading up to and at the threshold velocity

In between the velocity region where a cavity and no cavity forms there is a transition region where the projectile may form a partial cavity, one where air is only entrained partly around the circumference. Figure 3-2 shows this transition region for the acrylic rounded flat shape with an uncoated surface. Image series 1 shows the entry of the rounded flat shape at a speed just below the transition region where no cavity is formed. Image series 2 shows the cavity progression in the transition region where only a partial cavity forms. Notice that in image 2b there is a region on the nose where air is not entrained and the flow remains attached to the surface of the projectile. Image series 3 shows the cavity progression at the velocity threshold where the cavity is formed fully around the circumference. Notice that the region of impact speeds between which the projectile forms no cavity and forms a full cavity is less than 1 m/s for this particular shape and surface condition.

We now explore how the transition region and threshold velocity change as a result of different wetting angles, and their accompanying surface roughness, for the rounded flat shape as seen in Figure 3-3. The cavity formed at the threshold velocity looks similar between the

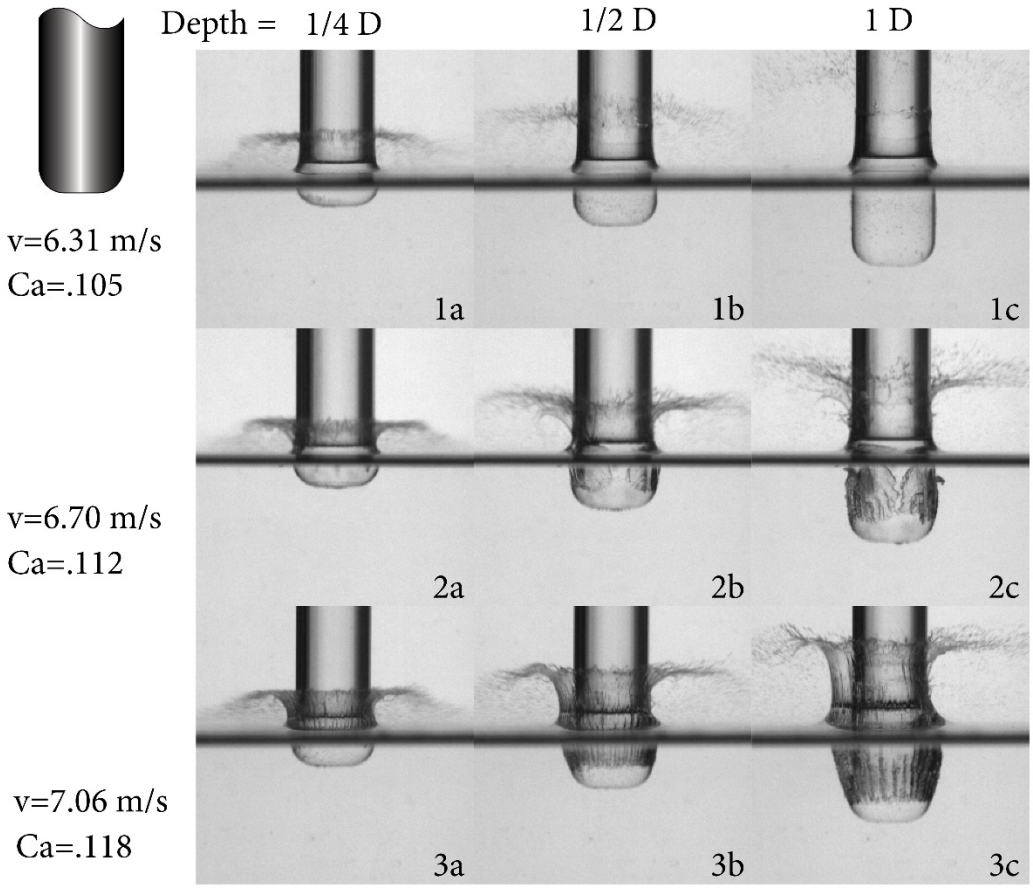

Figure 3-2. Transition region cavity formation for the rounded flat (θ = 72˚). The depth of the projectile through the series is at 1/4, 1/2, and 1 D below the surface, as shown across the top of the figure. Image series 1 shows the entry at a speed just below the threshold region where no cavity is formed. Image series 2 shows the entry at a speed in the transition region. Notice that a partial cavity is formed, where air is entrained at one or more locations but not fully around the circumference. Finally image series 3 shows the entry at the threshold region. Here the air is entrained, and the cavity is formed fully around the circumference.

different wetting angles except at the highest wetting angle (discussed in section 3.1.3). The velocity range of the transition region varies significantly between wetting angles. The velocity range for the uncoated (θ=72˚) and superhydrophobic (θ=163˚) cases are grouped closely (within 1 m/s) while the super-hydrophilic (θ=23˚) and hydrophobic (θ=108˚) cases have a greater spread (up to 2.24 m/s). The difference in ranges can be explained, in part, by the roughness of the

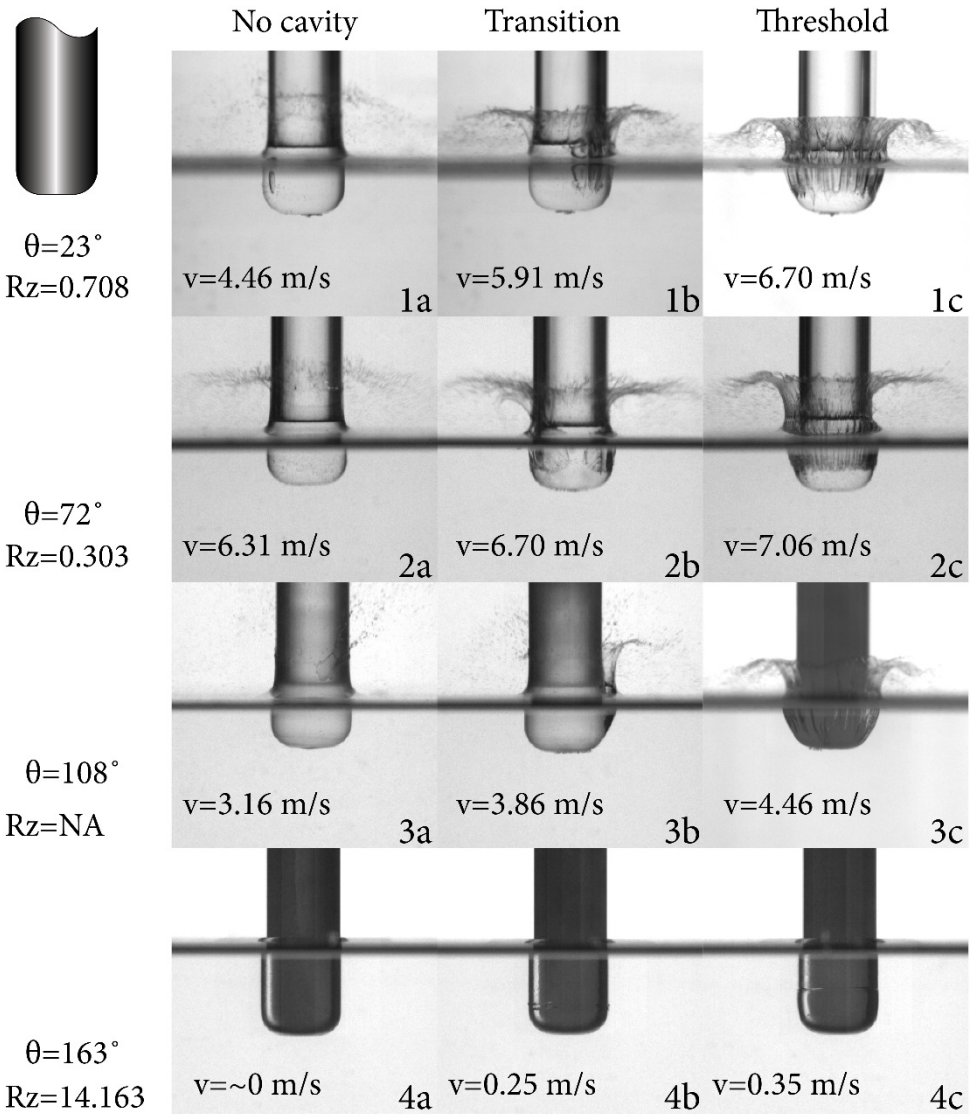

Figure 3-3. Comparison of the transition regions and threshold velocities (v) as a function of wetting angle (θ) and accompanying roughness. Notice that some impact velocity regions (from no cavity to full cavity) are grouped more tightly than others (impact velocity is listed instead of separation velocity for low velocity impacts in this figure).

coating. Cavity formation is sensitive to roughness and surface imperfections in the transition region. Roughness and surface imperfections cause a contact line to pin in a local area, but not globally, and consequently require a lower velocity to cause a partial cavity to form. Zhao et al. [23] showed that at a certain velocity an arbitrarily roughened patch on a sphere would pin a

contact line while the rest of the sphere would not. The roughness of the super-hydrophilic coating causes it to have a lower and wider transition velocity range, while the range for the polished case is more tightly grouped due to its smooth surface. These effects of roughness will be further explained in the next section.

3.1.2 Effect of roughness on the threshold velocity in the super-hydrophilic range

Wetting and roughness can have a combined effect on the threshold velocity for cavity formation, especially when the roughness is relatively high. This section illustrates why and how the wetting angle was adjusted for the influence of roughness on the hydrophilic coating.

In the current study there was a discrepancy between the results in the hydrophilic region and the trend predicted by Duez et al. [17]. They only considered the effects of wetting angle (and not roughness) on the threshold velocity for cavity formation. The prediction they made, and trend they found, was that all smooth spheres with a wetting angle less than 90˚ had the same threshold velocity, and as the wetting angle increased above 90˚, the threshold velocity exponentially decreased. In the current study two wetting angle regions were tested in the hydrophilic region of the chart, one in the $60^\circ < \theta < 90^\circ$ region and one in the $0^\circ < \theta < 40^\circ$ region. Contrary to the constant transition velocity predicted by Duez for the entire hydrophilic region, the transition velocities for our projectiles in the lower hydrophilic region ($0^\circ < \theta < 40^\circ$) are significantly lower than the transition velocities for the projectiles in the higher region ($60^\circ < \theta < 90^\circ$), see Figure 3-4. Zhao et al. [23] also found transition velocities significantly lower than predicted in the hydrophilic region in their study with roughened spheres. They found that the lower transition velocities were connected to projectiles with a high surface roughness and that surface roughness had a significant effect on the transition velocity. Similar observations were made by Worthington [21] who noted that a higher threshold velocity could be obtained by

carefully polishing the sphere. Similarly, the low transition velocities in the hydrophilic region are explained by the roughness of the hydrophilic coating. This additional roughness causes the projectile to entrain air at a much lower velocity than the carefully polished projectiles in the upper hydrophilic region.

Zhao et al. [23] demonstrated how the roughness induced lower transition velocities by recalculating the wetting angle of the projectiles in the Cassie-Baxter regime (determined by the Cassie-Baxter equation). These revised wetting angles placed the threshold velocities in good agreement with Duez's prediction. Figure 3-4 shows the effect of recalculating the wetting

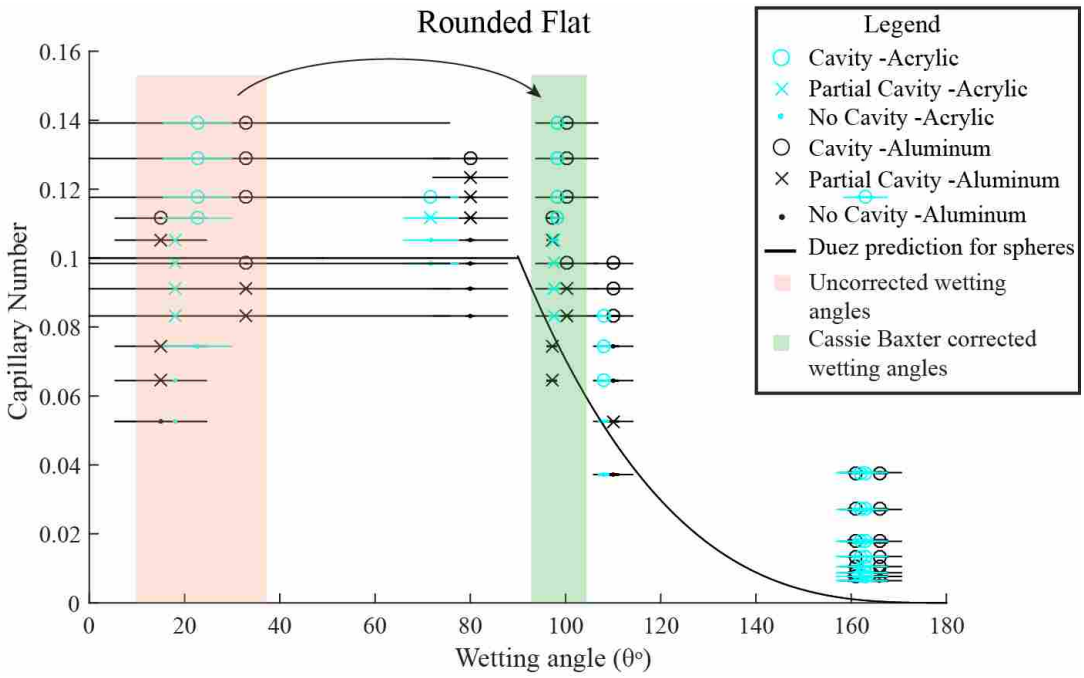

Figure 3-4. Example of correcting the wetting angle values in the Cassie-Baxter regime. The red area shows the measured advancing contact angles. The green area shows where the wetting angles from the red area fall within the data after being corrected for the Cassie-Baxter regime. Note that only the cavity and partial cavity data is within the Cassie-Baxter regime. The horizontal lines are uncertainty bars for the wetting angle.

angles for the lower hydrophilic region in the Cassie Baxter regime using a method with rougher approximations but similar to that used by Zhao et al. [23]. We note that wetting angle is a complicated measure and do not attempt to predict the Cassie-Baxter wetting angle with perfect accuracy but present an approximation to give insight to the deviant cavity behavior seen in the current study for the relatively rough hydrophilic projectiles.

As the impact velocity increases the interaction between the flow and the surface transitions from a Wenzel to a Cassie-Baxter state [23]. The equations for calculating the Wenzel (θ_W) and Cassie Baxter (θ_{CB}) wetting angles, as given by Banerjee [9] are

$$\cos\theta_W = r\ \cos\theta_y, \tag{3-1}$$

$$\theta_{CB} = \cos^{-1}\big(r\, f_s\ \cos\theta_y\ +\ f_s - 1\big). \tag{3-2}$$

Substituting equation 3-1 into equation 3-2 yields the Cassie-Baxter wetting angle as a function of the Wenzel wetting angle, θ_W,

$$\theta_{CB} = \cos^{-1}(\ f_s \cos\theta_W\ +\ f_s - 1). \tag{3-3}$$

Where θ_W is the Wenzel contact angle, and f_s is the fraction of solid tops respectively given as the measured contact angle for the samples and the material ratio at the roughness reference line (see Table 2-3). The fraction of solid tops was calculated using the material ratio at the roughness profile reference line, which was roughly assumed to be the level of the ideal smooth surface.

Recalculating the wetting angle in the Cassie Baxter regime moves the wetting angle from the lower hydrophilic region to the slightly hydrophobic region and better fits the transition and threshold velocities of the projectiles to the trend seen by Duez et al. [17], see Figure 3-4. The

uncertainty for the calculated Cassie-Baxter wetting angle is given in Appendix A. The study thus shows, as did Zhao et al.'s [23] that the threshold velocity for a given shape in the hydrophilic region is not dependent on measured wetting angle alone, but also on its roughness.

3.1.3 Cavity formation in the superhydrophobic range

In the superhydrophobic range the velocity at which cavities form is very low and the cavity formed is barely visible. The wetting on the projectile appears to be in the Cassie-Baxter regime where the flow skips from peak to peak on the surface and a thin film of air is trapped despite the low impact velocity. The thin film of air is evidenced by the smooth, reflective surface of the projectile, see Figure 3-5.

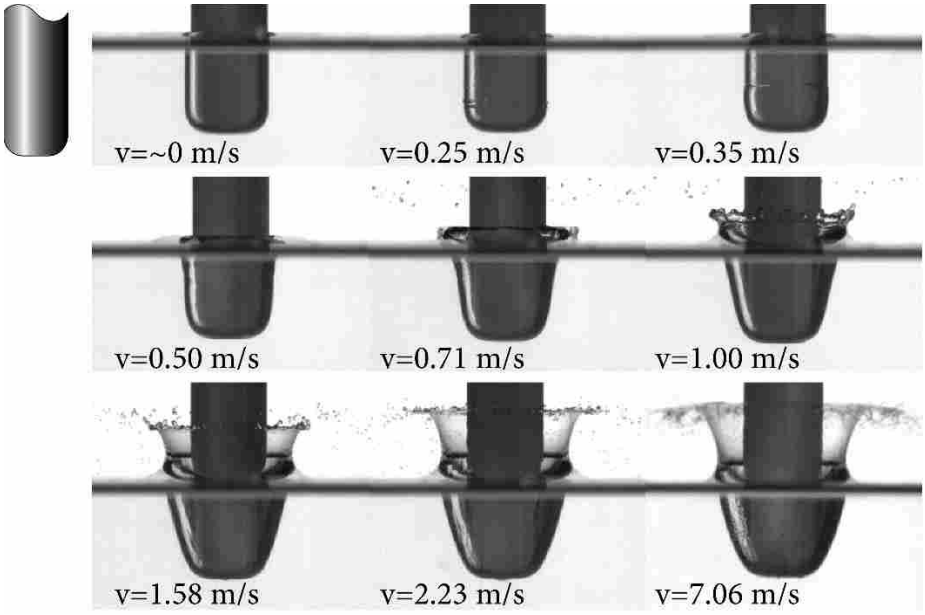

Figure 3-5. Shape of the cavity formed by the rounded flat shape as a function of speed in the superhydrophobic region. Each image is taken at 1 D below the water surface. Notice that a cavity is formed at very low speeds but is almost imperceptible, then grows as the impact velocity increases (impact velocity is listed instead of separation velocity for low velocity impacts in this figure)

A cavity was considered formed when a visible pinch off was seen at some point in the entry. This gave evidence that not just a thin film was trapped but that the flow separated enough to grow the cavity momentarily and then pinch off. Figure 3-5 shows the evolution of the cavity formed by the rounded flat shape in the superhydrophobic range through a range of impact velocities, ~0 < v < 7m/s.

3.1.4 Effect of shape on the threshold velocity through varying surface conditions

Thus far we have seen that factors such as wetting angle and roughness can alter the velocity at which a particular projectile will entrain air and eventually form a cavity. We now look at the effect that shape has on the threshold velocity. A range of drop heights was tested for each shape and surface condition to determine the velocities at which cavities would and would not form. The drop test results detail the Capillary number where partial and full cavities formed for each shape, except where data could not be obtained, see Figure 3-6, Figure 3-7, and Figure 3-8. For reference the results are plotted with the theoretical prediction of the threshold velocity for spheres as proposed by Duez et al. [17], which is given as

$$U^* = \frac{g_o}{9\zeta\ell}\frac{\gamma_{LV}}{\mu_L}[\pi - \theta_o]^3, (\theta \geq 90°), \tag{3-4}$$

$$U^* = \xi\frac{\gamma_{LV}}{\mu_L}, (\theta \leq 90°), \tag{3-5}$$

where they assumed g_o=7, ζ=2, ℓ=15, γ_{LV} is the liquid-vapor surface tension between water and air, and μ_L is the liquid viscosity. A similar prediction was made for the threshold capillary number for each of the shapes based on the equation given by Duez et al. [17], but with modified

values to fit the available data. If we rearrange equations 3-4, and 3-5 to determine the threshold capillary number they become

$$\frac{\mu_L U^*}{\gamma_{LV}} = \frac{g_o}{9\zeta\ell}[\pi - \theta_o]^3 = Ca^*, \tag{3-6}$$

$$\frac{\mu_L U^*}{\gamma_{LV}} = \xi. \tag{3-7}$$

The predictions are given mainly for comparison purposes between the shapes. Of the three shapes tested, the rounded flat shape had the lowest transition and threshold velocities across all wetting angles, yet still maintains a higher threshold velocity than the sphere. The cone and ogive shapes had a much more pronounced effect on increasing the threshold velocity, doubling the threshold or more for some wetting angles, when compared to the sphere.

The driving difference between the nose shapes is the local acceleration of the water over the projectile surface. The effects of the different nose geometries on the local acceleration are quantitatively compared by several parameters including tip bluntness, nose length, and shaft abruptness. The tip bluntness is determined by measuring the diameter of the nose at 1/10th D from the tip of the projectile and dividing it by 1/10th the shaft diameter. This gives insight into the degree to which the projectile has a blunt or pointed nose. The nose length is a measure of how sharp the entire nose is. It is based on the assumption that the profile of the nose is smooth and the curvature is gradual. The nose length is determined by dividing the length of the nose region by the diameter of the shaft. It gives insight into the relative length over which the flow transitions from the tip to the shaft of the projectile. The shaft abruptness is a measure of how smoothly the root of the nose section transitions to the shaft. It is determined by measuring the difference between the shaft diameter and the diameter at the last 1/10th of the nose region,

divided by 1/10th of the diameter. It gives insight into the abruptness of the transition from the nose region to the shaft. These values for the shapes used in the study as well as the sphere are listed in Table 3-1.

Table 3-1. Values of tip bluntness (how sharp the nose tip is), nose length (how sharp the overall nose region is), and shaft abruptness (how suddenly the nose root transitions to the shaft) for each shape. Green indicates that the parameter will contribute to a higher threshold velocity than the sphere, while Red indicates it will contribute to a lower threshold velocity.*The shaft abruptness for the sphere does not apply in the same way as the other shapes because the initial nose region is not followed by a cylindrical shaft but by a negative region.

Shape	Tip Bluntness (D of nose at 1/10th D from tip/ 1/10 D)	Nose length (Nose length/ D)	Shaft abruptness (D remaining at last 1/10th D of nose length/ 1/10 D)
Rounded Flat	8.48	0.3	0.34
Ogive	4.36	1	0.06
Cone	1.20	2	0.40
Sphere	6.00	0.5	0.10*

The rounded flat shape has a high tip bluntness, a short nose length, and a medium shaft abruptness. These combined factors cause the rounded flat to induce a high local acceleration as the liquid flow is rapidly displaced across the initial flat region and then around the rounded corners. The flow moves rapidly as compared to the other shapes because of the large tip bluntness and the relatively short nose length. Each of the parameters are higher for the rounded flat than the sphere, and yet it has a higher transition velocity, see Figure 3-6. The difference in shaft abruptness is a little misleading for the sphere because the sphere does not have a shaft that follows after the nose region. The lack of the shaft region creates the most pronounced difference between the sphere and the rounded flat shape and is discussed in greater detail in section 3.1.4.1.

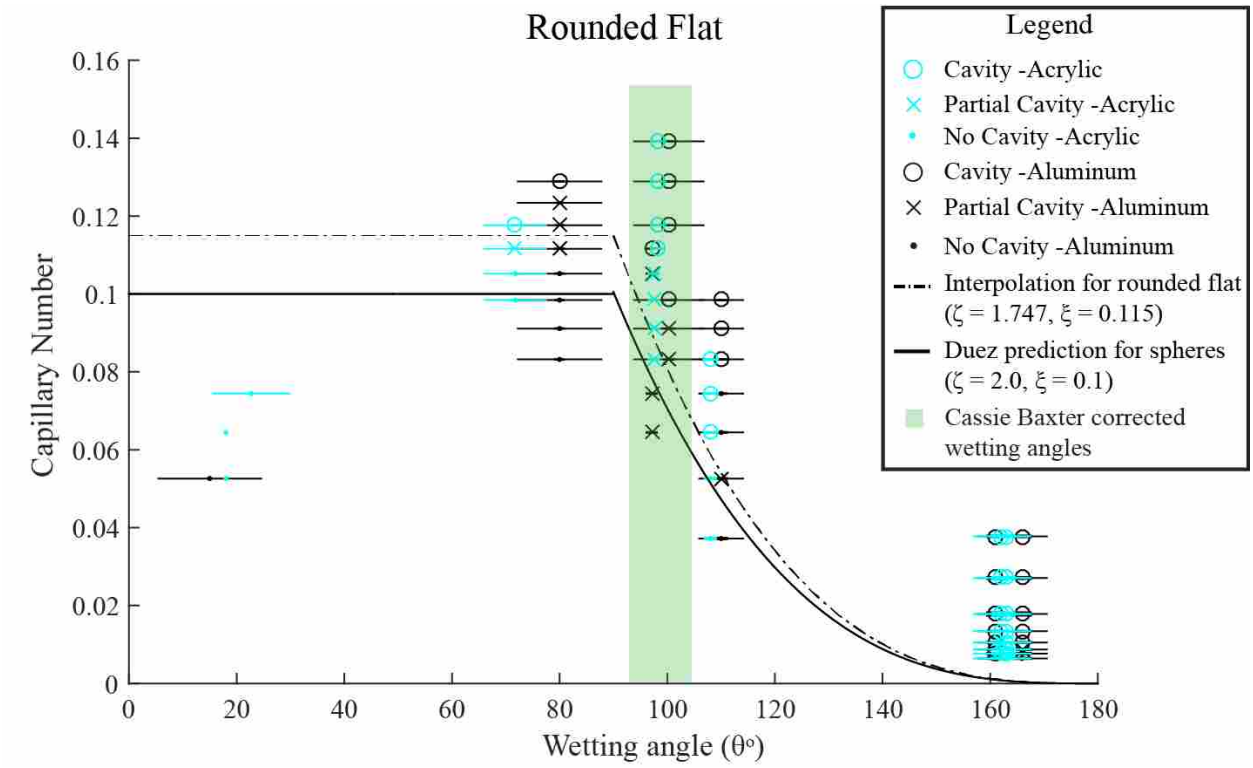

Figure 3-6. Cavity data for the rounded flat shape. The results are close to the theoretical prediction for the sphere, yet higher because of the shaft following the rounded flat shape. The green section shows the wetting angles recalculated in the Cassie-Baxter regime. The dashed line is a rough prediction for the threshold velocity based on the equation given by Duez et al. and modified to fit the available data.

The ogive shape sits in the middle of the parameter values having a mediocre tip bluntness and nose length, but also has a near 0 shaft abruptness. These parameters indicate that the ogive would have a gentler impact on the fluid than the rounded flat shape. Also the near zero shaft abruptness indicates that there is no set point at which the flow will separate before the shaft. This serves to delay cavity formation until the flow has sufficient speed to separate at a lower point on the nose region. When compared to the sphere the ogive has about 2/3 the tip bluntness of the sphere and twice the nose length. These differences contribute to giving the ogive shape a much higher transition velocity than the sphere, see Figure 3-7.

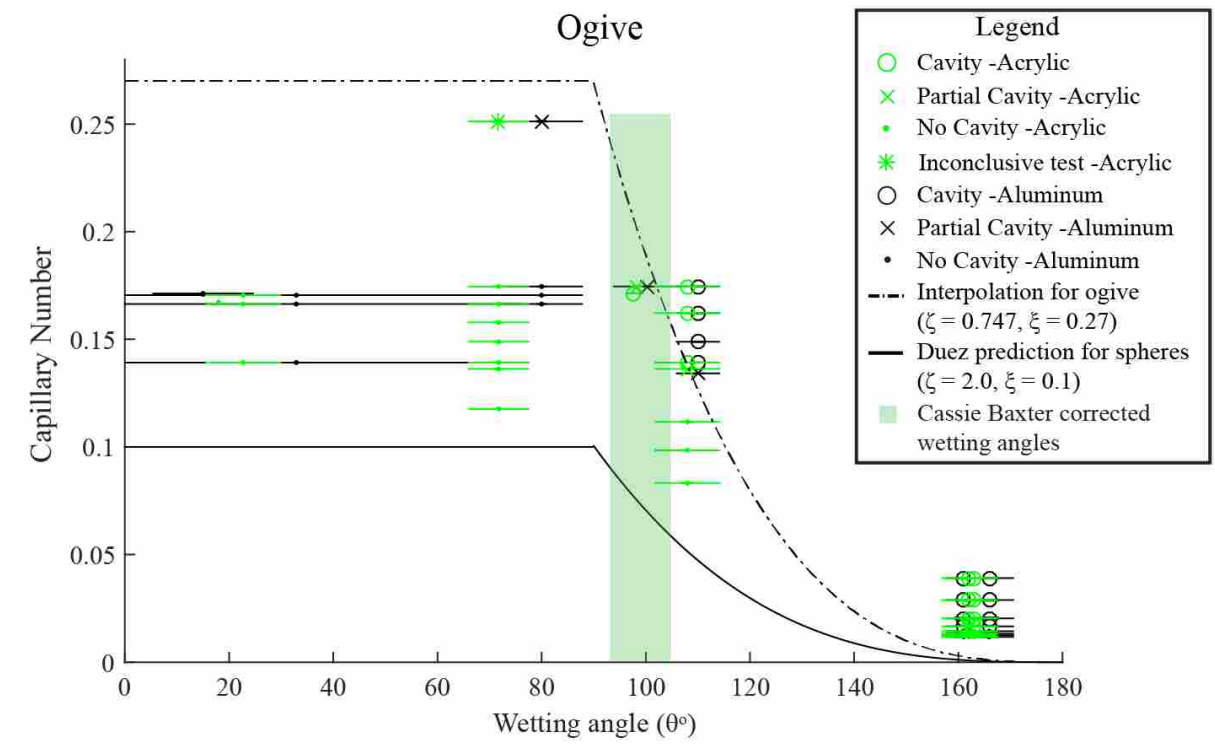

Figure 3-7. Cavity data for the ogive shape. The green section contains the Cassie-Baxter corrected wetting angles. Note that the dashed line is a rough prediction for the threshold velocity based on the equation given by Duez et al. and modified to fit the available data.

The cone shape seems to have a threshold velocity similar to the ogive shape, at least from the limited data collected, but there are some important differences. The ogive shape has a gradual and continually changing nose region so that there are no sharp corners or transitions as indicated by a low shaft abruptness. The cone, however, has the highest shaft abruptness because of the clear transition between the nose and shaft region. The cone's low tip bluntness and long nose region seem to make up for the relatively high shaft abruptness and produce similar results with the ogive in terms of the threshold velocity as seen in comparing Figure 3-7 and Figure 3-8. In comparing the cone with the sphere, the cone has 1/5 the tip bluntness as well as 4 times the nose length, contributing to a much higher threshold velocity.

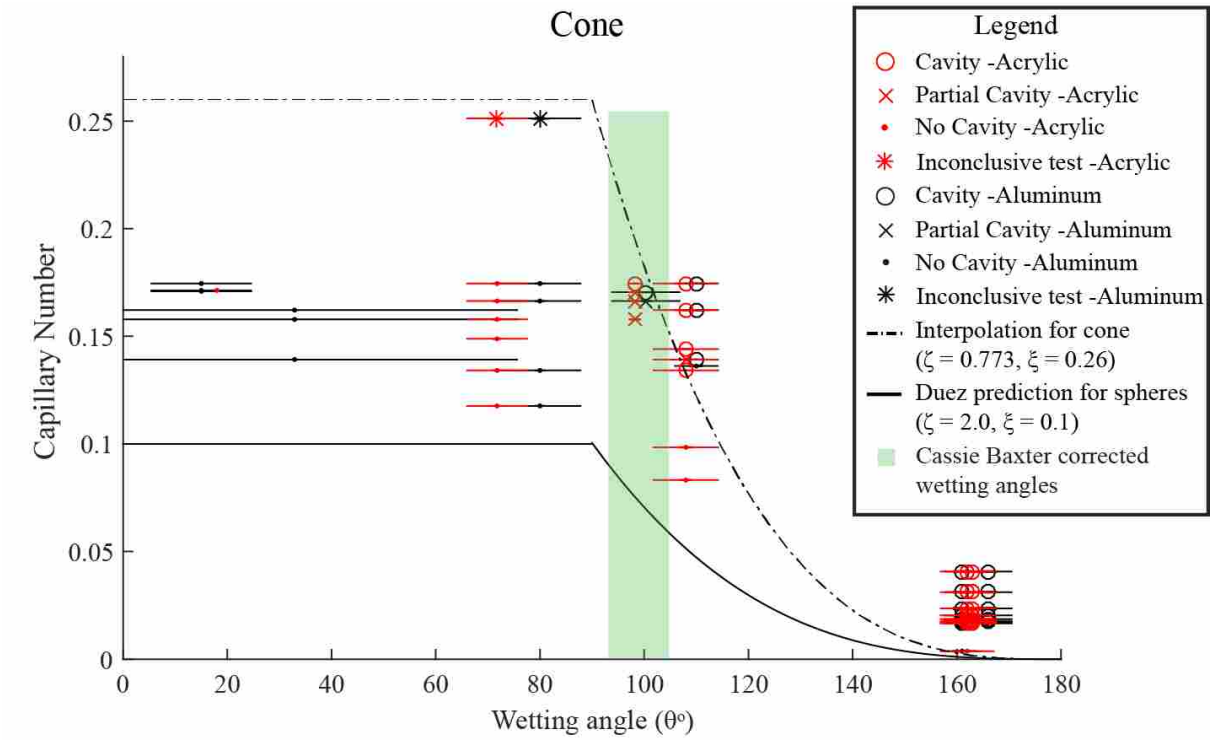

Figure 3-8. Cavity data for the cone shape. Note that the dashed line is a rough prediction for the threshold velocity based on the equation given by Duez et al. and modified to fit the available data.

3.1.4.1 Sphere comparison

An important difference between the axisymmetric projectiles (nose shape followed by a cylindrical shaft) and the sphere and other projectiles is the lack of negative space immediately following the nose region. Figure 3-9 compares the entry of spheres and the ogive nose shape. Spheres will first form cavities by pinning a contact line near the midline. The negative region above the midline facilitates cavity formation. Ding et al. [24] analytically and experimentally showed that the upper hemisphere (above the sphere midline in the negative region) is more

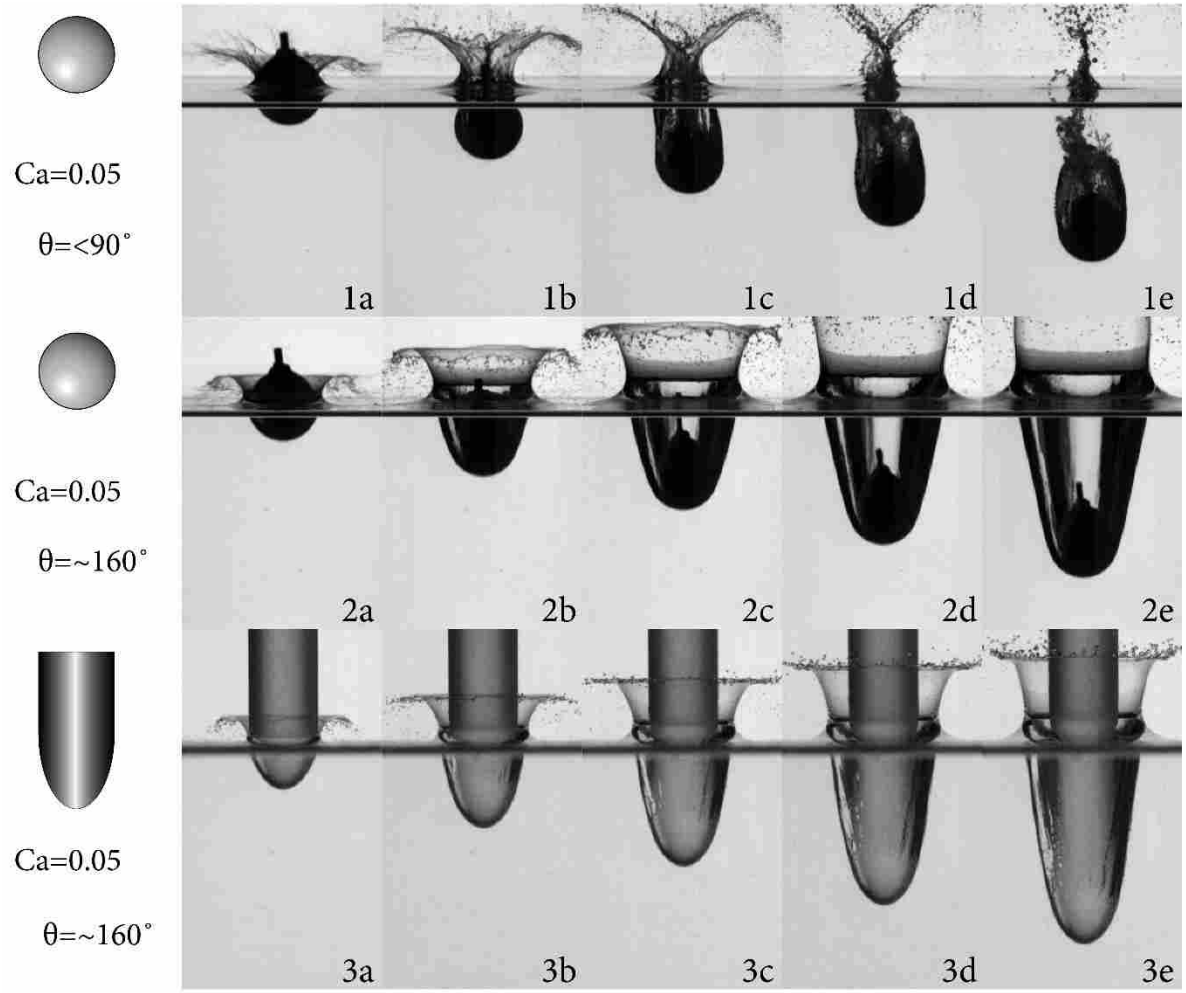

Figure 3-9. Comparison of the entry of a sphere (hydrophilic and hydrophobic) and the ogive shape (hydrophobic). Notice that in image 1b the flow has adhered to the sphere surface into the negative region beyond the midpoint (1/2 D) and yet in images 1 c-e still has managed to pin a contact line. This shows the influence of the negative region following the initial nose of the sphere in pinning a contact line. Comparing image series 1 and 2, both spheres pin contact lines at the same Ca number although the wetting angles and consequently the point at which the flow separates is different. In image series 1 the flow separates behind the midline and in image series 2 the flow separates before the midline.

favorable for the pinned contact line to rest on than the lower hemisphere. The shapes used in this study meet up with the shaft at their maximum radius and do not have a negative region following the nose shape. This forces the shapes to have a higher impact velocity in order to pin a contact line at or below the maximum radius, than is required for a sphere to pin a contact line

above the maximum radius. Consequently projectiles that are followed by a cylindrical shaft after the nose region will require a higher impact velocity to form a cavity than an equivalent nose shape that does not.

3.1.5 Upper bound of obtainable impact velocities

The threshold velocities for the uncoated cone and ogive shapes were not found because they required higher impact speeds than could be obtained with the current set up. The largest factor in preventing useful data at higher impact speeds was the imbalance between the center of pressure from the drag and the center of mass of the projectile. The projectiles were made from a solid shaft of material which placed the center of mass near the middle of the projectile. In our vertical drops the center of pressure acted on the nose of the projectile, below the center of mass. This created a tipping moment, akin to vertically balancing a broom on the end of the handle. At high enough drop heights, the pressure acting on the projectile caused it to tip at the slightest disturbance, whether from a slight draft in the room or a slight misalignment or vibration in the test setup. Once the projectile was tipped away from the vertical it would enter the water at an angle and produce misleading results.

3.2 The effect of concave shape on cavity formation

A concave shape is one that curves inward and forms a pocket or cave-like void. Many studies have focused on the cavity formation by various convex shapes [1] [1] [15] [24] [8], for example, but relatively few have focused on the cavity formation by concave shapes [1] [27]. Concave shapes used in the current study are shown in Figure 2-3.

Concave shapes create a unique cavity shape when entering the water. Figure 3-10 compares the cavity formed by a concave shape (image a) with that of two convex shapes

(images b, c). The cavity formed by the concave projectile is small and has a different shape when compared to the convex projectiles.

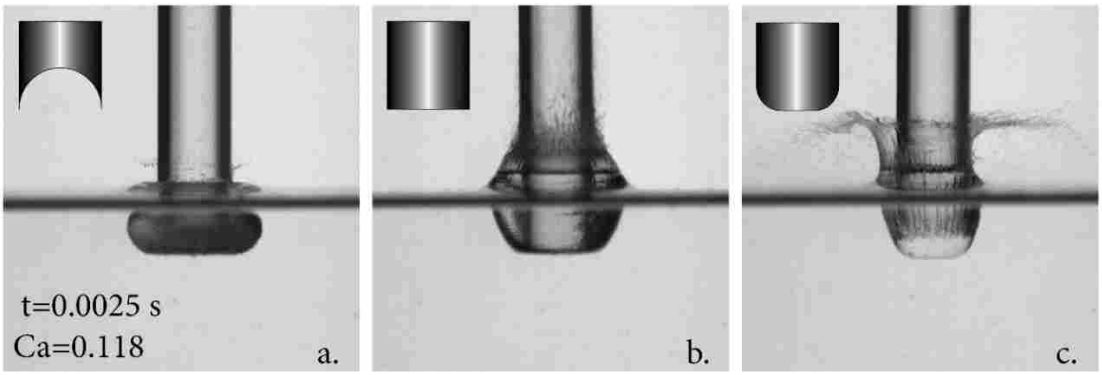

Figure 3-10. Comparison of the ring-like cavity formed by a concave shape to the classic cavity formed by convex shapes at the same capillary number and time (t) after impact. Insets: a. concave hemisphere (ball), b. flat, c. rounded flat. Projectile nose geometry shown in upper left-hand corner.

3.2.1 Methods of air entrainment

There are several different means by which projectiles entrain air or form cavities, which are affected by their geometry. The main cavity types include what we call a classic cavity (pinning a contact line), air trapping, and ring cavities (those formed by concave bodies). The terms *classic cavity* and *ring cavity* were coined to distinguish between the types of cavities formed in this study.

3.2.1.1 Classic cavity

A *classic cavity* is the type of cavity made by a convex shape when it pins a contact line and entrains air, forming an air pocket in the surface of the water, see Figure 3-10 b and c. This cavity grows vertically as the projectile descends and grows radially by the momentum of the

displaced water. This cavity is eventually sealed off from the ambient air by the collapse and pinch off of the underwater cavity (shallow or deep seal) or by the splash curtain collapsing on itself or the walls of the projectile (surface seal).

3.2.1.2 Air trapping

Air trapping is most pronounced in the entry of blunt projectiles, which was studied in depth by Hicks et al. [30]. They showed that just before impact the air in between the projectile and water surface is displaced downward from the pressure rise (greatest along the central axis), and deforms the water surface. The bowed surface of the water causes the edges of the projectile (or some distance away from the center) to impact the water before the center and trap the air in the middle. Only a small portion of air is trapped this way and quickly coalesces into a bubble at the bottom of the projectile, see Hicks et al. [30] Figures 2 and 4. The result of this can be seen in Figure 3-21, images 3a-3c.

3.2.1.3 Ring cavity

A *ring cavity* is formed in the wake of a concave shape entering the water with sufficient speed. This cavity forms and grows almost entirely from the trapped pocket of air, and not by pinning a contact line. The mechanism is different from a classic cavity, but similar to air trapping. At different speeds a pinned contact line may be more or less prevalent in the entry but in and of itself is not the driving force to form the ring cavity. The ring cavity is characterized by a ring of air pinned to the leading edge of the projectile and filled mostly with air from the concavity. The key events in a ring cavity formation are shown in Figure 3-11. At impact (image a), the air in the concave nose is cut off from the surrounding ambient air and forced below the

surface of the water. Insets a_2 and b_2 show that the water is in contact with the projectile and that a contact line has not been pinned. As the projectile descends (image b) the water intrudes into

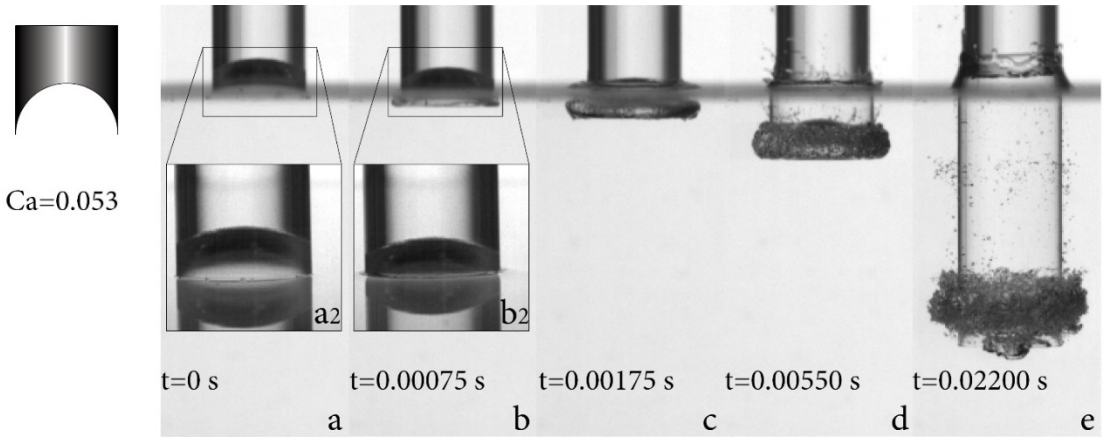

Figure 3-11. Formation of the ring cavity. Ca= 0.053, v=3.16 m/s. At impact the air in the concave shape is trapped by the water surface, image a. Notice in insets a_2 and b_2 (above surface shots of the entry) that a contact line is not pinned. As the projectile descends the water compresses the trapped air (image b) which is eventually forced out of the concave shape around the leading edge (image c) and forms a ring cavity (images b-d). As the projectile descends further the ring cavity separates from the leading edge and dissipates (image e). Note that the ring shape is maintained by a vortex circulation, see Figure 3-14.

the concave nose, raising the pressure of the air and forcing the air to vent out around the edges of the concave nose in the form of a ring cavity (image c). The ring cavity continues to grow until the pressure equalizes and the remaining air is forced back to the top of the concave nose (image d). Eventually the ring cavity will separate from the leading edge of the projectile and disperse as the projectile continues to descend (image e). At high enough impact speeds a strong vorticity develops soon after impact that maintains the cavity's ring-like shape, as shown in the PIV results in Figure 3-14.

To illustrate the importance of the trapped pocket of air on the formation of the ring cavity two concave hemisphere shapes were used. One projectile having 8 holes (each 1.6 mm

diameter) drilled through the body at an angle to top of the concave nose to allow the air to escape and not be trapped below the water surface. The entry of the two projectiles is compared in Figure 3-12. A distinct cavity is formed by the unaltered concave shape while no cavity is formed by the vented concave shape. This clearly illustrates the need for a trapped pocket of air to form the ring cavity. The test was performed at a speed low enough to allow the air to completely vent from the concave cavity. Higher speeds were investigated but the ventilation was not sufficient to prevent air entrapment.

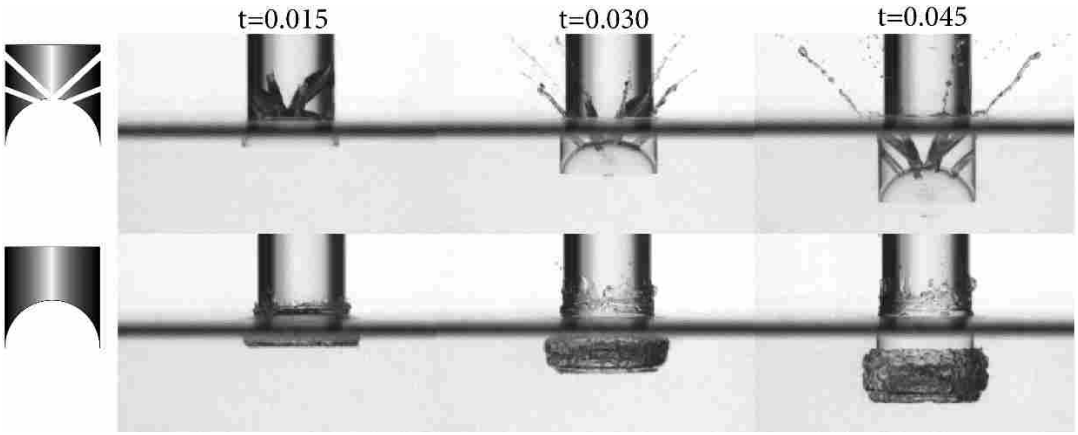

Figure 3-12. Entry of two concave ball shapes (cross sections shown on the left), Ca =0.026, v=1.58 m/s. The top series is of a concave ball shape with 8 shafts (each 1.6 mm diameter) to vent the air from the cavity, while the bottom series shows an unaltered concave ball. The air completely vents through the shafts as the projectile descends into the water making the only difference between the two in the first portion of their entry the trapped pocket of air. This illustrates the necessity of the trapped pocket of air for the concave shape to form a ring cavity.

Aspects of the ring cavity were further investigated through PIV analysis. Velocity magnitude and vorticity results of two concave shapes compared with the three convex shapes, studied in section 3.1, are shown in Figures 3-13 and 3-14 and shed some light on the effects of the different shapes on the flow of the water upon cavity formation. The two concave shapes cause an initial high velocity flow which then travels to the side and circulates around the nose

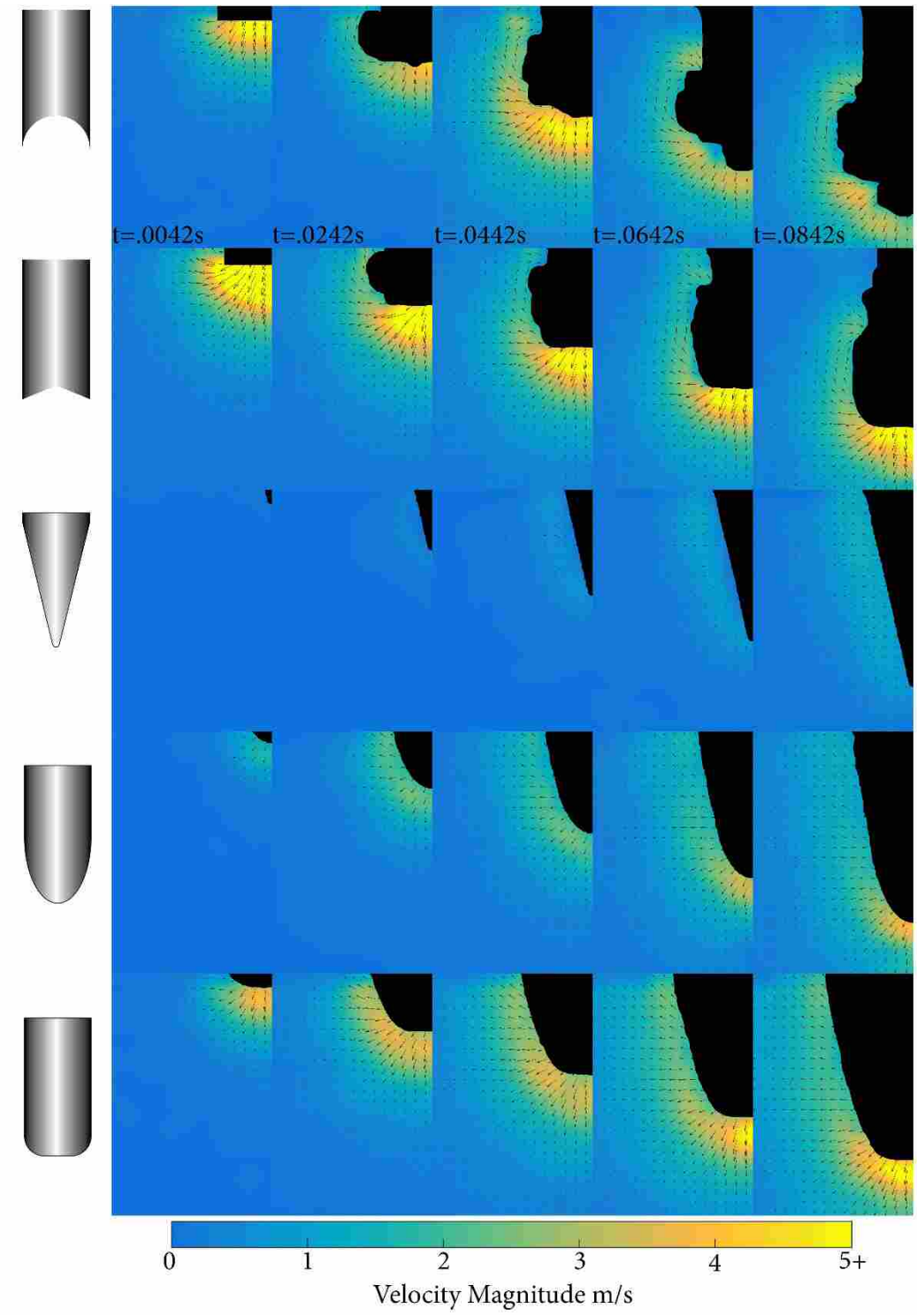

Figure 3-13. Velocity magnitude plots from PIV analysis. Ca=0.118, v= 7.06 m/s. The concave shapes cause a much faster flow at impact and subsequent cavity formation than the convex shapes do. The convex shapes were coated with a superhydrophobic coating to ensure cavity formation at this entry speed for comparison with the concave shapes. Progression of the impact through time is seen from left to right. The shape of the projectile is at the left of each row.

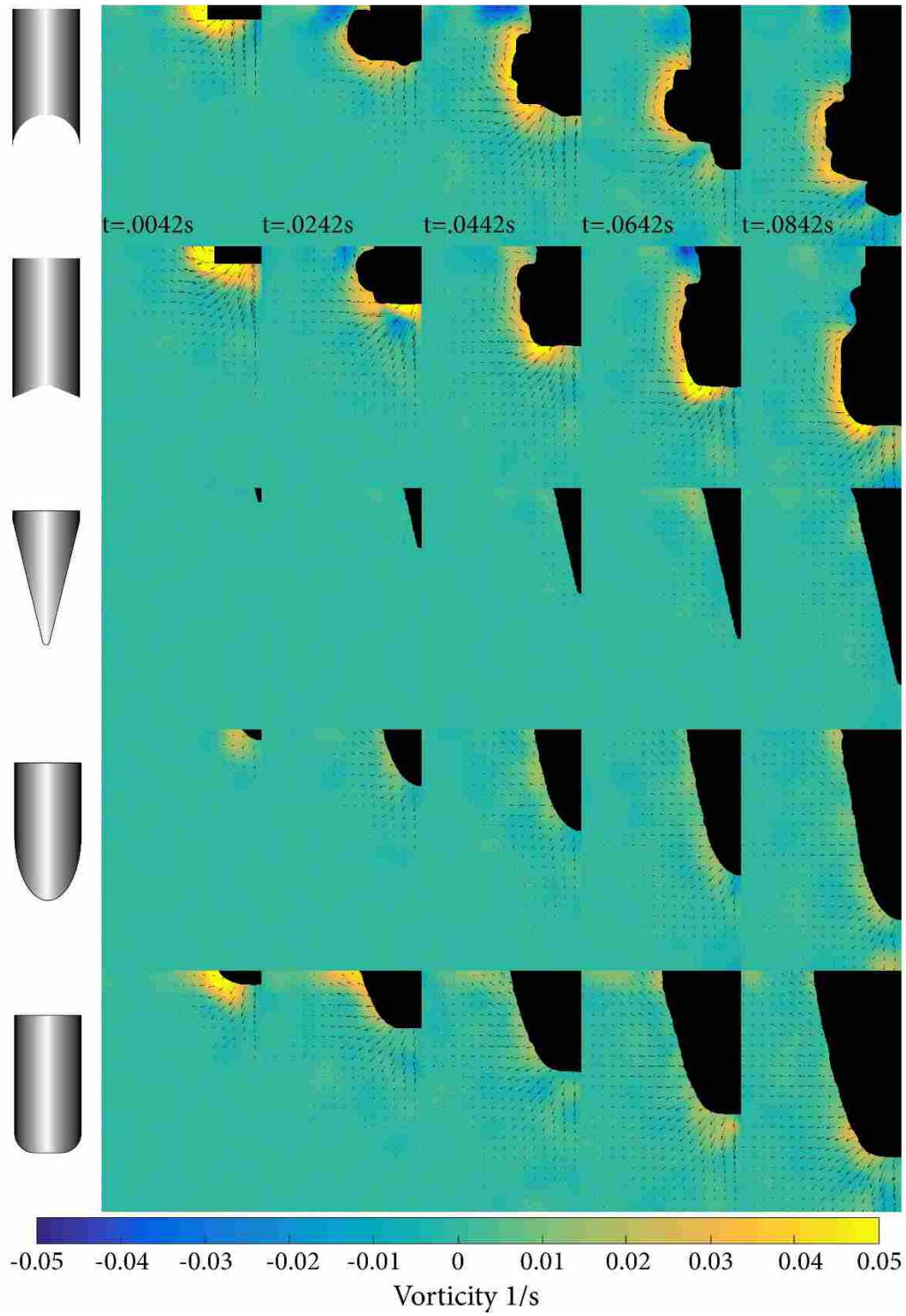

Figure 3-14. Vorticity plots from PIV analysis. Ca=0.118, v= 7.06 m/s. The concave shapes induce a high vorticity in the flow immediately around the nose of the projectile while the convex shapes do not. The rounded flat shape does induce a small vorticity at impact, but does not grow and persist as with the concave shapes. The time for each image is listed at the top of the column.

region in a vortex ring before dissipating. The three convex shapes impart a much lower initial velocity to the water. The flow spreads radially for the most part and does not circulate around the nose and induce vorticity as seen with the concave shapes. The rounded flat shape does induce a small vorticity at impact but the vorticity quickly dissipates and does not persist and develop into a vortex ring as with the concave cases.

3.2.2 Effects of velocity on the cavity formed by the concave nose shape

Mathai et al. [27] studied the entry of a concave hemisphere at two impact speeds, (7 & 10 m/s). No study though has investigated the impact of concave nose shapes at low velocities. The present study focuses on the entry of several concave geometries over a range of impact speeds (~0-10 m/s). In general, the behavior of the different concave shapes varies significantly throughout this larger range of impact speeds, indicating a need to understand their behavior at these lower impact speeds.

The progression of the cavity shape for the concave ball through the range of speeds tested is shown in Figure 3-15 and Figure 3-16 at 1/2 and 1 Diameter (D) below the surface. There appears to be three main regions of impact velocity where cavities are similar. These regions are grouped into low, moderate and high impact velocities. At low velocities (0 m/s < v ≤ 1 m/s) the cavity wall is clear and smooth, and formed by contact line pinning with little to no vorticity or other disturbances, see Figure 3-15 and Figure 3-16 images a-f. At moderate speeds (1 m/s < v < 4 m/s) the cavity wall is rough and the cavity size small, showing the cavity was formed by underwater venting, see Figure 3-15 and Figure 3-16 images g-j. At high speeds (5 m/s < v < 10 m/s) the cavity wall is smooth yet disturbed, as a result of contact line pinning, and rapid underwater venting.

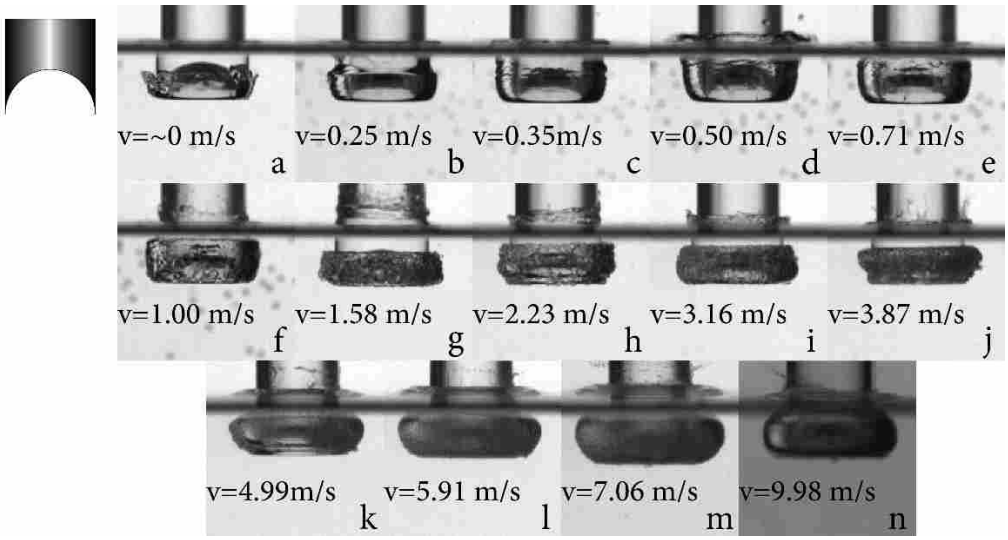

Figure 3-15. Cavity shape as a function of speed for the concave ball nose shape. Images are taken at approximately 1/2 diameter (D) below the surface. Notice there are three regions where the cavity shapes are similar, images a-f are the first or low speed region ($0<v\leq1$ m/s), images g-j are the second or moderate speed region ($1<v<4$ m/s), and k-n are the third or high speed region ($4<v<10$ m/s).

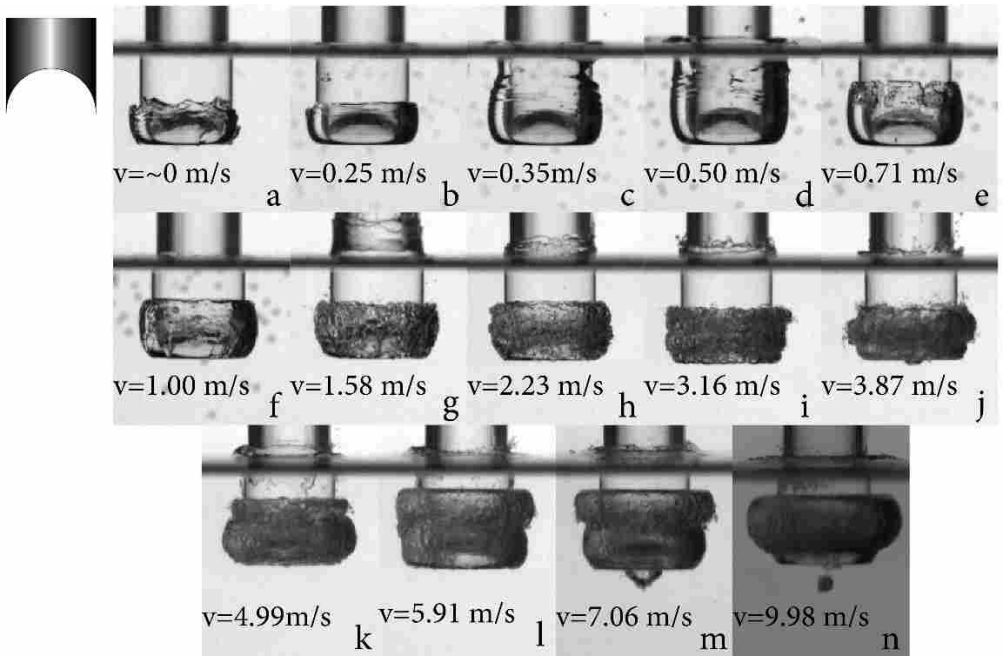

Figure 3-16. Cavity shape as a function of speed for the concave ball nose shape. Images are taken at approximately 1 D below the surface and come from the same drop tests as Figure 3-15. Comparing Figures 3-15 and 3-16, the three regions show similar cavity shape at both depths.

A time series of images from drops at the median velocity in each of these regions was selected to show their respective cavity progression, see Figure 3-17. Image series 1 shows the

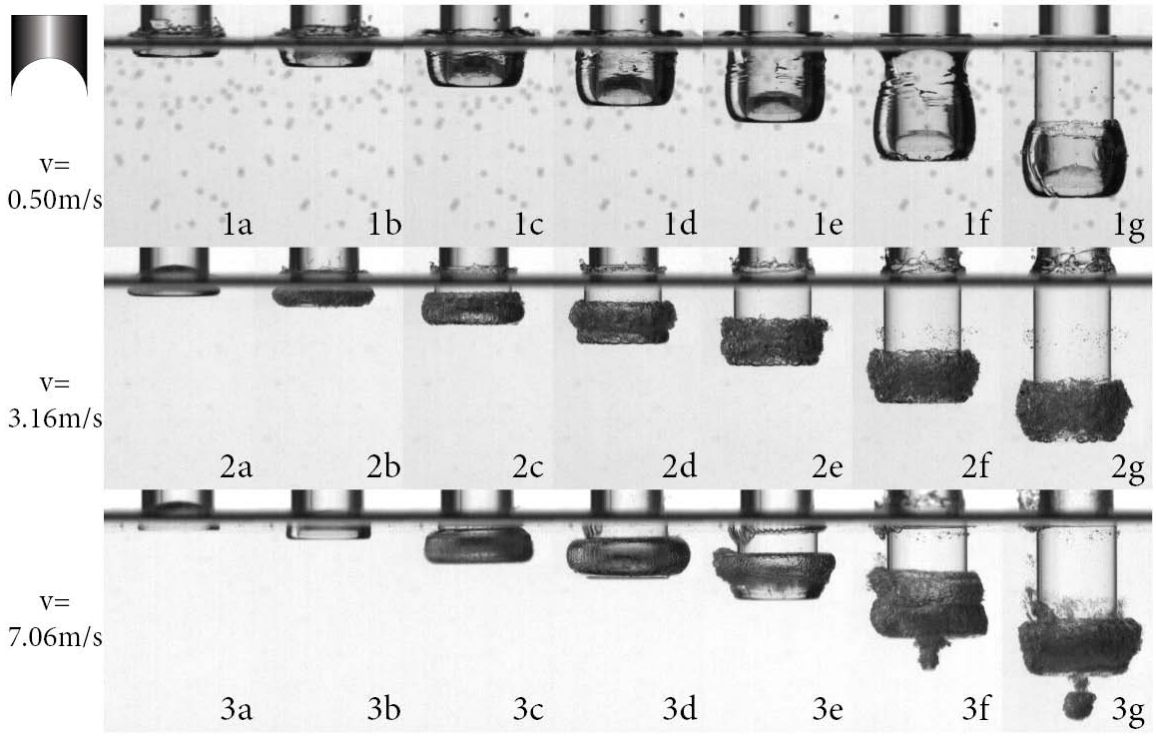

Figure 3-17. Progression of the three cavity types for the concave ball shape. The projectile depths for the image series are as follows: a. 1/8 D, b. ¼ D, c. ½ D, d. ¾ D, e. 1 D, f. 3/2 D, g. 2D. Image series 1 shows the progression of the cavity at a velocity in the middle of the first region (v=0.5 m/s) and is similar to a classic cavity progression. Image series two shows the cavity progression in the second region at v=3.16 m/s. In this region a ring cavity forms, which is filled with the air initially trapped in the concave ball (image 2b-c). Image series 3 shows the cavity progression in the third region, at v=7.06 m/s, where a small contact line is initially pinned and quickly pinches off on the body (images 3a-b). The cavity then rapidly fills with the air trapped in the concave ball (image 3c) and forms an unsteady pressure flow.

progression of the cavity at a velocity in the middle of the first region (v=0.5 m/s) and is similar to a classic cavity progression. Image series 2 shows the cavity progression in the second region at v=3.16 m/s. In this region a ring cavity forms, and fills only with the air initially trapped in the concave ball (image 2b-c). The venting of the air from the concave shape into the small classic

cavity causes a rough cavity to form that circulates around the nose section until it separates from the leading edge of the projectile. Image series 3 shows the cavity progression in the third region at v=7.06 m/s, wherein a ring cavity is also formed. Similarly, a small contact line is initially pinned and quickly pinches off on the body (images 3a-b). However, the cavity rapidly fills with the air trapped in the concave ball (image 3c) and forms an unsteady pressure flow, which will be explained in a later section.

The concave cone behaves nearly identical to the concave ball having the same velocity regions and cavity behavior, with the exception of the cavity size at low and mid velocities. In the low region the maximum cavity size for the concave cone is seen in Figures 3-18 and 3-19

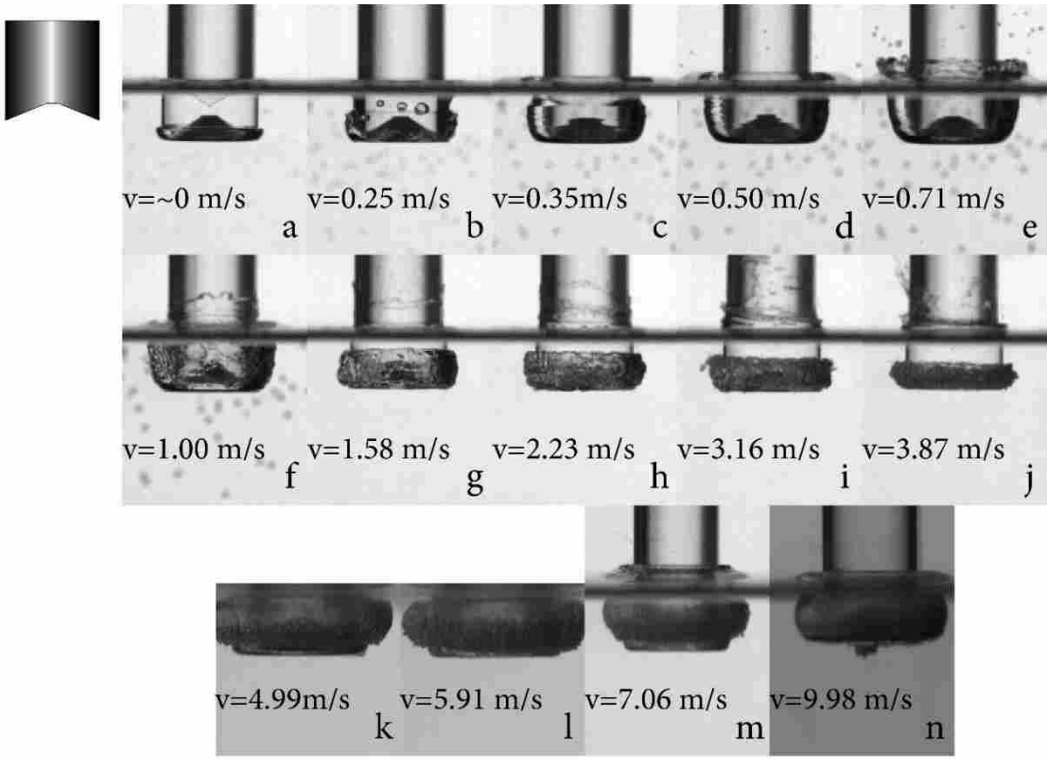

Figure 3-18. Three main cavity shapes for concave cone, grouped as follows: images a-f are the first or low speed region (0<v≤1 m/s), images g-j are the second or moderate speed region (1<v<4 m/s), and k-n are the third or high speed region (4<v<10 m/s). The regions are similar to the concave ball. Projectiles are each shown at ½ D below the surface.

image e at a velocity of 0.71 m/s, while the maximum cavity size for concave ball is seen in Figures 3-15 and 3-16 image d at a velocity of 0.5 m/s. The reason behind this difference is explained in greater detail in the next section.

In the mid velocity region the cavity size is slightly smaller for the concave cone than for the concave ball, compare Figure 3-15 image j and Figure 3-18 image j. Of special note is the difference in cavity size between images f and g in Figure 3-19. This sudden change in cavity size is a result of the projectile not pinning a contact line at the higher velocity and only being fed by the air trapped in the concave shape.

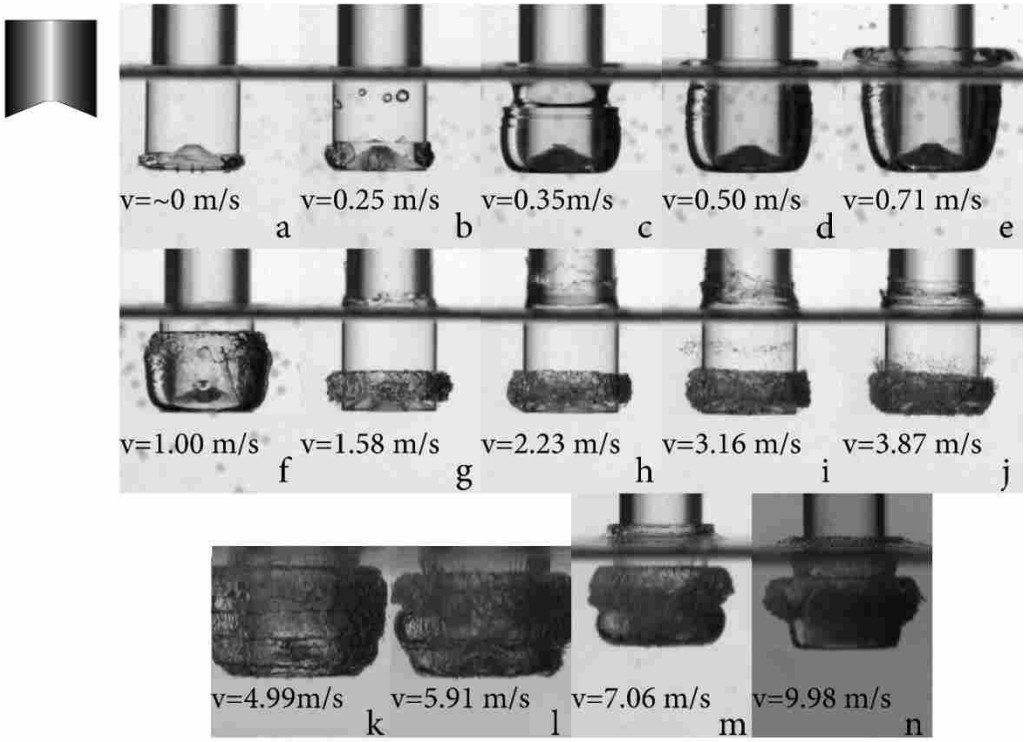

Figure 3-19. Cavity shape as a function of speed for the concave cone nose shape. Images are taken at approximately 1 D below the surface and come from the same drop tests as Figure 3-18. The cavity types are similar to the concave ball with slightly different cavity sizes at different velocities. Comparing this with Figure 3-18 the three regions show similar cavity shape at both depths.

The differences and similarities in the formation and growth of the cavities for the concave ball and concave cone can be seen in comparing Figure 3-17 and Figure 3-20. Aside from the differences in resulting cavity shape, as discussed earlier, the concave cone forms a ring cavity faster at high speed than the concave ball (compare images 3b-c for each). Also the concave cone forms a jet faster than the concave ball, but to a much smaller extent (compare Figure 3-20, images 3c-3f with Figure 3-17, images 3f-3g).

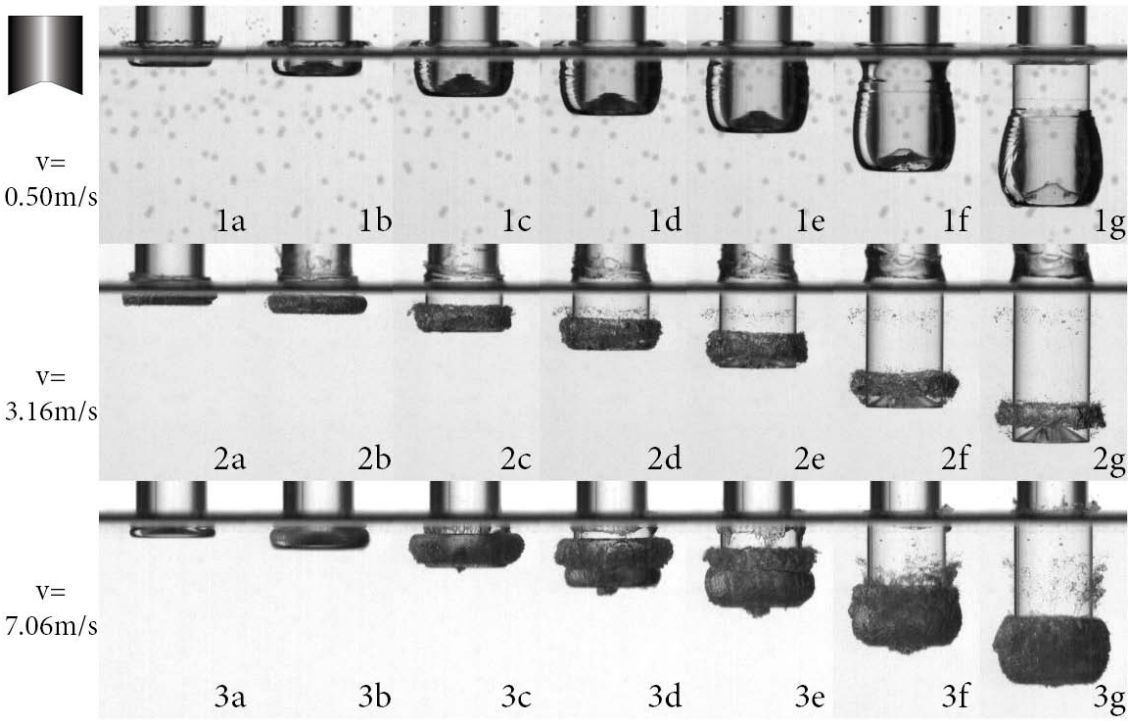

Figure 3-20. Progression of the three cavity types for the concave cone shape. The projectile depths for the image series are as follows: a. 1/8 D, b. ¼ D, c. ½ D, d. ¾ D, e. 1 D, f. 3/2 D, g. 2D. Image series 1 shows the progression of the cavity at a velocity in the middle of the first region (v=0.5 m/s) and is similar to a classic cavity progression. Image series two shows the cavity progression in the second region at v=3.16 m/s. In this region a ring cavity forms, which is filled with the air initially trapped in the concave cone (image 2b-c). Image series 3 shows the cavity progression in the third region, at v=7.06 m/s, where a small contact line is initially pinned and quickly pinches off on the body (images 3a-b). The cavity then rapidly fills with the air trapped in the concave ball (image 3c) and forms an unsteady pressure flow.

These results show the effect of velocity on the cavity formed by the two main concave shapes. There are three distinct regions of velocity which will cause different cavities to form and are grouped by low, mid and high velocities forming classic cavities, ring cavities, and a mix between classic and ring cavities respectively. These are discussed further in the following sections.

3.2.3 Effects of geometry on the cavity in the low and mid velocity regions

At low speeds there are distinct differences in the cavities made between the shapes which helps to show how the geometry affects the cavity formation, as seen in Figure 3-21 and Figure 3-22. In Figure 3-21 the concave ball and concave cone form distinct classic cavities while the flat shape only forms a small partial cavity.

In Figure 3-22 the concave ball, concave cone and flat all form classic cavities, although different sizes. This brings up some interesting questions. Why were the concave ball and concave cone able to form distinct classic cavities while the flat shape was not? Why did the concave ball and concave cone form similarly sized cavities at the velocity tested in Figure 3-21 and then form differently sized cavities at the higher velocity tested in Figure 3-22? The answer to these lie in the geometry of the concave shape and how it affects the trapped pocket of air. As the projectiles enter the water the air from the concave nose vents and forces the water pinned at the radial tip of the projectile off of the projectile until a large portion or all of the air inside the concave nose has vented out. While the air vents from the concave nose shape, air is also entrained by the cavity from the surface. Once the air ceases to vent from the concave shape a contact line finally pins to the projectile, see Figure 3-23, image e. The reason the concave cone cavity is so much larger than the concave ball cavity (at 0.7 m/s) is the difference in the depth of the concave cutout, and the effect on the cavity formation. The concave ball has a deep pocket

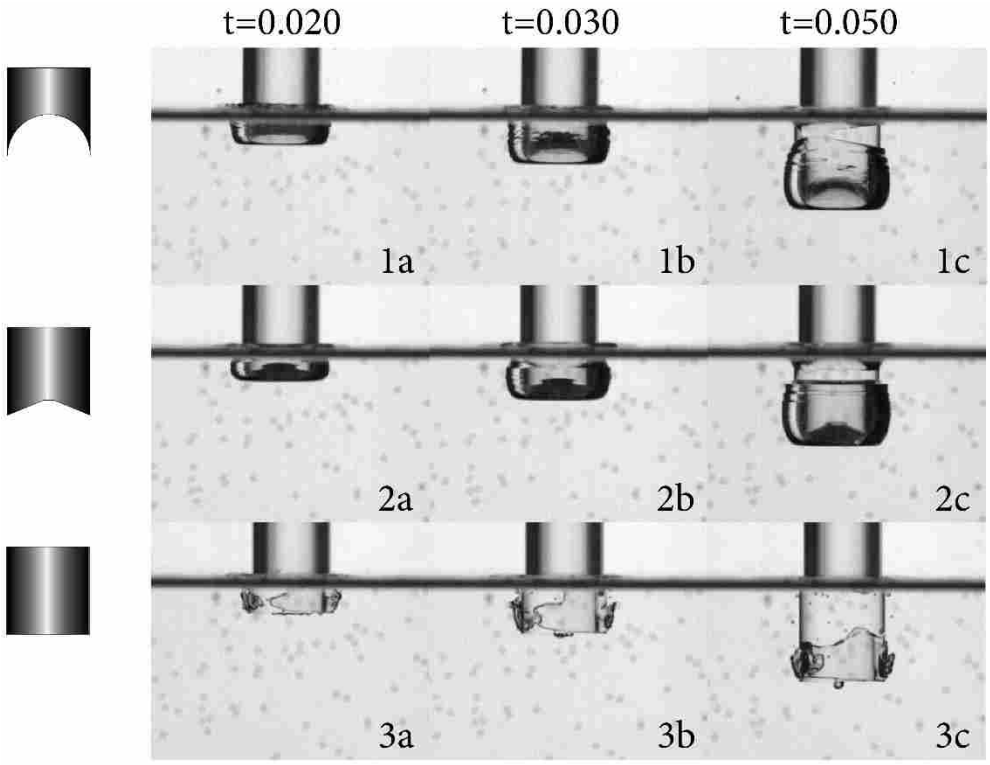

Figure 3-21. Comparison of concave ball, concave cone, and flat shapes at very low speeds (Ca=0.006 v=0.35 m/s). Images show the cavity progression at three different times after impact (t = 0.020, 0.030, 0.050 s). The difference in cavities formed is especially prevalent at this low speed and show the various effects of different concave geometry. Notice that the flat shape only formed a small partial cavity while the concave shapes formed full and comparatively larger classic cavities. The larger cavities formed by the concave shapes is a result of forcing the trapped air out of the concave nose after impact and causing the flow to separate from the projectile and fill with air from the concave nose as well as the surface.

with sharp edges and a large volume of air, while the concave cone has a comparatively shallow pocket with gradually rising edges and a less overall volume of air. The shape of the concave ball allows the air to be trapped and compressed, whereas the shape of the concave cone does not provide as effective trapping or as much room for compression. This lack of trapping and compression seems to allow the air to be forced out of the concave cone sooner and more rapidly than the concave ball. This in turn forces the flow off the edges of the concave cone and allows a relatively large cavity to develop, fed by air from the concave cone as well as from above the

water surface. The comparatively delayed venting of the concave ball allows it to descend into the water further before venting, making the air in the concave ball less effective at separating the water flow from the projectile, which results in a smaller cavity. Figure 3-22 shows the first few moments of entry for the concave ball (images 1a and 1b) and concave cone (images 2a and 2b). The evidence of the flow being forced off the edges of the concave cone is the presence of the splash curtain which is not apparent in the entry of the concave ball. The key parts of the entry of the concave shape at low velocities are illustrated in Figure 3-23.

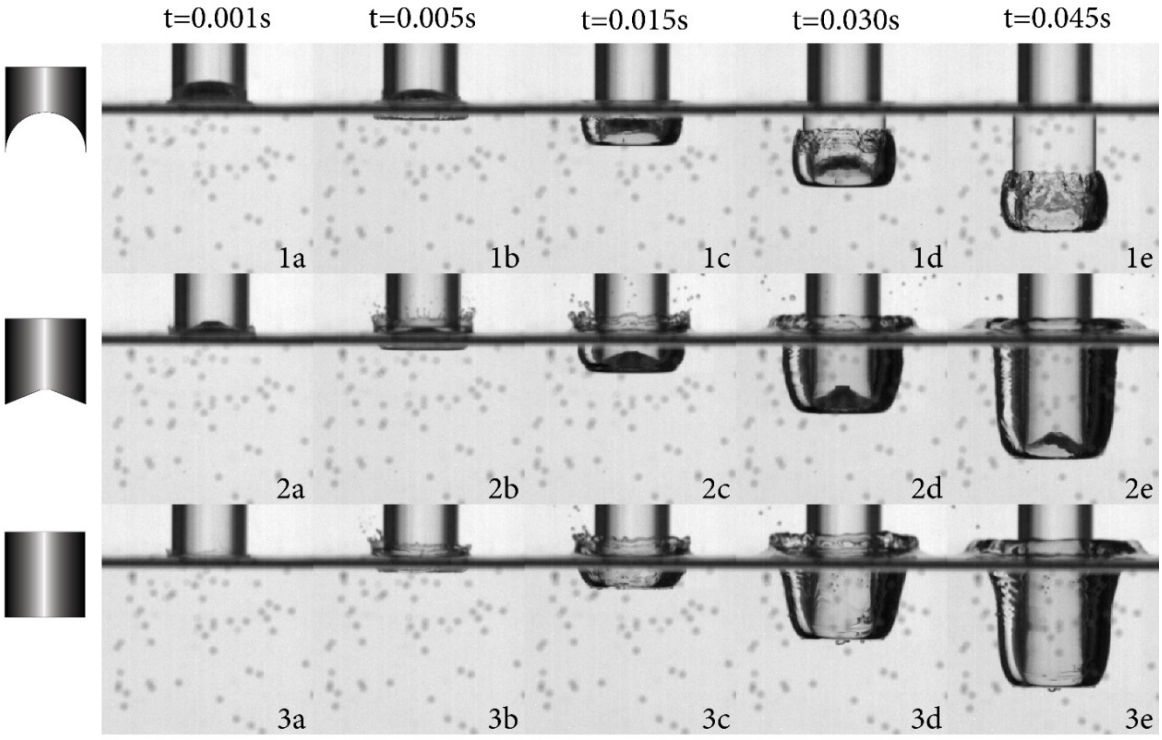

Figure 3-22. Comparison of the concave ball, concave cone, and flat nose shapes at low speeds (Ca = 0.012, v = 0.706 m/s). In the first few moments of impact the air from the concave cone pushes the flow out and off of the projectile forming a visible splash curtain, while the air from the concave ball does not. Consequently the concave cone forms a larger cavity. Notice how the concave cone and flat nose shapes formed similarly sized cavities while the concave ball formed a much smaller cavity.

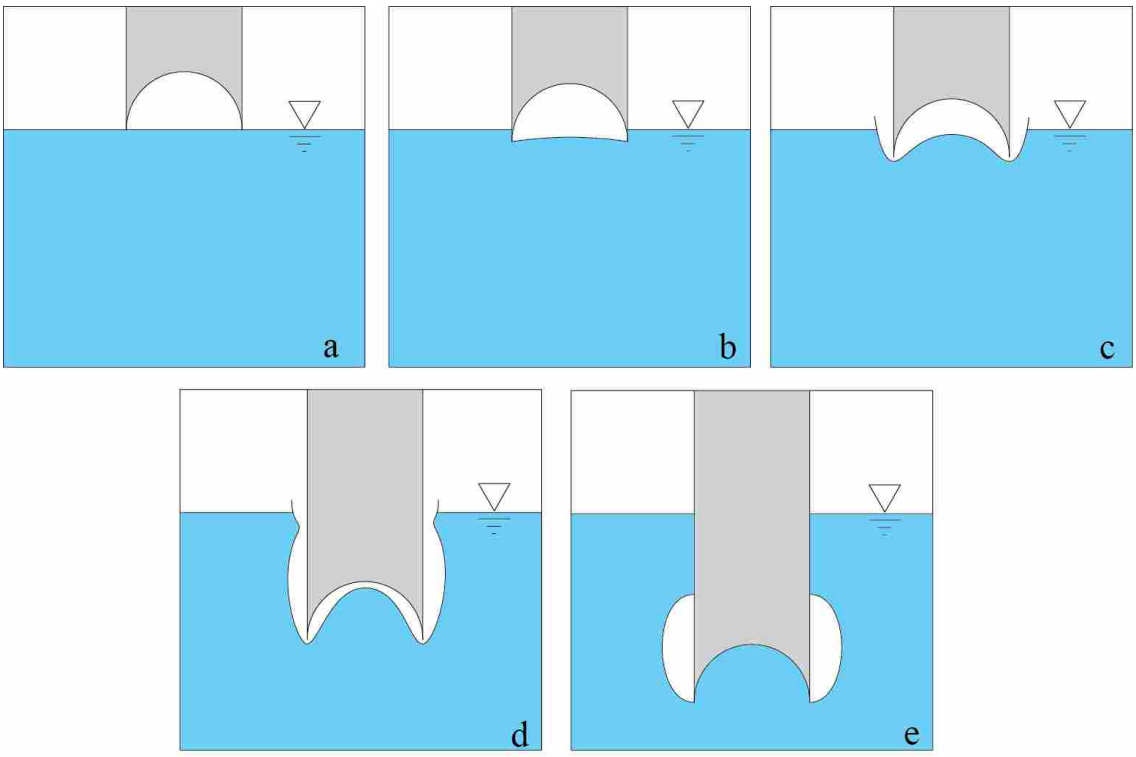

Figure 3-23. Illustration of the cavity behavior of the concave shapes at low velocity. As the projectile nears the water surface, the water surface deforms slightly, image a. When the leading edge of the projectile touches the water surface the air in the concave shape is trapped, image b. The air trapped in the concave shape is then forced by the intruding water out around the leading edge, which separates the flow off the projectile, forming a cavity, image c. The cavity fills with air, both from air trapped in the concave shape, as well as from the surface, image d, and eventually pinches off, both at the leading edge and on the walls of the body, image e. Note that the gap of air in between the projectile and water have been exaggerated for illustrative purposes.

As the impact velocity of the projectiles increase (1 m/s < v < 4 m/s) the leading edge of the concave shape is able to penetrate farther into the water before the air vents from within the concave region, preventing flow separation and allowing the ring cavity to form. As seen in Figure 3-24, the concave cone and concave ball entries are fairly similar at this velocity (v=3.16 m/s) with the exception of the size of the cavity and the small jet of air emitting from the concave ball in image 1c of Figure 3-24. The concave cone forms a smaller cavity than the concave ball because it has a smaller concave volume and consequently has a smaller amount of

air to form the ring cavity with. The formation of the jet by the concave ball will be discussed in section 3.2.4.1.

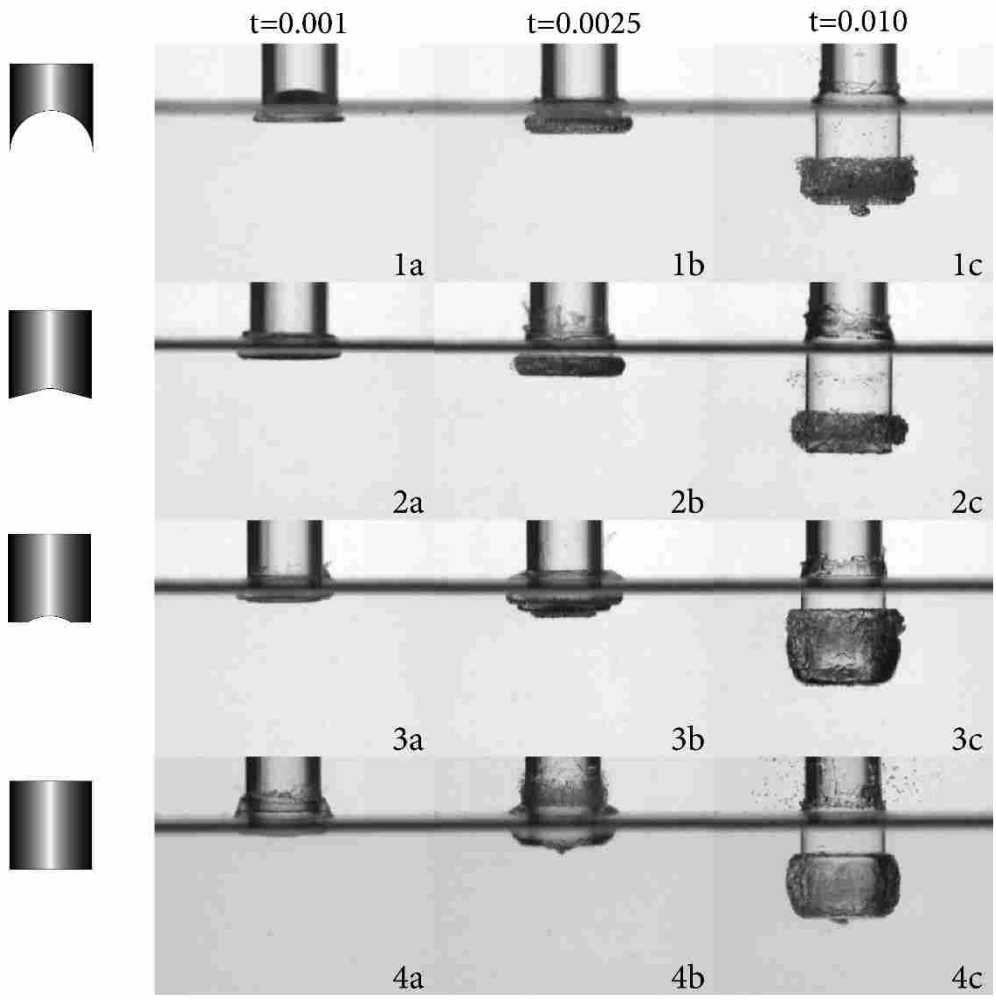

Figure 3-24. Comparison of the various concave shapes at a moderate velocity, Ca=0.053, v=3.16 m/s. In this second impact speed region the cavity shape changes. Nearly all the shapes create smaller cavities but for different reasons. The concave ball and cone shapes descend further into the water before the air vents out the leading edge of the projectile. This allows only a small contact line to be pinned before it pinches off and fills with air trapped in the concave shape, allowing a ring cavity to form. The partial and flat shapes form classic cavities and look similar after the initial impact (images 3c and 4c). The partial shape also vents the air trapped in its concave section below the surface of the water that makes its cavity slightly larger than the flat shape.

Also at this impact speed, the flat shape pins a contact line and creates a splash curtain that rises rapidly and collapses on the projectile soon after formation (image 4a, 4b). This rapid splash curtain formation and collapse causes the flat shape to form a smaller cavity than it did at the slower velocity (v=0.706 m/s), compare Figure 3-24, image 4c with Figure 3-22, image 3c.

The partial concave ball is introduced at this impact velocity and also pins a contact line and creates a cavity, but its splash curtain collapses even faster than the flat (image 3a). The flat and partial concave ball have similar looking cavities after the projectiles have descended further into the water. The cavity from the partial concave ball (image 3c) is slightly larger than the flat (image 4c), likely due to the air entrained by the concavity. The partial ball also helps explain the difference in the initial impact between the concave shapes and the flat shape. Comparing image series a between the shapes we can see that as the concave volume decreases, the height of the splash increases. This is because the air in the concave shape acts as a spring and cushions the impact. Thus the smaller the volume of air, the more the cushion, and the smaller the splash at impact.

3.2.4 Effects of geometry on the cavity in the high velocity region

3.2.4.1 Jet formation

The entry of the concave shapes in the third or high speed region is compared in Figure 3-25. In this region the cavity shape is initially smooth as it pins a contact line and begins to form a small classic cavity. We observe however, that the cavity walls become rough and disturbed about the time when the classic cavity begins to collapse and the trapped air vents from inside the concave nose into the classic cavity. Also of interest in this region is the formation of a high speed jet emitting from the center of the concave region. Although the jet also forms at lower

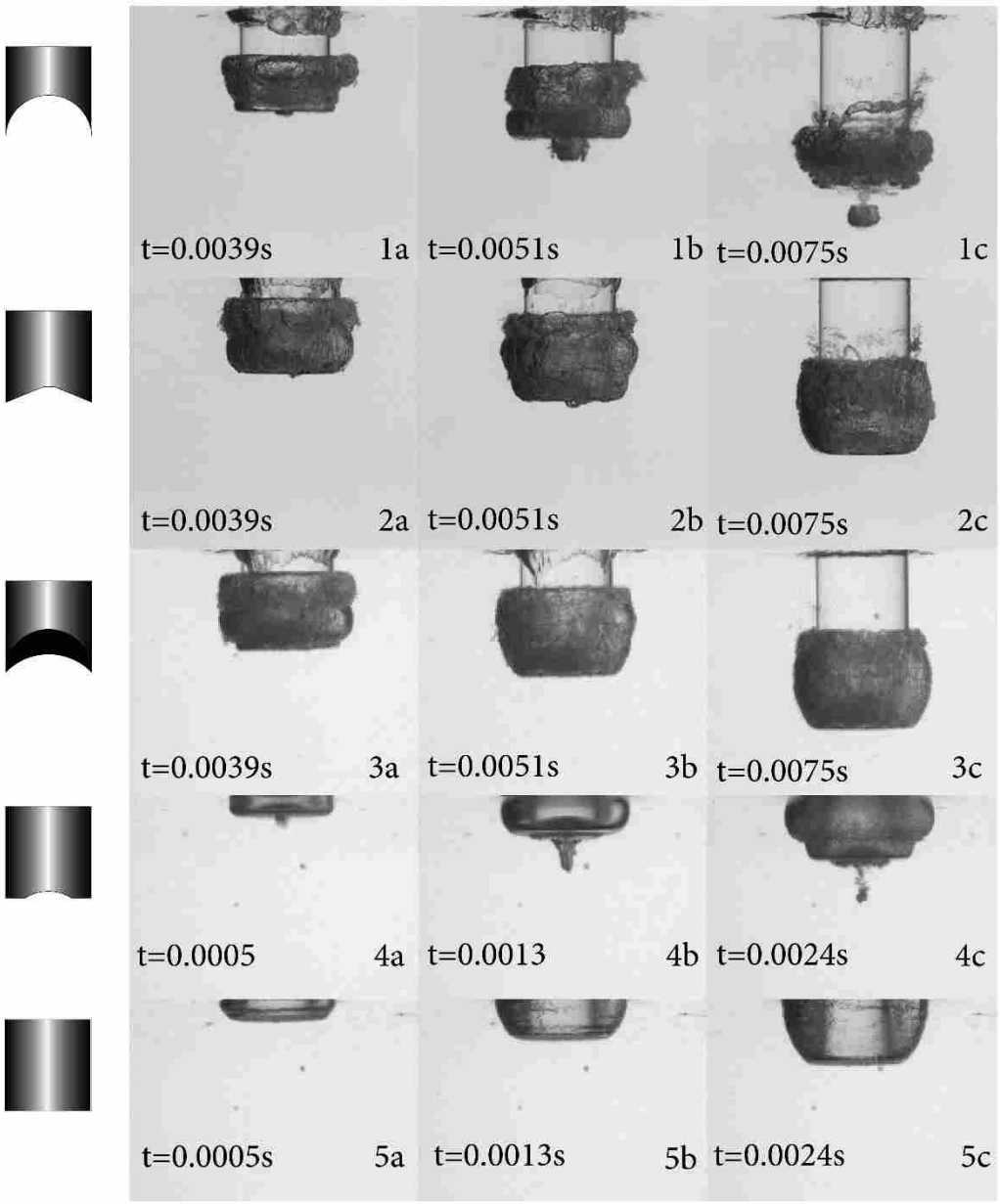

Figure 3-25. Effect of concave shape in third or high speed region. The concave ball and partial concave ball formed jets while the concave cone, half volume concave ball, and flat did not. Of note is the evidence of a jet as a small bubble seen in images 2 a-b. The concave cone seemed to form a jet but it did not grow as large or last as long as the jet formed by the concave ball.

impact velocities (observed as low as v=3.16 m/s) the jet is particularly prominent at high speeds and will be discussed in the context of the high speed region. The concave ball and partial concave ball each formed a well-defined jet, although at different times, while the half volume

concave ball did not visually form a jet. The concave cone did form a small jet but did not last long. Similar small jets were observed for the concave cone in some repeat tests but none lasted long or made it very far beyond the leading edge of the projectile.

To more fully investigate the flow in the concavity and the jet formed in the high impact speed region, the entry was filmed from below and to the side of the projectile at 8000 fps. Figure 3-26 shows the initial part of the entry where the ring cavity and jet are formed and Figure 3-27 roughly illustrates a cross section view of what is happening inside the concave shape. The leading edge of the projectile descends into the water in Figure 3-26 a, and Figure 3-27 a, trapping the air inside the concave nose. The air is then compressed as the projectile descends, Figure 3-26 b-f and Figure 3-27 b-c. In Figure 3-26 d-f and Figure 3-27 c-d the surface of the air inside the concave nose domes upward as the air is forced over and down the edges. The air vents from the concave shape into the surrounding classic cavity and rapidly forms a ring cavity, Figure 3-26 g-k and Figure 3-27 d. The air eventually stops venting and retreats back into the nose shape. At the same time the bottom edge of the ring cavity is pulled down and stretched by the leading edge of the projectile, Figure 3-26 l-p and Figure 3-27 e. In Figure 3-26 q-y and Figure 3-27 e-h the top toroidal part of the ring cavity flows down into the stretched bottom part along the shaft of the projectile. This momentarily forms two rings of air, Figure 3-26 t and Figure 3-27 f, which then continue to combine into one cavity. An interesting note is how the jet formed from within the concave nose, Figure 3-26 images i-y and Figure 3-27 b-i. This jet is produced by a small amount of water that infiltrates its way behind the trapped pocket of air during the first few moments of entry, Figure 3-27 images b-c. Evidence of this is the curved edge of the air surface in Figure 3-26 image d. This indicates that water has passed around the edge of the air surface along the internal wall of the concave shape. This water is what forms the

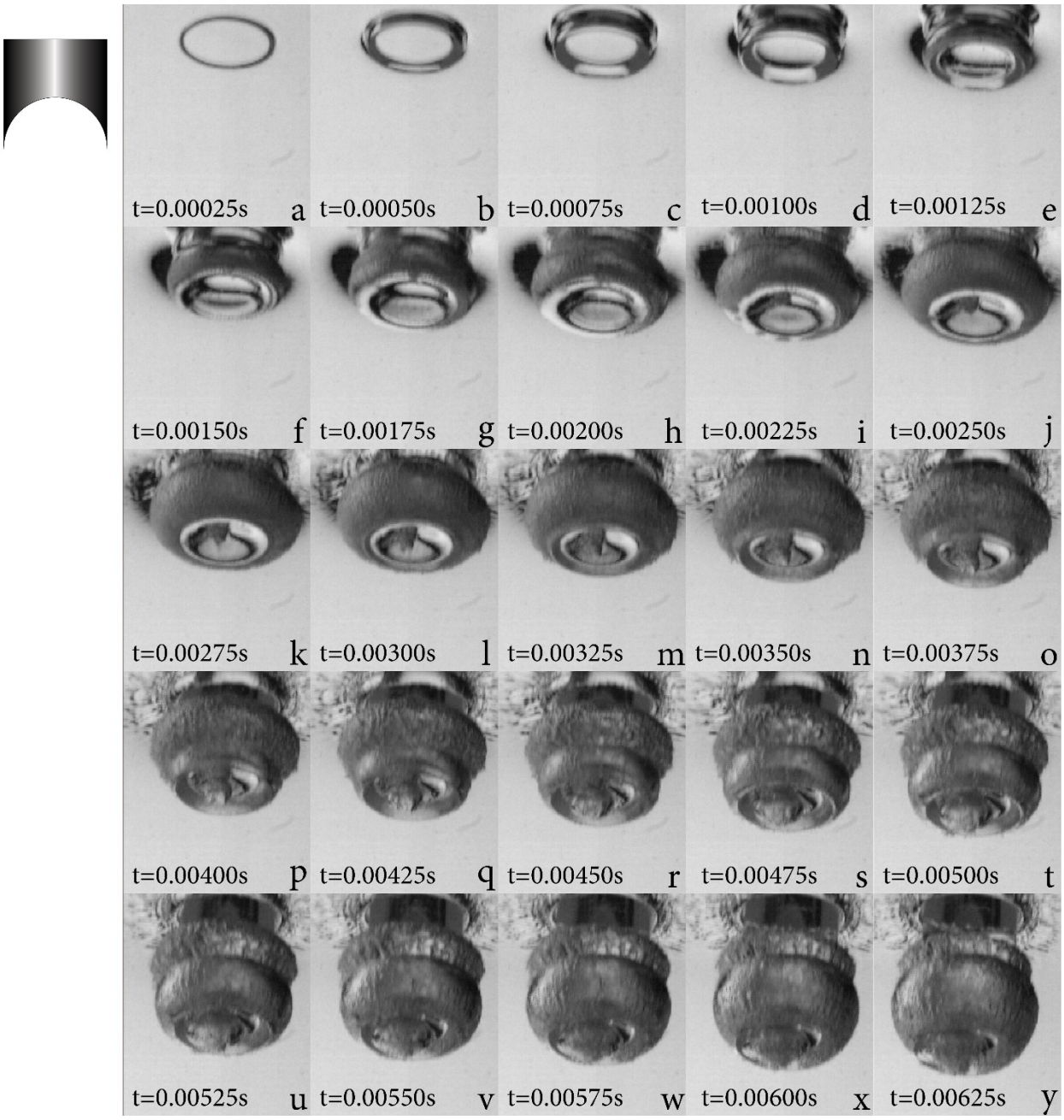

Figure 3-26. Evolution of the cavity and flow within the concave shape at high impact velocity as seen from below. The leading edge of the projectile descends into the water in image a, trapping the air inside the concave nose. The air is compressed as the projectile descends, images b-f. In images d-f the surface of the air inside the concave nose domes upward as the air is forced over and down the edges. The air vents from the concave shape into the surrounding classic cavity and rapidly forms a ring cavity, images g-k. After the air stops venting, image l, the bottom edge of the ring cavity is pulled down and stretched by the leading edge of the projectile, images l-p. In images q-y the top part of the cavity flows down into the stretched bottom part along the shaft of the projectile. The jet is formed by water that infiltrates behind the air pocket, along the internal wall of the projectile, and is further illustrated in Figure 3-27.

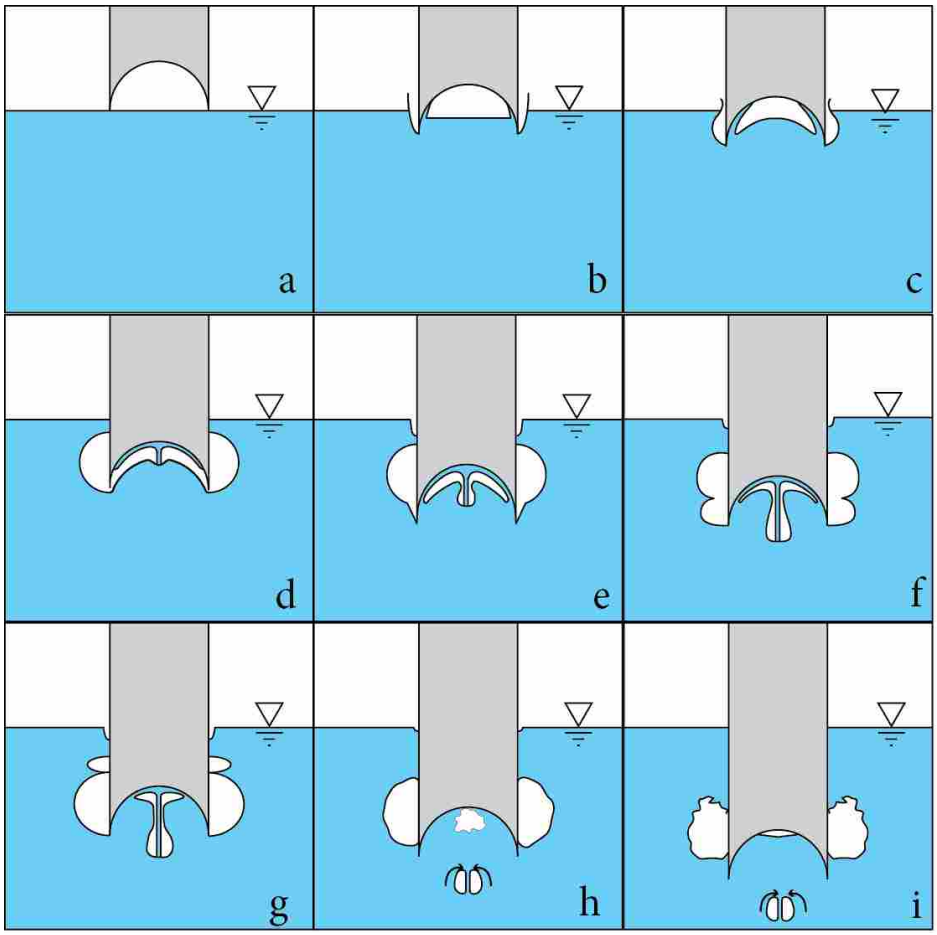

Figure 3-27. Illustration of the unsteady pressure event. Of special note are the air intrusion and formation of the jet. As explained in Figure 3-26, the trapped pocket of air causes the formation of the ring cavity (images a-d). Just after impact the water passes behind the trapped air along the wall and then forms a jet at the top of the concave shape that forces its way downward through the trapped air, entraining a bubble (images b-g). At the same time the jet is forming, the ring cavity stretches and an air intrusion from the water surface is observed, indicating that pressure in the fluid has fallen below atmospheric pressure, (image e). When the second ring cavity forms the air intrusion retreats to the surface, (image f). Also about the time the second ring cavity forms, the jet progresses beyond the bottom edge of the concave ball (images g-i). In some cases the jet will form a small vortex ring (images h, i), see also images m-o of Figure 3-33.

jet, starting in Figure 3-26 image i and Figure 3-27 image d, that grows throughout the rest of the images shown in each figure. It can be thought of similar to a Worthington jet. Water from all sides meet at a singular point at the top of the concave shape and combine into a single strong jet that entrains air as it flows through the trapped air and down through the center of the concave

shape. The forceful impact of the water on the trapped pocket of air causes the ring cavity to form rapidly, and with the right internal geometry causes a jet to form during the impact.

The difference in forming a well-defined jet or not lies in the geometry of the concavity. The concave-ball and partial concave ball are both rounded geometries (and have the same internal curvature r=1.27 cm, only the partial is shallower) which facilitate the flow combining into a single jet. They also had a great deal of air left in the concave shape at the time the jet formed, giving the jet a large pocket of air to entrain. The two shapes that did not form well-defined jets have shallow concavities, as well as a flatter geometry/ curvature. In the case of the concave cone a small jet did form but it is unclear whether the geometry prevented a well-defined jet from forming, or if the concave cone did not entrain sufficient air to facilitate the air pocket needed for a well-defined jet. In the case of the half-volume concave ball it did have a rounded geometry, although flatter, yet did not form a jet. It is unclear why a jet was not observed, although it could be that not enough air was retained to facilitate the air entrainment.

3.2.4.2 Unsteady pressure event

At high speeds the concave shapes produce an unsteady pressure event, first reported by Mathai et al [27]. They used an embedded pressure transducer and found that the pressure of the air trapped at impact raises to more than double atmospheric pressure. They also found that the pressure oscillated throughout the initial entry. The high pressure they measured explains the compression of the air seen in Figure 3-26. We briefly explain the compression with the ideal gas law, PV=nRT, where n is the number of moles of gas, R is the gas constant, and T is the temperature of the gas. Comparing the state of the gas between impact and maximum pressure,

the equation becomes $P_1V_1 / (n_1RT_1) = P_2V_2 / (n_2RT_2)$. The impact happens very quickly and no air initially escapes so the values of T and n can be treated as constant. This reduces the equation to $P_1V_1 = P_2V_2$, where P_1 is the pressure at impact (atmospheric), P_2 is the peak pressure, V_1 is the initial volume of air, V_2 is the volume at the peak pressure (Mathai reported about 240 kPa absolute). If we rearrange and solve for V_2, we get $V_2 = P_1V_1/ P_2$, or roughly $V_2 = 0.42\ V_1$. The high compression of the air acts like a compressed spring in driving the oscillations seen in the flow.

PIV measurements show the effects of the unsteady pressure event on the flow surrounding the concave shape. The concave ball and concave cone were specifically studied, but evidence of an unsteady pressure flow was observed for the concave ball, half volume concave ball, and the concave cone. The partial concave ball was not investigated for an unsteady pressure event. The PIV results show that the flow field around the concave shapes is unsteady as illustrated in Figure 3-28. The air cavity that remains in the concave shape compresses and expands causing a flow field oscillation at the tip of the projectile as it descends through the fluid. The first expansion occurs at t = 1.8 ms after impact and imparts the largest velocity, while expansions at t = 4.4 ms and 7.6 ms impart similar oscillations at reduced velocities. These high velocity expansions are preceded and followed by compression of the air inside the concave shape and a decrease in the flow velocity at the nose as indicated at t = 3.8 ms and 6.2 ms.

The velocity data along several axial lines was extracted to track the velocity variation through time as indicated in Figure 3-29a. Figure 3-29b shows how the u and v velocity components and combined magnitude varied through time as gathered from the PIV results. Four data sets were taken one each at approximate radii distance of 0 r (center), ½ r, ¾ r, and r.

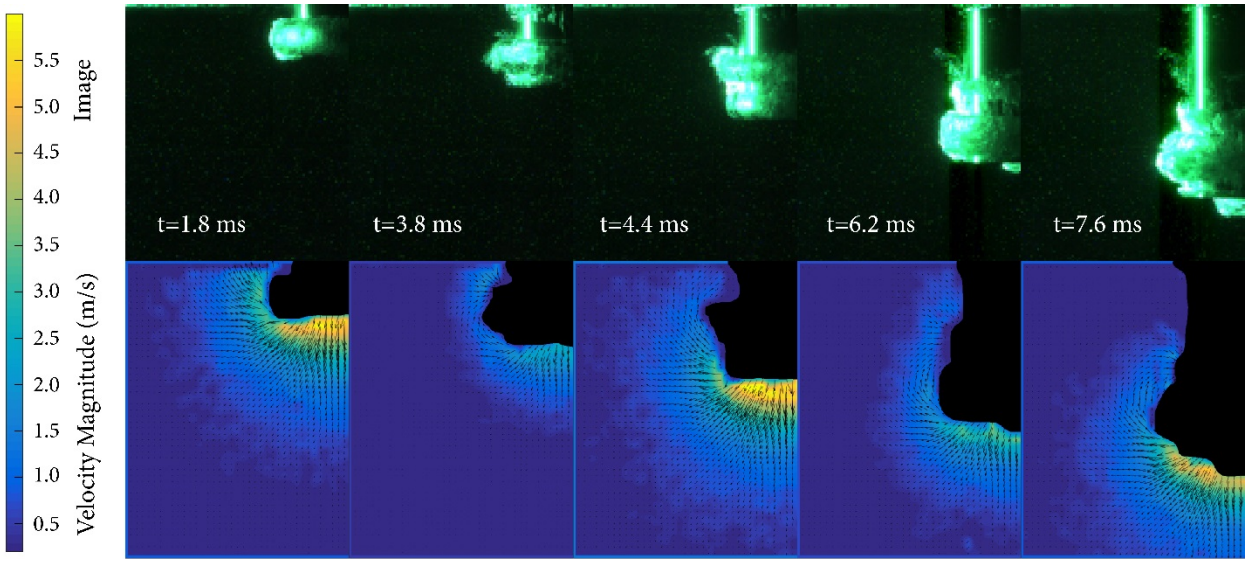

Figure 3-28. PIV evidence of the unsteady flow. The figure shows the original as well as the PIV images of the concave hemisphere for reference (top row and bottom row respectively). The velocity magnitude oscillates between high and low immediately around the projectile nose as the projectile descends into the water.

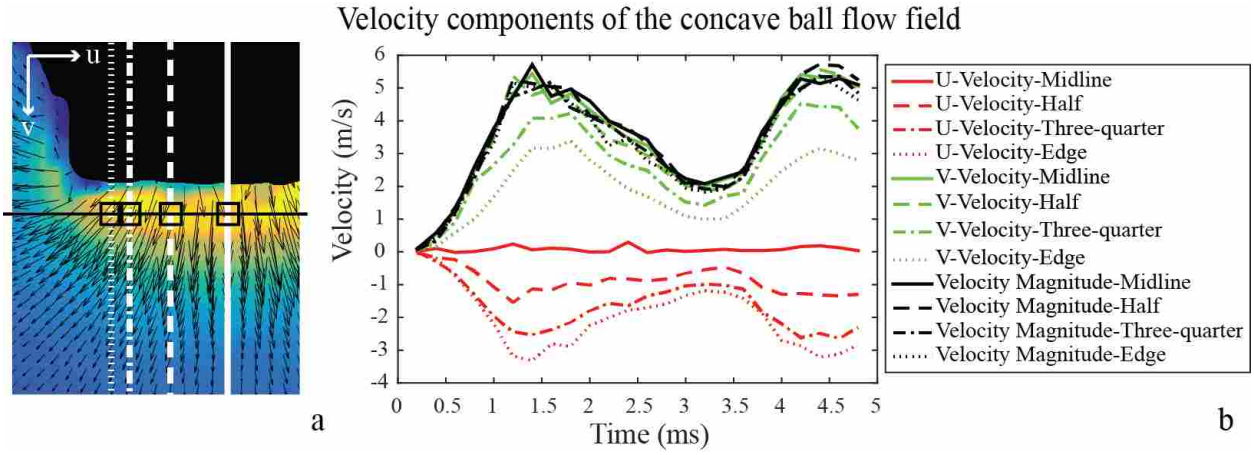

Figure 3-29. Velocity magnitude variation of the concave ball nose shape. The velocity magnitude and the u and v components were tracked at specific points on the radius (0r,1/2r, 3/4r, and r) through time at 4 mm ahead of the projectile (image a) . The chart shows how the u and v components, and velocity magnitude varied through time, indicating an unsteady phenomenon (image b).

Because the PIV data was not reliable at the immediate edge of the projectile mask, the data was taken at a distance of 5mm below the bottom edge of the projectile. Also, the data was truncated at the point where the jet first emitted from the concave ball because of the scatter in the data caused by the jet.

The Strouhal number, defined as $St = f\ D/v$ (where f is the frequency, D is the projectile diameter and v is the impact velocity), is used to describe oscillating flows and was calculated for the pressure oscillation data from Mathai et al. [27] and for the unsteady flow from the PIV data. The relevant non-dimensional numbers and other parameters for the two studies (Mathai and current) are listed in Table 3-2. An important note is that the values between the studies are not directly comparable since they come from two different measurements in the entry event.

Table 3-2. Relevant parameters to the unsteady entry event. The table shows current velocity oscillation data and Mathai et al's [27] pressure data. There is a distinct difference in the Strouhal number between the concave ball and concave cone nose shapes when comparing the initial period, measured from zero to the first minimum.

Data set	Non-Dim rebound # (Strouhal) min to min	Froude #	Initial period (ms) +/- 0.2	Diameter (cm)	Approximate volume (cm^3)
Mathai et al.	1.210	10.000	6	5.08	34
Al concave ball v 2	0.955	14.142	3.2	2.54	
Al concave ball	1.134	14.142	3.2	2.54	2.33
Acrylic concave ball	1.134	14.142	3.2	2.54	2.37
Acrylic concave cone	2.016	14.142	1.8	2.54	1.185

In comparing the values between the shapes in the current study there is a difference in period and consequently Strouhal number. The difference in period is linked to the difference in shape and volume. We found earlier that the air in the shallower concave cone vents more

quickly than the concave ball. For this reason the initial oscillation also occurs more rapidly for the concave cone than the concave ball. Although not directly comparable, the period as well as the volume of the concave shape in Mathai et al's [27] data is considerably longer and larger than the period and volume for either shape in the current study. This shows that the larger the concave volume, the longer the initial period and further supports the observation that the concave cone vents faster than the concave ball.

One difficulty in comparing pressure with velocity data is that the velocity will not reach a maximum until after the pressure reaches a maximum. In this case the velocity will not reach its first maximum (formation of the ring cavity) until the pressure is close to its second minimum (end of venting from the concave nose). For this reason care should be taken to not compare the values too closely between the studies.

Although the projectile diameter in the current study is half of the diameter in the study by Mathai et al., the cavity shape and timing appear to be similar at similar impact speeds at a depth of 1 diameter below the surface, see Figure 3-30.

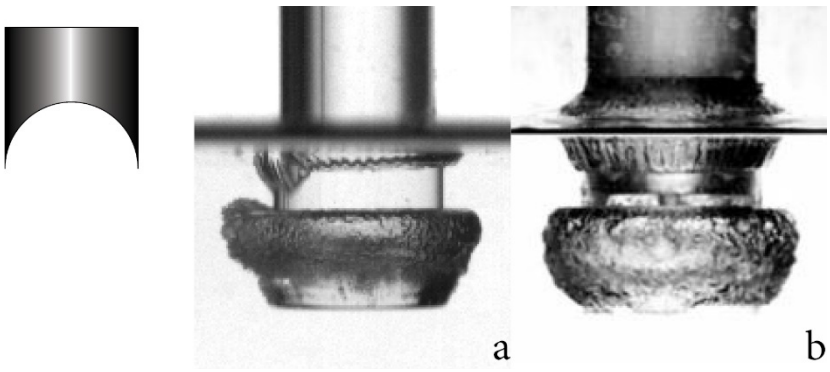

Figure 3-30. Comparison of the current data with Mathai et al's [27] data. Image a is the current data with a diameter of 2.54 cm and Image b is Mathai's data with a diameter of 5.08 cm. Each is at 1 D below the surface. Notice the key similarities between the two images. Each shows the intrusion of air at the surface and the iconic ring cavity. Image b used with permission.

3.2.4.3 Projectile wettability/ roughness

While the cavity formed by the concave shape is predictably affected by entry speed and projectile shape, the wettability of the projectile surface does not seem to have an effect on the cavity formed in the third or high impact speed region. Because the cavity dynamics are dominated by the trapped pocket of air in the high speed region, it is logical that the surface conditions would have a lesser if any effect. Figure 3-31 shows the entry of a concave ball with three different wetting conditions, image series 1, 2, and 3 respectively. Despite the variety of

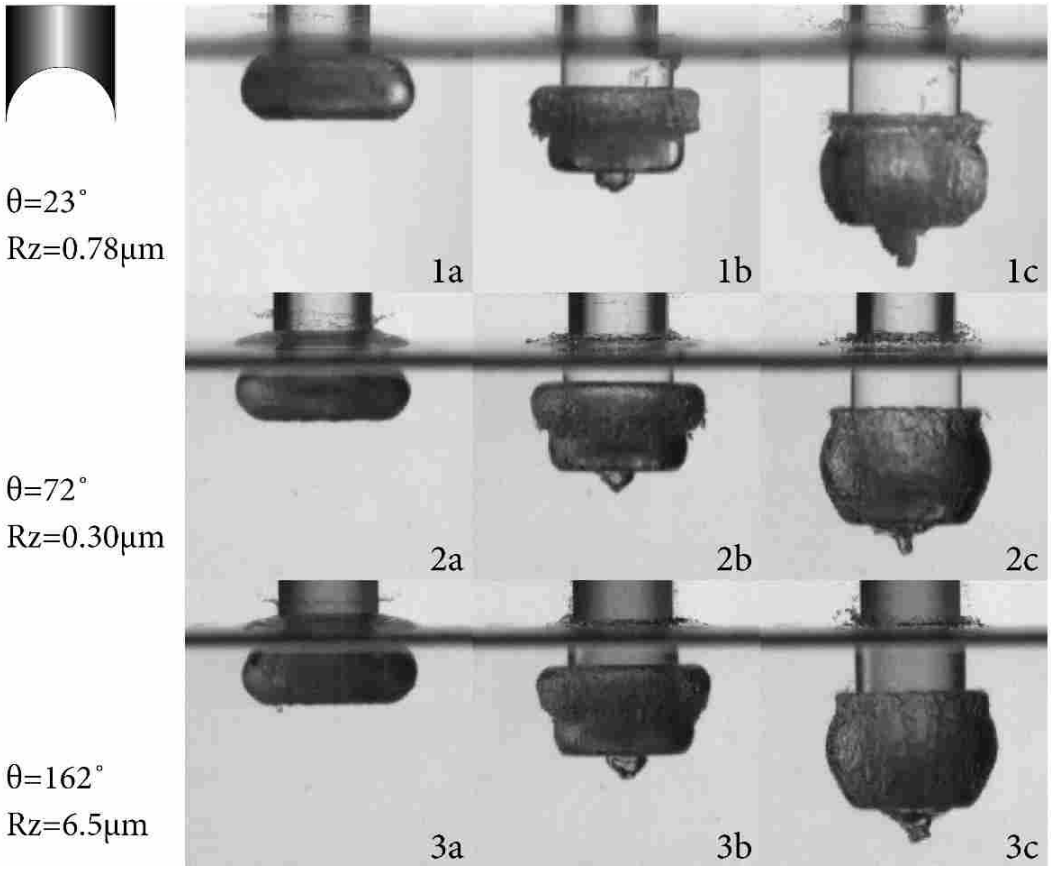

Figure 3-31. Entry of the concave ball shape at Ca=0.118, v=7.06 m/s, with several different wetting conditions. Image series a, b, and c, are at 1/2 D, 1 D, and 1 1/2 D below the surface respectively. Interestingly the cavity shape is similar at each depth for every wetting angle, and is thus independent of wetting condition at this entry speed.

wetting conditions between the entries the cavity shape is similar at each stage of the entry, showing that the surface wettability has little or no effect on the shape of cavity created.

3.2.5 Other factors

Concave drop tests were not only done with acrylic projectiles, but also with aluminum. The acrylic projectiles were used for a majority of the tests because their transparent nature allowed us to see the cavity formation more clearly as well as see into the pocket to a certain degree. The aluminum material allowed a slightly deeper pocket to be machined with sharper edges at the radial edge of the nose, where this was not possible with the acrylic. The entry of the aluminum concave ball and the acrylic concave ball at v=7.06 m/s are compared in Figure 3-32 and Figure 3-33. There are subtle differences in the entry of each that are worth mentioning.

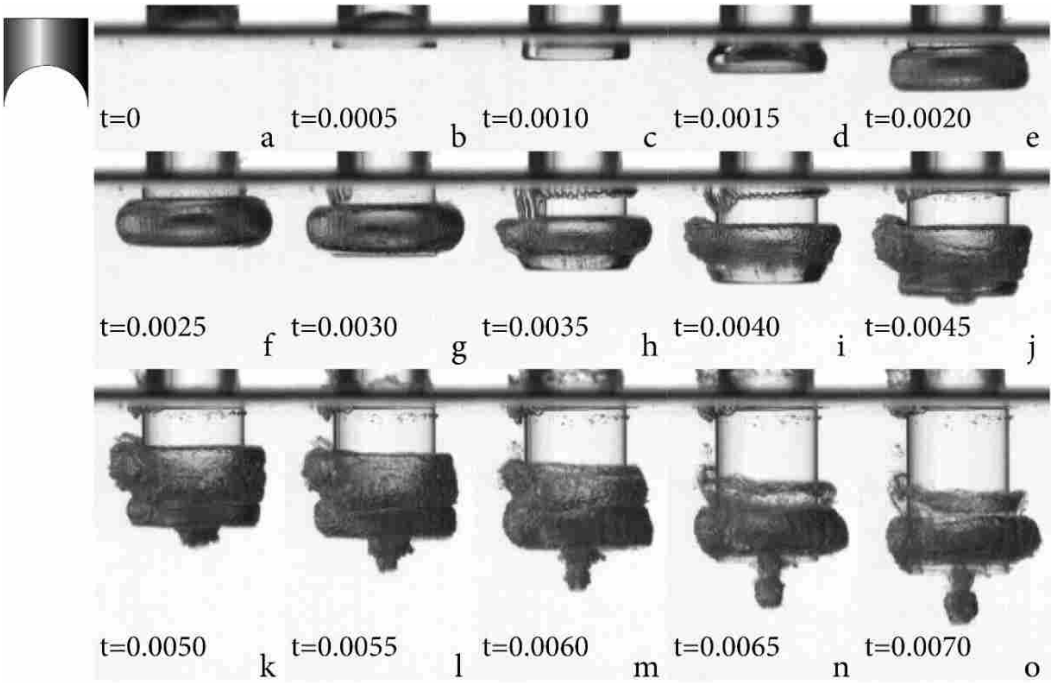

Figure 3-32. Time evolution of the entry of the acrylic concave ball, compare with the aluminum entry in Figure 3-33. The acrylic concave ball forms a noticeable classic cavity, images a-d. Notice also, that in image h the air from the surface successfully intrudes into the ring cavity.

The acrylic shape visibly pins a contact line and forms a classic cavity, Figure 3-32, images a-d. The aluminum shape also forms a classic cavity, but the pinned contact line is nearly indiscernible and the classic cavity formed comparatively smaller, Figure 3-33, images a-c. This is likely due to the sharper edge of the aluminum projectile. Also for the acrylic shape there is a portion of the air intrusion that penetrates into the ring cavity, Figure 3-32, image h. However, this is not observed in the aluminum entry, Figure 3-33, image g. It is not clear what factors contribute to air penetrating into the ring cavity or not, whether it is the slight difference in geometry, density, or some other factor. Lastly there is a small and tight vortex ring produced

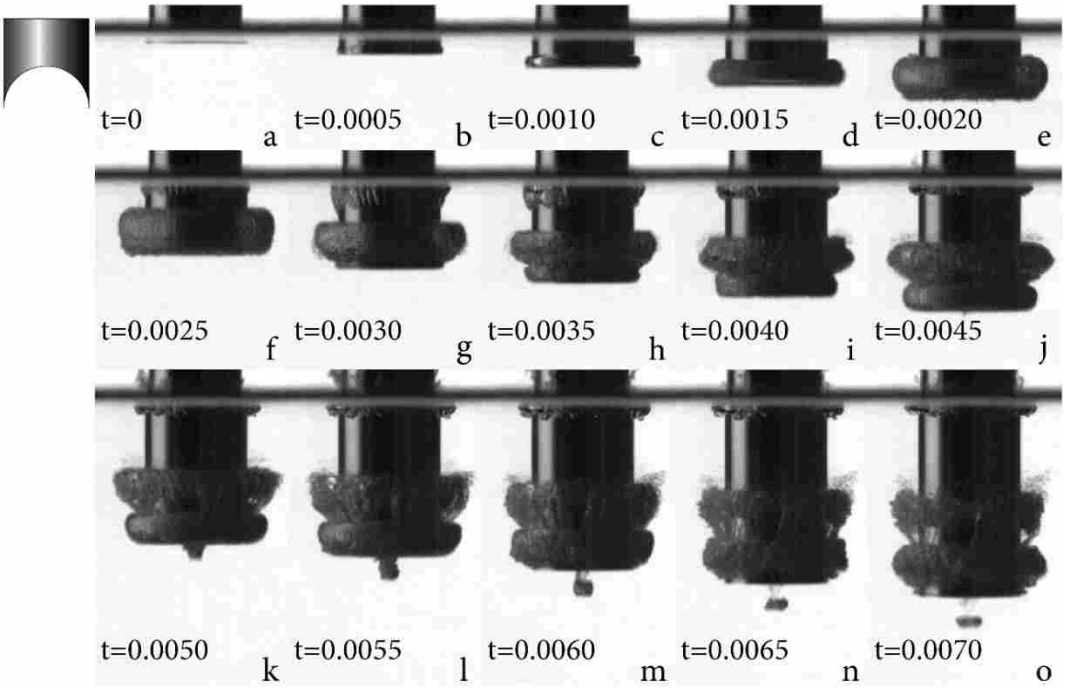

Figure 3-33. Time evolution of the entry of the aluminum concave ball, compare with acrylic concave ball in Figure 3-32. The aluminum concave ball forms a nearly indiscernible classic cavity, as compared to that of the acrylic concave ball. Notice that in image h the air from the surface does not intrude into the ring cavity. Also notice the formation of a distinct vortex ring in image o.

by the aluminum shape, see Figure 3-33 images j-o, which is emitted ahead of the main jet (not shown), while no vortex ring is initially observed from the acrylic shape, but only a large jet, see Figure 3-32 images j-o. This may be linked to a greater compressive ability of the aluminum shape due to its slightly deeper pocket and sharper edges.

4 CONCLUSIONS AND RECOMMENDATIONS

The purpose of this research was to determine the effect of shape, both concave and convex, on cavity formation. Shapes were tested through a range of wetting angles ($15^\circ < \theta < 164^\circ$) and impact velocities (~0 m/s < v < 15 m/s). Convex nose shapes were investigated for the effect on the threshold velocity on cavity formation. The unique cavity formed by concave nose shapes was also investigated.

4.1 Effect of convex nose shape on the threshold velocity for cavity formation

The experiments show that convex nose shape has a significant effect on the threshold velocity for cavity formation. As compared to the data available for spheres, the streamlined axisymmetric shapes formed cavities at higher velocities, especially the cone and elliptical ogive shapes. Even the rounded flat shape, though much more blunt, had a threshold velocity above that for the sphere. The key difference between spheres and the shapes used in the current study (aside from the initial nose shape) is the region following the nose. The presence of a cylindrical shaft following the nose shape prevents pinning a contact line on the nose shape until a higher velocity is reached, as compared to nose shapes that are not followed by a cylindrical shaft.

Several parameters were developed to quantitatively distinguish between convex nose shapes and their potential influence on the threshold velocity. These parameters were tip bluntness, nose length, and shaft abruptness. A smaller value for tip bluntness or shaft abruptness will comparatively delay cavity formation as opposed to objects with a higher value for either.

Also a greater value for nose length will similarly delay cavity formation as opposed to a shape with a shorter nose length.

The threshold velocities for the ogive and cone nose shapes in the hydrophilic region could not be determined because an imbalance of gravitational and drag forces would deflect the trajectory of the projectile before impact so that it would not have a vertical entry.

4.2 Effect of concave nose shape on cavity formation

The research determined that concave shape has a significant effect on cavity formation. The factors of concave shape, and impact speed were found to make a difference in the type of cavity formed. Three main regions of impact velocity determine the type of cavity. In the low speed region the concave shape forms a cavity with a smooth wall as the trapped air in the concave shape vents out and forces the flow off the leading edge of the projectile. Near the top of the low velocity range, and depending on the concave nose shape, a large cavity will form filled by air from the concave nose shape as well as entrained from the surface. In the middle velocity range the concave shape vents the trapped air beneath the surface of the water without separating the flow off the leading edge of the projectile, and forms a ring cavity that is filled only with air from the concave shape and is maintained in a ring shape by vorticity. In the high speed range the concave shape initially pins a contact line and forms a small cavity while the air in the concave shape is compressed. The air vents rapidly from the concave shape, as the initial small cavity collapses, and forms a large ring cavity with strong vorticity.

The compression and rapid release of the trapped air creates an unsteady flow field. The time at which the air vents and the period of oscillation is influenced by the volume of air in the concave nose shape. The concave cone had a shorter period of oscillation than the concave ball shape for this reason.

A jet was seen to form within the concave ball shape in the middle and high velocity regions during entry. The jet is formed by water infiltrating behind the air trapped in the concave nose shape along the inside walls, and combining at the top of the shape to form a Worthington jet. This jet then entrains the trapped air as it is forced down through the center of the concave shape.

Another interesting finding is that wetting angle had no effect on the shape of the cavity formed by the concave shape in the high speed region. We conclude that the trapped pocket of air has a large influence on the cavity formed by the concave shape through all velocities tested.

4.3 Recommendations

This study could be further expanded by determining the threshold velocity for the ogive and cone nose shapes in the hydrophilic region. This could be addressed by altering the design of the projectiles to reduce or eliminate the couple moment between the center of gravity and the center of pressure. It could also be addressed by changing the test set up to mechanically drive the motion of the projectiles instead of relying on free fall motion.

A more in depth study could also be performed to determine the effects of concave shape and concave volume on cavity and jet formation as well as the unsteady flow at high speeds. It would be useful to determine the exact time the air vents from the concave nose shape as a function of the impact velocity as well as the concave volume and or geometry. A deeper study into the formation of the Worthington jet formed by the concave ball shape detailing the impact speeds and other necessary parameters, including but not limited to concave volume and geometry, that are required for its formation would also be beneficial.

REFERENCES

[1] Truscott, T. T., Epps, B. P., & Belden, J. (2014). Water entry of projectiles. *Annual Review of Fluid Mechanics, 46*(1), 355-378. doi:10.1146/annurev-fluid-011212-140753

[2] Lee, M., Longoria, R. G., & Wilson, D. E. (1997). Cavity dynamics in high-speed water entry. *Physics of Fluids, 9*(3), 540-550. doi:10.1063/1.869472

[3] Aristoff, J. M., Truscott, T. T., Techet, A. H., & Bush, J. W. M. (2010). The water entry of decelerating spheres. *Physics of Fluids, 22*(3), 032102. doi:10.1063/1.3309454

[4] Yao, E., Wang, H., Pan, L., Wang, X. and Woding, R. (2014) Vertical Water-Entry of Bullet-Shaped Projectiles. Journal of Applied Mathematics and Physics, 2, 323-334. doi: 10.4236/jamp.2014.26039.

[5] Aristoff, J.M., & Bush, J.W.M. (2009). Water entry of small hydrophobic spheres. *Journal of Fluid Mechanics, 619*, 45-78. doi:http://dx.doi.org/10.1017/S0022112008004382

[6] Duclaux, V., Caillé, F., Duez, C., Ybert, C., Bocquet, L., & CLANET, C. (2007). Dynamics of transient cavities. *Journal of Fluid Mechanics, 591*, 1. doi:10.1017/S0022112007007343

[7] Guo, Z., Zhang, W., Wang, C. (2012). Experimental and theoretical study on the high-speed horizontal water entry behaviors of cylindrical projectiles. *Journal of Hydrodynamics, 24*(2), 217-217-225.

[8] Kubota, Y., & Mochizuki, O. (2011). Influence of head shape of solid body plunging into water on splash formation. *Journal of Visualization, 14*(2), 111-119. doi:10.1007/s12650-011-0071-4"

[9] Banerjee, S. (2008). Simple derivation of Young, Wenzel and Cassie-Baxter equations and its interpretations. ArXiv e-Prints, http://arxiv.org/abs/0808.1460v1

[10] De Backer, G., Vantorre, M., Beels, C., De Pré, J., Victor, S., De Rouck, J., Van Paepegem, W. (2009). Experimental investigation of water impact on axisymmetric bodies. *Applied Ocean Research, 31*(3), 143-156. doi:10.1016/j.apor.2009.07.003

[11] Richardson, E. G. (1948). The impact of a solid on a liquid surface. *Proceedings of the Physical Society, 61*(4), 352.

[12] Bodily, K. G., Carlson, S. J., & Truscott, T. T. (2014). The water entry of slender axisymmetric bodies. *Physics of Fluids,* 26(7), 072108. doi:http://dx.doi.org/10.1063/1.4890832

[13] Truscott, T. T., Epps, B. P., & Techet, A. H. (2012). Unsteady forces on spheres during free-surface water entry. *Journal of Fluid Mechanics, 704*, 173.

[14] Shi, H., & Takami, T. (2001). Some progress in the study of the water entry phenomenon. *Experiments in Fluids, 30*(4), 475-475-477.

[15] Truscott, T. T., & Techet, A. H. (2009). A spin on cavity formation during water entry of hydrophobic and hydrophilic spheres. *Physics of Fluids*, 21(12), 121703. doi:http://dx.doi.org/10.1063/1.3272264

[16] Guo, Z., Zhang, W., Xiao, X., Wei, G., & Ren, P. (2012). An investigation into horizontal water entry behaviors of projectiles with different nose shapes. *International Journal of Impact Engineering, 49*(November), 43-43-60.

[17] Duez, C., Ybert, C., Clanet, C., & Bocquet, L. (2007). Making a splash with water repellency. *Nature Physics,* 3(3), 180-183.

[18] Gekle, S., Peters, I., Gordillo, J. M., van der Meer, D., & Lohse, D. (2010). Supersonic Air Flow due to Solid-Liquid Impact. *Physical Review Letters,* 104, 024501 (2010). arXiv:0909.3777v2 [physics.flu-dyn]

[19] Uber, B. D., & Fegan Jr, R. J. (1973). *Acoustic Signatures Accompanying Low-Velocity Water Entry* (Master's thesis), Retrieved from DTIC. (Accession No. AD0772846)

[20] Worthington, A. M., & Cole, R. S. (1897). Impact with a liquid surface, studied by the aid of instantaneous photography. *Philosophical Transactions of the Royal Society of London.Series A, Containing Papers of a Mathematical Or Physical Character, 189*, pp. 137-148.

[21] Worthington, A. M. (1908). *A study of splashes*. London: Longmans, Green, and Co.

[22] May, A. (1951). Effect of surface condition of a sphere on its Water-Entry cavity. *Journal of Applied Physics, 22*(10), 1219-1222. doi:http://dx.doi.org/10.1063/1.1699831

[23] Zhao, M., Chen, X., & Wang, Q. (2014). Wetting failure of hydrophilic surfaces promoted by surface roughness. *Scientific Reports, 4*, 5376.

[24] Ding, H., Chen, B, Liu, H., Zhang, C., Gao, P., & Lu, X. (2015). On the contact-line pinning in cavity formation during solid–liquid impact. *Journal of Fluid Mechanics, 783*, 504-525. doi:10.1017/jfm.2015.574

[25] Kubota, Y., & Mochizuki, O. (2009). Splash formation by a spherical body plunging into water. *Journal of Visualization, 12*(4), 339-346. doi:10.1007/BF03181877"

[26] Kubota, Y., & Mochizuki, O. (2010). Elemental structure of splash generated by a plunging solid body. *Journal of Flow Visualization and Image Processing, 17*(4), 359-369.

[27] Mathai, V., Govardhan, R. N., & Arakeri, V. H. (2015). On the impact of a concave nosed axisymmetric body on a free surface. *Applied Physics Letters, 106*(6), 064101. doi:http://dx.doi.org/10.1063/1.4907555

[28] Thoroddsen, S. T., Etoh, T. G., & Tahehera, K. (2003). Air entrapment under an impacting drop. *Journal of Fluid Mechanics, 478*, 125-134. doi:10.1017/S0022112002003427

[29] Hicks, P. D., & Purvis, R. (2011). Air cushioning in droplet impacts with liquid layers and other droplets. *Physics of Fluids (1994-Present), 23*(6), 062104. doi:http://dx.doi.org/10.1063/1.3602505

[30] Hicks, P. D., Ermanyuk, E. V., Gavrilov, N. V., & Purvis, R. (2012). Air trapping at impact of a rigid sphere onto a liquid. *Journal of Fluid Mechanics, 695*, 310-320. doi:10.1017/jfm.2012.20

[31] Takagi, K., & Dobashi, J. (2003-09-01T00:00:00). Influence of trapped air on the slamming of a ship. *Journal of Ship Research, 47*(3), 187-193.

[32] Raffel, M., Willert, C.E., Wereley, S., Kompenhans, J.. (2007). *Particle image velocimetry: A practical guide*. Heidelberg: Springer. doi:10.1007/978-3-540-72308-0

[33] Thielicke, W. and Stamhuis, E. J. (2014): PIVlab - Time-Resolved Digital Particle Image Velocimetry Tool for MATLAB (version: 1.40). http://dx.doi.org/10.6084/m9.figshare.1092508

[34] May, A. (1975). *Water entry and the cavity-running behavior of missiles.* NAVSEA Hydroballistics Advisory Committee Silver Spring, Maryland.

[35] Appendix C: Contact angle goniometry. (2009; 2009). Surface design: Applications in bioscience and nanotechnology (pp. 471-473) Wiley-VCH Verlag GmbH & Co. KGaA. doi:10.1002/9783527628599.app3

[36] Hommelwerke, (2002) Operating Manual: Turbo Roughness for Windows. Hommelwerke

[37] Bernardin, J. D., Mudawar, I., Walsh, C. B., & Franses, E. I. (1997). Contact angle temperature dependence for water droplets on practical aluminum surfaces. *International Journal of Heat and Mass Transfer*, 40(5), 1017-1033. doi:http://dx.doi.org/10.1016/0017-9310(96)00184-6

[38] http://www.accudynetest.com/polytable_03.html?sortby=contact_angle#istop

[39] Hilgenberg, S. P., Orellana-Jimenez, E. E., Sepulveda-Navarro, W. F., Arana-Correa, B. E., Alves, D. C. T., Campanha, N. H. (2008). Evaluation of surface physical properties of acrylic resins for provisional prosthesis. *Materials Research*, 11(3), 257.

[40] http://www.livescience.com/19630-water-repellant-coating-leaf.html

[41] http://www.cytonix.com/fluorothane.html

APPENDIX A. UNCERTAINTY FOR MEASURED AND CALCULATED CASSIE-BAXTER WETTING ANGLES

The uncertainty for the measured wetting angles is calculated by

$$U_\theta = \pm\sqrt{u_0^2 + u_1^2 + \left(S_{\bar{\alpha}} t_{\nu,P_{95\%}}\right)^2},$$

where u_0 is the dial uncertainty (0.5˚), u_1 is the uncertainty of the method (~3˚), $S_{\bar{\alpha}}$ is the true standard deviation and $t_{\nu,P_{95\%}}$ is the student's t distribution for the 95% confidence interval.

The Cassie-Baxter wetting angle as defined by Banerjee [9], is calculated as

$$\theta_{CB} = \cos^{-1}\left(r\, f_s\, \cos\theta_y + f_s - 1\right).$$

$\cos\theta_w$ can be substituted in for $r\cos\theta_y$ as seen in equation 3-3 in the text. The uncertainty in the Cassie-Baxter wetting angle is then

$$U_{\theta_{CB}} = \pm\sqrt{\left(\frac{\partial\theta_{CB}}{\partial f_s} U_{f_s}\right)^2 + \left(\frac{\partial\theta_{CB}}{\partial\theta_w} U_{\theta_w}\right)^2}.$$

Partial derivatives of the Cassie-Baxter equation with respect to the two variables comes out to

$$\frac{\partial\theta_{CB}}{\partial f_s} = \frac{f_s \sin\theta_w}{\sqrt{1-(f_s\cos\theta_w + f_s - 1)^2}},$$

$$\frac{\partial\theta_{CB}}{\partial\theta_w} = \frac{-(\cos\theta_w + 1)}{\sqrt{1-(f_s\cos\theta_w + f_s - 1)^2}}.$$

Substituting the partial derivatives into the uncertainty gives a final uncertainty of

$$U_{\theta_{CB}} = \frac{+}{-}\sqrt{\left(\frac{f_s \sin\theta_w}{\sqrt{1-(f_s\cos\theta_w + f_s - 1)^2}}U_{f_s}\right)^2 + \left(\frac{-(\cos\theta_w + 1)}{\sqrt{1-(f_s\cos\theta_w + f_s - 1)^2}}U_{\theta_w}\right)^2},$$

Where U_{θ_w} comes from the uncertainty in the wetting angle measurement, $U_{\theta_w} = U_\theta$.

APPENDIX B. ERROR/UNCERTAINTY FOR THE CAPILLARY NUMBER

Given that the capillary number is defined as

$$Ca = \frac{\mu v}{\gamma},$$

the uncertainty for the capillary number is defined as

$$U_{Ca} = \frac{+}{-}\sqrt{\left(\frac{\partial Ca}{\partial \mu}U_{\mu}\right)^2 + \left(\frac{\partial Ca}{\partial v}U_{v}\right)^2 + \left(\frac{\partial Ca}{\partial \gamma}U_{\gamma}\right)^2}.$$

Because the uncertainty in μ, and γ are beyond the scope of this research, the uncertainty simplifies to be a function of velocity, represented as

$$UCa = \frac{+}{-}\sqrt{(\frac{\mu}{\gamma} * Uv)^2}.$$

The uncertainty in the velocity is only a function of the drop height, *h*, and is given as

$$Uv = \sqrt{(\frac{\partial v}{\partial h} * Uh)^2}.$$

The partial derivative of the impact velocity with respect to the drop height is

$$\frac{\partial v}{\partial h} = \frac{\partial\sqrt{2gh}}{\partial h}$$

$$= \frac{\sqrt{2g}}{2\sqrt{h}}.$$

This gives a final uncertainty of the impact velocity defined as

$$Uv = \sqrt{(\frac{\sqrt{2 * g}}{2\sqrt{h}} * Uh)^2}.$$

This indicates that the uncertainty for the capillary number is a function of the drop height. Table A-1 lists the uncertainty in the capillary number for all the drop heights used in the study. It also lists the uncertainty in the capillary number as a function of the uncertainty in impact velocity as obtained from the error in the derivative of position calculation from Table 2-4 in the experimental methods section.

Table A-1. Uncertainty for the Capillary number as a function of the uncertainty in drop height (Uh) and the uncertainty/error in the derivative of position for select cases (Uv)

	Drop height		Velocity	Capillary #	Uncertainty			
	h(m)	h(in)	v(m/s)	Ca	Uh	UCa (Uh)	Uv	UCa (Uv)
Height measured on screen	0.003	0.125	0.250	3.8E-03	5.7E-04	3.4E-04		
	0.006	0.25	0.353	5.4E-03	5.7E-04	2.4E-04	1.0E-01	1.5E-03
	0.013	0.5	0.499	7.6E-03	5.7E-04	1.7E-04		
	0.025	1	0.706	1.1E-02	5.7E-04	1.2E-04	6.1E-02	9.2E-04
	0.051	2	0.998	1.5E-02	5.7E-04	8.5E-05		
Height measured with ruler	0.127	5	1.579	2.4E-02	3.2E-03	3.0E-04		
	0.254	10	2.232	3.4E-02	3.2E-03	2.1E-04	2.0E-02	3.0E-04
	0.508	20	3.157	4.8E-02	3.2E-03	1.5E-04		
	0.762	30	3.867	5.9E-02	3.2E-03	1.2E-04		
	1.016	40	4.465	6.8E-02	3.2E-03	1.1E-04		
	1.270	50	4.992	7.6E-02	3.2E-03	9.5E-05	1.1E-02	1.6E-04
	1.524	60	5.468	8.3E-02	3.2E-03	8.7E-05		
	1.778	70	5.906	9.0E-02	3.2E-03	8.0E-05		
	2.032	80	6.314	9.6E-02	3.2E-03	7.5E-05		
	2.286	90	6.697	1.0E-01	3.2E-03	7.1E-05		
	2.540	100	7.059	1.1E-01	3.2E-03	6.7E-05	5.0E-04	7.6E-06
	2.794	110	7.404	1.1E-01	3.2E-03	6.4E-05		
	3.048	120	7.733	1.2E-01	3.2E-03	6.1E-05		
	3.302	130	8.049	1.2E-01	3.2E-03	5.9E-05		
	5.588	220	10.471	1.6E-01	3.2E-03	4.5E-05	4.0E-04	6.1E-06

The resulting uncertainty in capillary number as calculated by both the uncertainty in the drop height and error in the derivative of position calculation are plotted against Capillary number in Figure A-1. It shows that both methods exponentially decrease with increasing Capillary number.

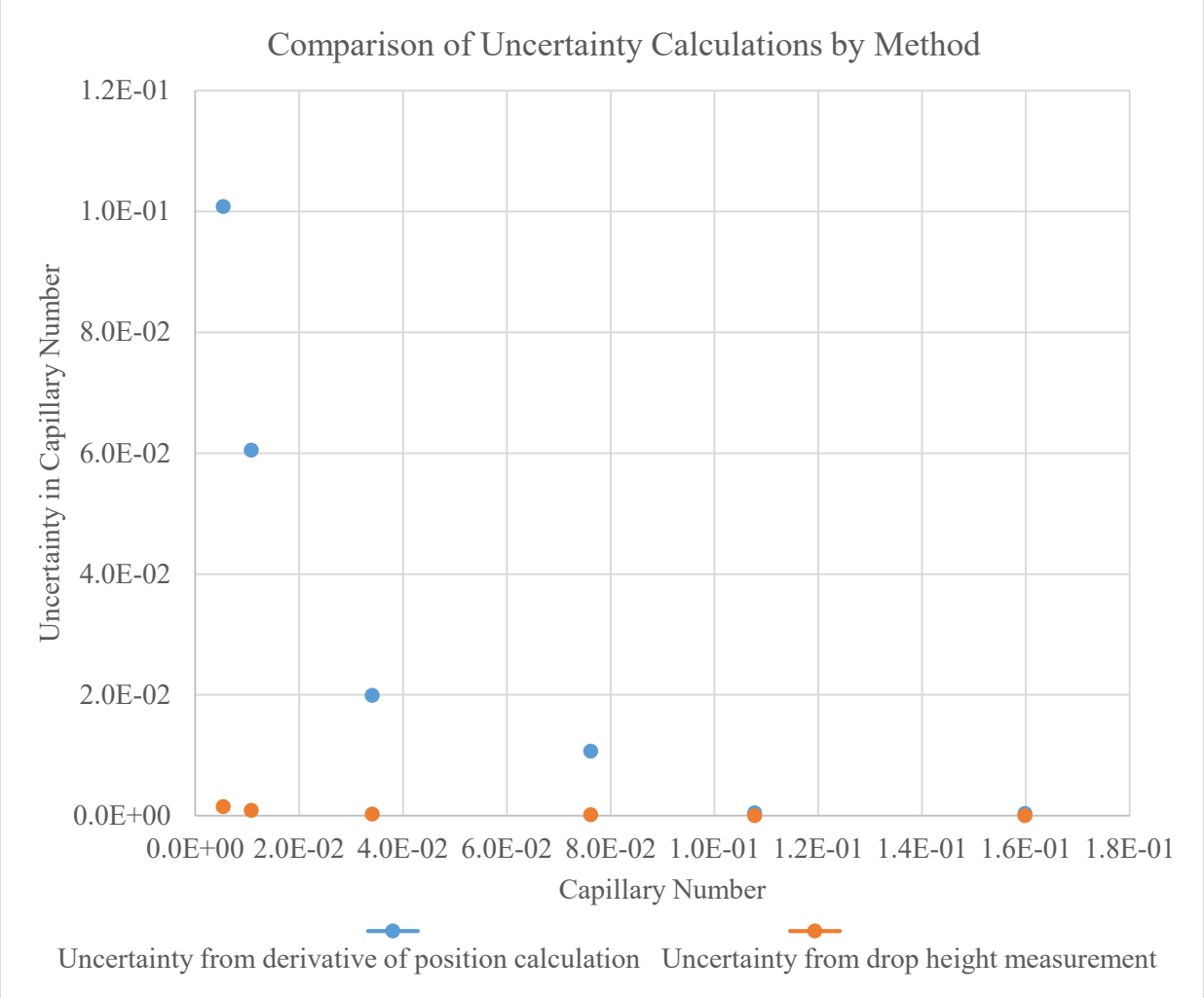

Figure A-1. Comparison of the effects of different uncertainties on the capillary number. Notice the high uncertainty associated with the derivative of position calculation at low Capillary numbers.